ABSTRACT

Title of Document: **DESIGN AND RELIABILITY ASSESSMENT OF HIGH POWER LED AND LED-BASED SOLID STATE LIGHTING**

Bong-Min Song, Doctor of Philosophy, 2012

Directed By: Professor Bongtae Han

Department of Mechanical Engineering

Lumen depreciation and color quality change of high power LED-based solid state light (SSL) are caused by the combination of various degradation mechanisms. The analytical/experimental models on the system as well as component-level are proposed to analyze the complex reliability issues of the LED-based solid SSL. On the system-level front, a systematic approach to define optimum design domains of LED-based SSL for a given light output requirement is developed first by taking cost, energy consumption and reliability into consideration. Three required data sets (lumen/LED, luminaire efficacy, and L70 lifetime) to define design domains are expressed as contour maps in terms of two most critical operating parameters: the forward current and the junction temperature (I_f and T_j). Then, the available domain

of design solutions is defined as a common area that satisfies all the requirements of a luminaire. Secondly, a physic of failure (PoF) based hierarchical model is proposed to estimate the lifetime of the LED-based SSL. The model is implemented successfully for an LED-based SSL cooled by a synthetic jet, where the lifetime of a prototypical luminaire is predicted from LED lifetime data using the degradation analyses of the synthetic jet and the power electronics. On the component-level front, a mathematical model and an experimental procedure are developed to analyze the degradation mechanisms of high power LEDs. In the approach, the change in the spectral power distribution (SPD) caused by the LED degradation is decomposed into the contributions of individual degradation mechanisms so that the effect of each degradation mechanism on the final LED degradation is quantified. It is accomplished by precise deconvolution of the SPD into the leaked blue light and the phosphor converted light. The model is implemented using the SPDs of a warm white LED with conformally-coated phosphor, obtained before and after 9,000 hours of operation. The analysis quantifies the effect of each degradation mechanism on the final values of lumen, CCT and CRI.

DESIGN AND RELIABILITY ASSESSMENT OF HIGH POWER LED AND LED-BASED SOLID STATE LIGHTING

By

Bong-Min Song

Dissertation submitted to the Faculty of the Graduate School of the
University of Maryland, College Park, in partial fulfillment
of the requirements for the degree of
Doctor of Philosophy
2012

Advisory Committee:
Professor Bongtae Han, Chair/Advisor
Professor Avram Bar-Cohen
Professor Mario Dagenais
Professor Joon-Hyun Lee
Professor Youngrae Cho
Professor Jong Soo Ko

Acknowledgement

When I made my mind to go to U.S., one of my friends told me that all I have to do is just holding my pencil and then he will do everything for me. I laughed at him at the moment. That turned out to be true. All I have done was just holding my pencil. Sometimes, the pencil was so heavy to be held. At other times, I wanted to throw it away. However, he made me achieve this, finally. I achieved that I did not dream of. I do not understand how I can be here. I am on the way that I could not imagine. My God is so amazing beyond description. If someone reads this thesis, I want to tell you that you must see him, now. Please go to the church. You will experience more amazing love than this thesis in your life. I am really serious.

While I was pursuing my degree, I have been supported and accompanied by many people. I could not finish this epic journey without their help. First, I gratefully acknowledge the guidance from my precious adviser Professor Han. God set him as my advisor. I could have not succeeded without his continual advice and support. I will never forget the tremendous amount of time we had spent. I have learned a lot about myself during the time. It was a great chance to look back my past life and to set the goal in my life. I also have to thank my Korean advisor Joon-Hyun Lee. If he didn't open the joint Ph.D. program between UMD and PNU, I would not be able to start the degree. Next, I would like to thank the members of my dissertation committee, Professors Avram Bar-Cohen, Youngrae Cho, Jong Soo Ko, and Mario Dagenais for their support and suggestions during my graduate career, as well as in the completion of this dissertation.

I should remember the support from my fiancé Dahyun Lee. She is a wonderful present from God, who always prays for me. I do not think that I would be successful without her prayer. I have to thank my second family in U.S.: Rev. Youn, Elder Kim, Deacon Sin, Noh and moon, Jungbin, Jongyoun, Changwon, Hyelim, Younjung, Inseok, Suzie, Arin, Kangtaek, Sunyoung, and Hakseong. I cannot mention all of them but I feel grateful to them in the church.

I also appreciate the support from all LOMSS members: Dr. Jang, Yejin, Belong, Yong Sun, Dae-Suk, Stephen, Dr. Oh, Kenny, Laura, Yong Wang, Ari, and Hongbo. I will miss all of you. I would like to acknowledge the help from many Korean students. Special thanks are given to Sungwon, Wonseok, and Sungmin for their assistance, suggestions, and friendship.

I owe a big hug to my family, Sung-Il (dad) and Pilja (mom), Bong-Ae (brother) and Minsu (sister), for their encouragement and love, even from a distance. I will always love you. I dedicate this thesis to them.

Table of Contents

List of Figures

Chapter 1: Introduction

1.1. Motivations and Objectives

LED based luminaire have been accepted as a general light source, which will eventually substitute the incandescent and fluorescent lights as the performance of pc-LEDs is improved continuously. It has been claimed that the luminous efficacy of 254 lm/W can be achieved under normal operating conditions [1]. Various types of LED based luminaire have been released in the market attracting considerable interest due to advantages such as compact size, high color quality, high luminaire efficacy, and long lifetime compared to conventional light sources. This revolutionary transition is imminent as demands for green energy (no hazardous materials such as lead and mercury) and reduction of energy consumption continuously increase.

Although LEDs are attractive for lighting applications due to the aforementioned advantages, the extreme sensitivity of light output and useful lifetime to the LED junction temperature remains a unique technical challenge. This thesis concerns three technical issues to help overcome the challenge. The motivation and objective of each issue are described in the following section.

1.1.1. Design Optimization of LED Based Luminaire

Design considerations for LED-based luminaires are unique in that many design solutions are possible for the same required light output unlike the conventional light sources (e.g., compact florescent light, incandescent light, etc.).

This is due to the well-known fact that the lumen output that each LED produces is a function of the driving current, I_f, as well as the junction temperature, T_j.

The luminous flux of LEDs increases as the driving current increases, but the corresponding luminous efficacy decreases at a higher driving current because the luminous flux is not linearly proportional to a driving current. More importantly, when a higher driving current is used, heat flux becomes proportionally larger, resulting in a higher junction temperature. This increased junction temperature not only decreases the luminous flux but also significantly affects the rate of lumen maintenance (i.e., life time). A lower driving current can be utilized if more LEDs are used in the light engine of a luminaire. Yet this is often not the most desired solution due to the high cost of LEDs.

For a required light output, the optimum design of a LED-based luminaire can be achieved by considering (1) cost, (2) energy consumption, and (3) reliability. In an LED-based luminaire design, all design parameters are interdependent and the corresponding requirements are dictated by operating conditions (I_f and T_j).

The objective is, thus, to propose a methodology to define the optimum design domains of LED-based luminaires considering cost, energy consumption and reliability.

1.1.2. Physic of Failure Based Reliability Assessment of LED-Based Luminaire

The high lumen requirements for LED-based luminaire necessitate a cost effective thermal management solution because many of the components within LED packages and lighting systems are temperature-limited. LED cooling solutions are also required to match to the efficiency, compactness, and reliability of LED chip components. Thermal management solutions (conduction as well as convection) of LEDs must be provided to maintain the LED junction temperature below a critical value. Otherwise, the LED system would not meet the required life expectancy.

Passive cooling solutions have been implemented for several LED-based luminaires. Due to the limited cooling capacity offered by passive cooling, the maximum total light output is limited. In order to be accepted more widely for general illumination, the LED-based luminaires requires the development of active cooling solutions, especially for applications with the high lumen requirement in a compact volume.

The reliability of the luminaire with an active cooling device is dependent not only on the junction temperature itself but also on its gradual increase caused by the time-dependent performance degradation of active cooling devices.

The objective is, thus, to develop a hierarchical physics-of-failure (PoF) model that can be used to assess the reliability of an actively cooled luminaire.

1.1.3. Quantification of LED degradation mechanism

Reliability of pc-LEDs has been studied by numerous researchers since LED-based solid state lighting (SSL) was realized for residential and commercial applications. In Refs. [2-8], reliability of LEDs was assessed by simply monitoring light output. An empirical model was developed assuming the exponential decay of light output [3] and used for the lifetime prediction [9, 10]. The reliability was also assessed using both optical and electrical characteristics [8, 11-20]. An increase in the forward voltage was observed in degraded LEDs [12, 17, 20]. The degradation of phosphor was reported in Refs. [7, 21-24]. The degradation of phosphor was indicated by reduction in the phosphor converted light power [21-23]. The effect of packaging material degradation was reported in Refs. [24-32]. The dominant degradation phenomenon was silicone or epoxy lens yellowing.

The degradation of phosphor converted LEDs (pc-LEDs) decreases lumen maintenance. The lumen depreciation can be caused by a combination of various degradation mechanisms; i.e., degradation mechanisms can contribute at different rates to cause the same lumen reduction. It is difficult to quantify the contribution of each degradation mechanism from a degraded pc-LED. The reliability of pc-LEDs can be improved provided the contribution of each degradation mechanism is quantified.

The objective is, thus, (1) to identify the spectral power distribution (SPD) change associated with the corresponding degradation mechanism and (2) to propose and implement a mathematical and experimental procedure to quantify the effect of each degradation mechanism on the final LED degradation. The goal is achieved by

analyzing the SPDs of new and aged pc-LEDs in such a way that the SPD change after operation is decomposed into the contributions of individual degradation mechanisms.

1.2. Organization of Dissertation

This first chapter describes the motivations and three main objectives of the dissertation. The three objectives are addressed in the subsequent chapters.

Chapter 2 presents a design methodology of LED-based luminaires. Design parameters of LED-based solid state lighting products are interdependent and the corresponding requirements are dictated by operating conditions. A scheme to define optimum design domains of LED-based luminaires for a given light output requirement by taking cost, energy consumption and reliability into consideration is proposed. First three required data sets to define design domains are expressed as contour maps in terms of the forward current and the junction temperature (I_f and T_j): (1) face lumen and cost requirement as lumen/LED; (2) power consumption and energy requirement as luminaire efficacy (*LE*); and (3) reliability requirement as L70 lifetime. Then, the available domain of design solutions is defined as a common area that satisfies all the requirements of a luminaire. The proposed scheme is implemented for a wall wash light and the optimum design solutions are presented. This chapter has been accepted for publication in *Microelectronics Reliability* and will be published as a research paper soon.

Chapter 3 is devoted to PoF based reliability assessment of LED-based luminaire. An Edison base – 6 inch, compatible can, downlight – LED replacement bulb, cooled by an active *synthetic jet*, is used as the test vehicle. Based on the identified degradation mechanisms and the experimentally obtained degradation rate of the cooling device, the reduction in the heat sink enhancement factor, and thus the increase in the LED junction temperature, is determined as a function of time. The degradation mechanisms of the dual-function power electronics – providing constant current to the LEDs and to the drivers of a series of synthetic jets – are also analyzed and serve as the basis for a hybrid model which combines these two effects on the luminaire lifetime. The lifetime of a prototypical luminaire is predicted from LED lifetime data using the degradation analyses of the synthetic jet and power electronics. This chapter has been published as a research paper in *Microelectronics Reliability*.

Chapter 4 provides a novel procedure to deconvolute the spectral power distribution (SPD) of phosphor-converted LEDs (pc-LEDs). The procedure involves a two-step process using multiple Gaussian functions. The first step is a preliminary process to deconvolute an SPD using a pair of Gaussian functions. Using the results from the first step, the second step determines (1) the number of Gaussian functions to be used in the analysis and (2) the initial values and regression domains of the coefficients of each Gaussian function for subsequent multiple-regression operations. Successful deconvolution is confirmed by comparing the values of lumen, CCT and CRI with the experimental data of cool and warm pc-LEDs. The approach is used to analyze the degradation analysis of pc-LED in Chapter 5. This chapter has been submitted to *Applied Optics* and is currently under a review process.

Chapter 5 focuses on a mathematical and experimental procedure to quantify the effect of each degradation mechanism on a pc-LED degradation. A mathematical model based on the spectral power distribution (SPD) is proposed after defining each degradation parameter. The model decomposes effectively the SPD change caused by the degradation into the contributions of individual degradation mechanisms. The model is implemented using the SPDs of a pc-LED with a conformally coated phosphor, obtained before and after 9,000 hours of operation. The analysis quantifies the effect of each degradation mechanism on the final values of lumen, CCT and CRI. This chapter has been submitted to *IEEE Transactions on Device and Materials Reliability* and is currently under a review process.

Chapter 6 contains a summary of the contributions made by this study and a discussion for future studies that can be extended from the present study.

Chapter 2: Design Domain of LED-based Luminaires: Optimization of Cost, Energy Consumption and Reliability[1]

Abstract

Design parameters of LED-based solid state lighting products are interdependent and the corresponding requirements are dictated by operating conditions. We propose a scheme to define optimum design domains of LED-based luminaires for a given light output requirement by taking cost, energy consumption and reliability into consideration. First three required data sets to define design domains are expressed as contour maps in terms of the forward current and the junction temperature (I_f and T_j): (1) face lumen and cost requirement as lumen/LED; (2) power consumption and energy requirement as luminaire efficacy (*LE*); and (3) reliability requirement as L70 lifetime. Then, the available domain of design solutions is defined as a common area that satisfies all the requirements of a luminaire. The proposed scheme is implemented for a wall wash light and the optimum design solutions are presented.

[1] This chapter will be published in the *Microelectronics Reliability* under the title of "Optimum design domain of LED-based solid state lighting considering cost, energy consumption and reliability" by B. Song, B Han and J. Lee

2.1. Introduction

Recently LED-based luminaires have emerged rapidly for commercial and residential applications. For a required light output, the optimum design of a LED-based luminaire can be achieved by considering cost, energy consumption and reliability.

Design considerations for LED-based luminaires are unique in that many design solutions are possible for the same required light output unlike the conventional light sources (e.g., compact florescent light, incandescent light, etc.). This is due to the well-known fact that the lumen output that each LED produces is a function of the driving current, I_f, as well as the junction temperature, T_j.

Figure 2.1 illustrates the details. The luminous flux of LEDs increases as the driving current increases, but the corresponding luminous efficacy decreases at a higher driving current because the luminous flux is not linearly proportional to a driving current. More importantly, when a higher driving current is used, heat flux becomes proportionally larger, resulting in a higher junction temperature. This increased junction temperature not only decreases the luminous flux but also significantly affects the rate of lumen maintenance (i.e., life time). A lower driving current can be utilized if more LEDs are used in the light engine of a luminaire. Yet this is often not the most desired solution due to the high cost of LEDs.

In an LED-based luminaire design, all design parameters are interdependent and the corresponding requirements are dictated by operating conditions (I_f and T_j). This paper suggests a methodology to define the optimum design domains of LED-based luminaires considering cost, energy consumption and reliability. The required

data sets to define design domains are described in Section 2.2. An application using the requirements of wall wash light is provided in Section 2.3.

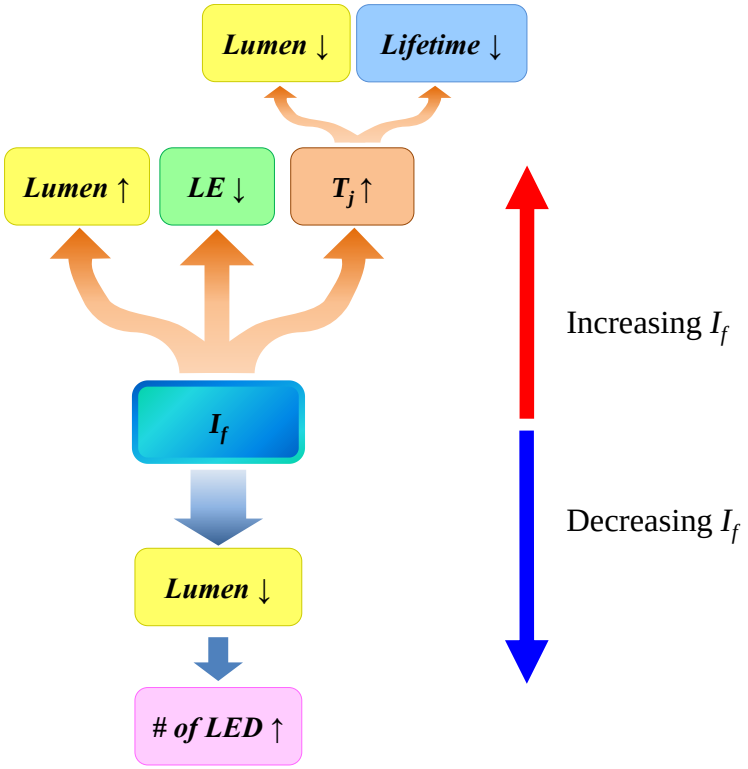

Figure 2.1 Effect of I_f on performance of LED-based luminaire

2.2. Design Considerations and Required Data Sets

Optimum design of LED-based luminaires can be achieved by considering cost, energy consumption and reliability. These design parameters can be expressed as lumen/LED, luminaire efficacy, and L70 lifetime, respectively. Since they are a function of operating conditions, the parameters can be quantified in the domain of junction temperature (T_j) and forward current (I_f).

This section describes the three interdependent design parameters and defines the data sets required to obtain them. Test data obtained from a commercial phosphor converted LED are used to illustrate the concept.

2.2.1. Cost (lumen/LED)

The Department of Energy (DoE) of U.S. published the requirements for solid state lighting luminaires [33]. To deliver a required light output, two different approaches can be considered depending upon the nature of applications. For medical and military applications where stringent reliability requirements must be met, the required light output should be delivered at a junction temperature that is sufficiently low to satisfy the high reliability standards. For a given passively or actively-cooled luminaire, a low junction temperature can be achieved only by a low forward current level, which forces to employ as many LEDs as needed. For commercial and residential applications, however, LED-based luminaires should use only a minimum number of LEDs to be cost-effective and thus to be competitive with the conventional light sources. Therefore, the light output of a single LED at a specified condition is a very important parameter. Since the light output is a function of forward current and junction temperature, the light output has to be measured at various forward current and junction temperature conditions.

Figure 2.2 shows an experimental setup used to acquire light output at different currents and junction temperatures. An LED (CREE XR-E) is mounted on a thermoelectric cooler (TEC) in an integrating sphere. The LED has a conformally coated phosphor layer on the chip and encapsulated with transparent silicone. The top

part dome is glass. The package is surrounded with the aluminum reflector. The TEC controls the *solder point temperature*[2] of LED (T_s) and the integrating sphere equipped with a spectroradiometer (SMS–500: Labsphere) system measures the spectral power distribution (SPD) of the LED at the various operating conditions. The sampling interval of the spectroradiometer is 1 nm. The measurement range of wavelength is 360-1000 nm. The TEC is controlled by a thermal controller (LB 320: Silicone Thermal. Co. Ltd.) using an input provided by a T-type thermocouple directly mounted on the solder point surface. The setup can adjust the solder point temperature from -40 to 125 ℃ with a resolution of 0.1 ℃.

The junction temperature can be estimated by the well-known forward voltage method [34]. The method is valid only when a pulsed current with a very short duration is used so that the junction temperature does not change during forward voltage measurement. For the SPD measurement, however, the spectroradiometer requires an integration time [35], which is usually much longer than the short pulse duration for the forward voltage method: a typical integration time for a full white light spectrum is 100 to 1000 ms. As a result, an additional increase of junction temperature is unavoidable during the SPD measurement.

[2] The “solder point” is the point at which the solder meets with a printed circuit board and LED leads. Some LED manufactures refer to "case temperature" but referring to the solder point temperature is more precise.

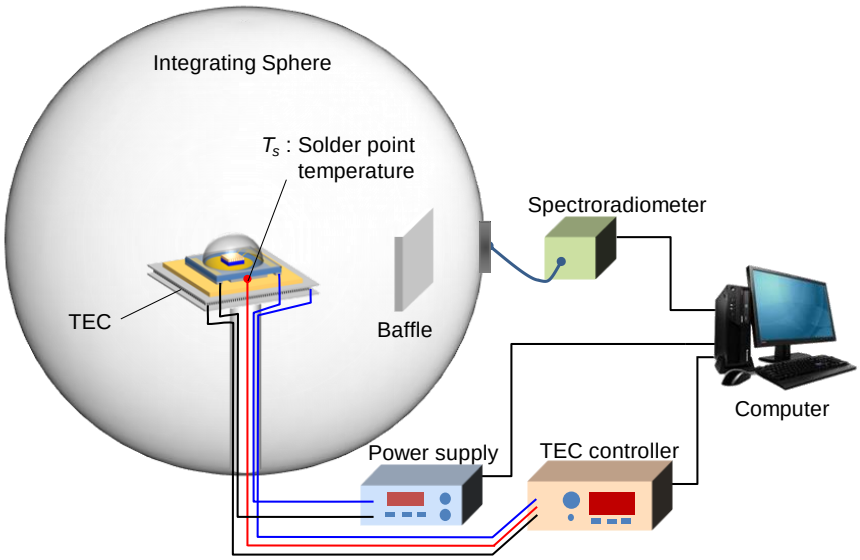

Figure 2.2 Experimental setup for luminous flux measurement (4π configuration)

In order to avoid this undesired error in junction temperature measurement, an LED is subjected to a steady-state condition inside an integrating sphere for accurate junction temperature measurement. With the 4π configuration in Fig. 2.2, a current is applied to the LED continuously until the solder point temperature reaches a preset value which is maintained by controlling the TEC. Once the solder point temperature is stabilized, the SPD and the forward voltage of the LED are measured simultaneously.

The SPDs have been measured at various solder point temperatures and forward currents: T_s from 65 to 125 ℃ with a constant interval of 15 ℃ and I_f from 300 to 1000mA with a constant interval of 100mA. The total number of measurements is 40. Typical SPDs obtained at T_s = 65 and 125 ℃ at I_f = 300 and 1000mA are shown in Fig. 2.3. The radiant flux and the corresponding luminous flux obtained from all 40 measurements are shown in Fig. 2.4a and b, respectively. As

expected, the luminous flux increases as the solder point temperature decreases under a constant current.

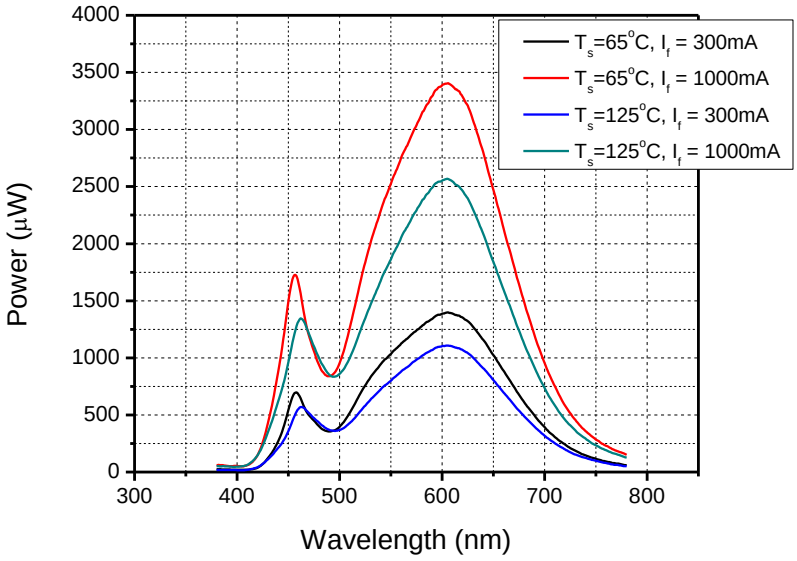

Figure 2.3 SPDs at various conditions; T_s = 65 and 125 °C at I_f = 300 and 1000 mA

The measurement data obtained for solder point temperatures can be converted to the junction temperature domain through the relationship between junction temperature and solder point temperature, which can expressed as [3, 7, 36]:

$$T_j = T_s + P(1-\eta_P)R_{js} = T_s + I_f V_f (1-\eta_P) R_{js} \tag{2.1}$$

where T_s is the solder point temperature, P is the total electrical power consumption in W $\left(= I_f \cdot V_f\right)$, η_p is the LED power efficiency (the radiant flux divided by the total electrical power input), I_f is the forward current, V_f is the forward voltage and R_{js} is the thermal resistance between the chip and the solder point (8℃/W for the LED tested in this study [37]). It is important to note that power efficiency in Eq. (2.1) was often ignored in the thermal analysis of low power LEDs due to low efficiency [38,

39]. For high power LEDs with typical power efficiency of 15~30%, the effect of the power efficiency must be considered in a thermal analysis.

The forward voltage is measured first as a function of solder point temperatures (Fig. 2.5a), from which the total electrical power consumption is determined. The results are shown in Fig. 2.5b. The power efficiency then can be determined simply by dividing the total power consumption by the radiant flux amount shown in Fig. 2.4a, and the results are shown in Fig. 2.6. The power efficiency varies significantly with the forward current.

The solder point temperatures in Fig. 2.6 can be converted to the corresponding junction temperatures using Eq. (2.1). The converted power efficiency as a function of junction temperature is shown in Fig. 2.7. It is worth noting that the power efficiency decreases almost linearly as the junction temperature increases and the rate of the power efficiency reduction remains the same regardless of the current.

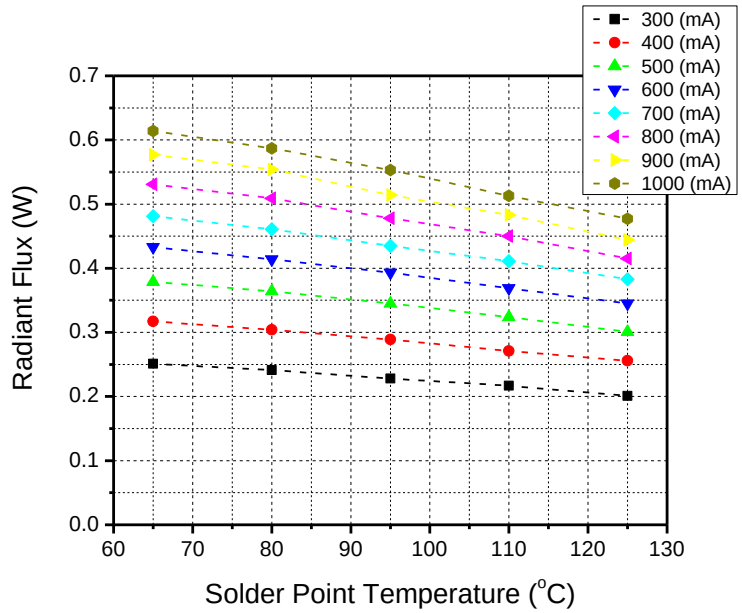

(a)

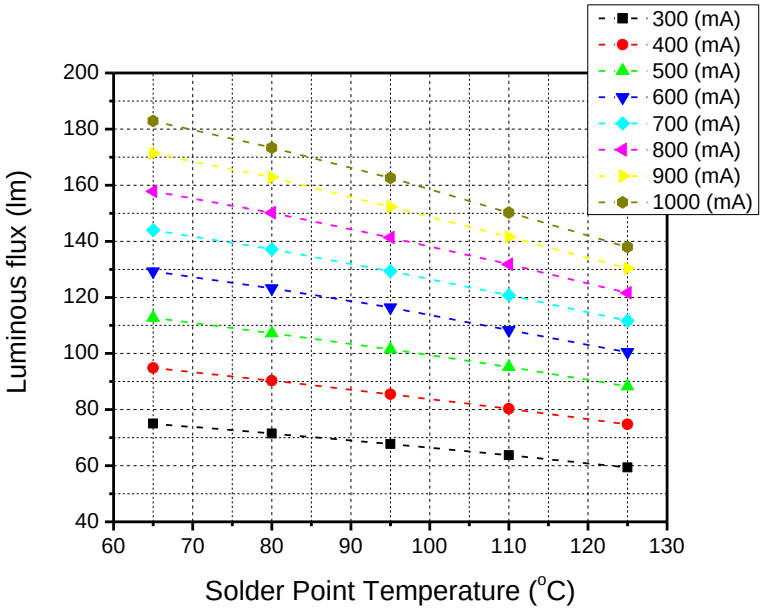

(b)

Figure 2.4 (a) Radiant flux and (b) luminous flux at different forward currents as a function of solder point temperatures

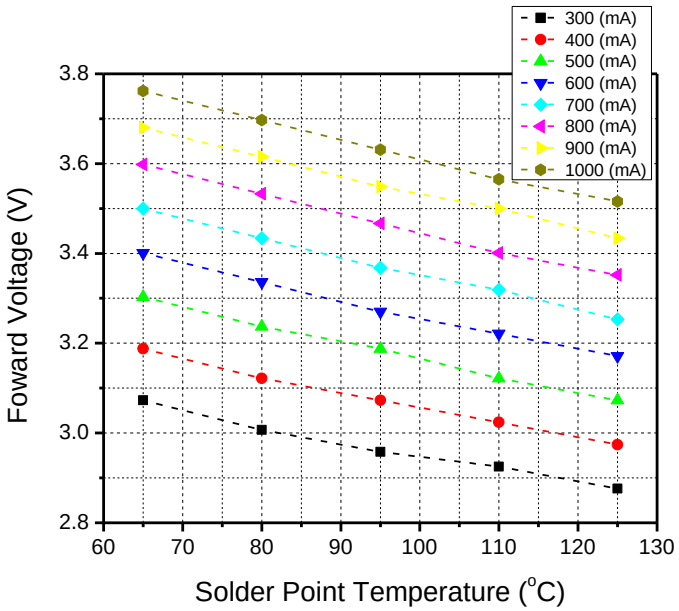

(a)

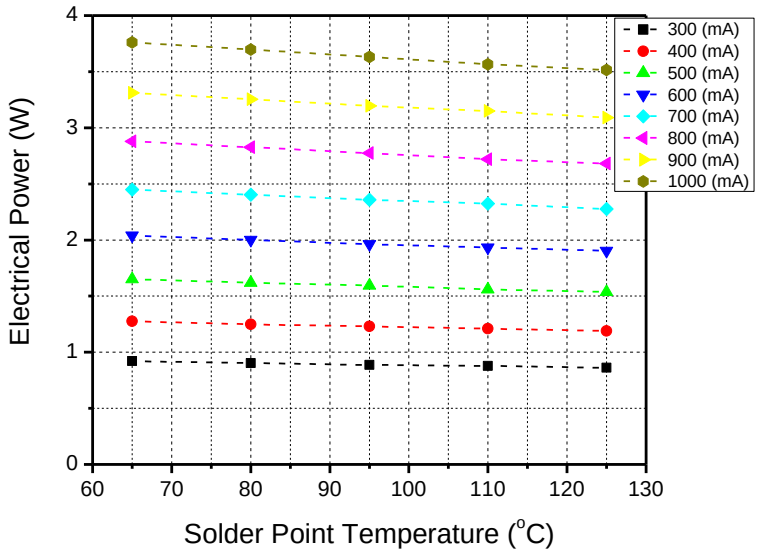

(b)

Figure 2.5 (a) Forward voltage and (b) electrical power consumption at different forward currents as a function of solder point temperatures

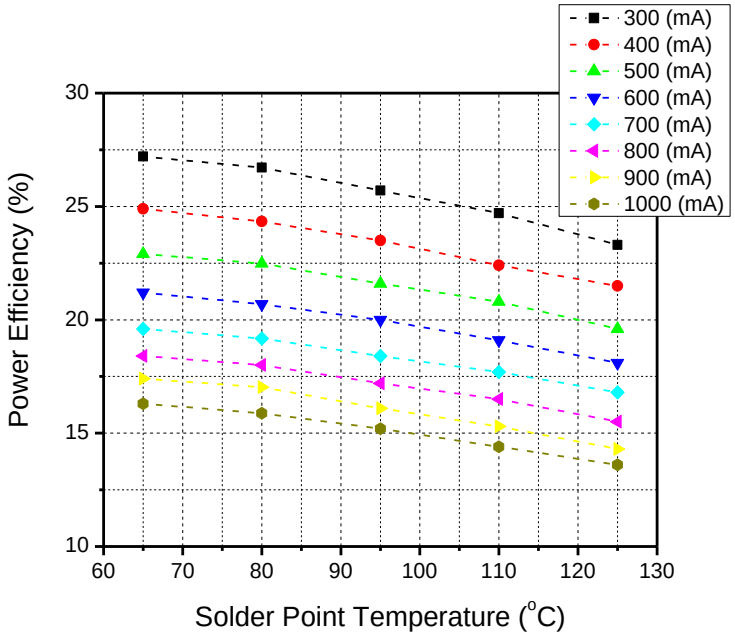

Figure 2.6 Power efficiency of LED at different currents as a function of solder point temperatures

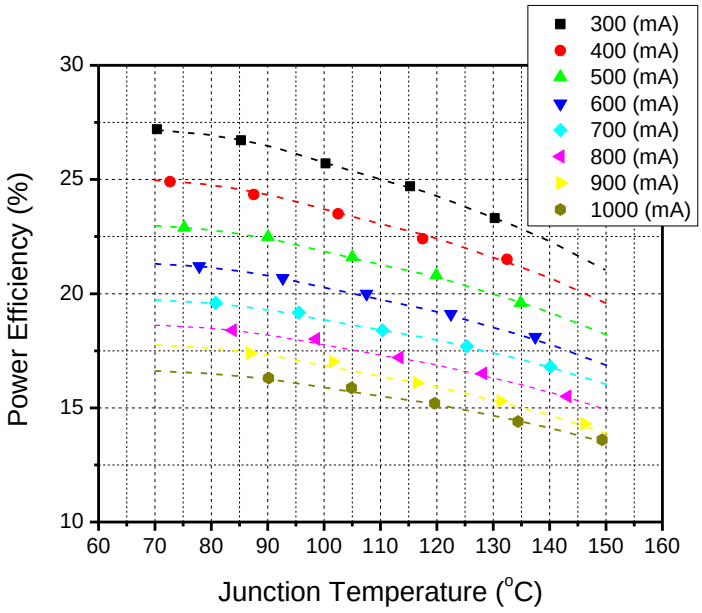

Figure 2.7 Power efficiency of LED at different currents as a function of junction temperatures

The luminous flux data of Fig. 2.4b can be also presented in the junction temperature domain using Eq. (2.1) and the power efficiency data. The converted luminous flux data is shown in Fig. 2.8. From the data in Fig. 2.8, a contour plot of the luminous flux of a single LED in a domain of the forward current and the junction temperature can be determined (Fig. 2.9). The contour plot shows the distinctive characteristic of LED luminous flux, which depends on the junction temperature as well as the forward current.

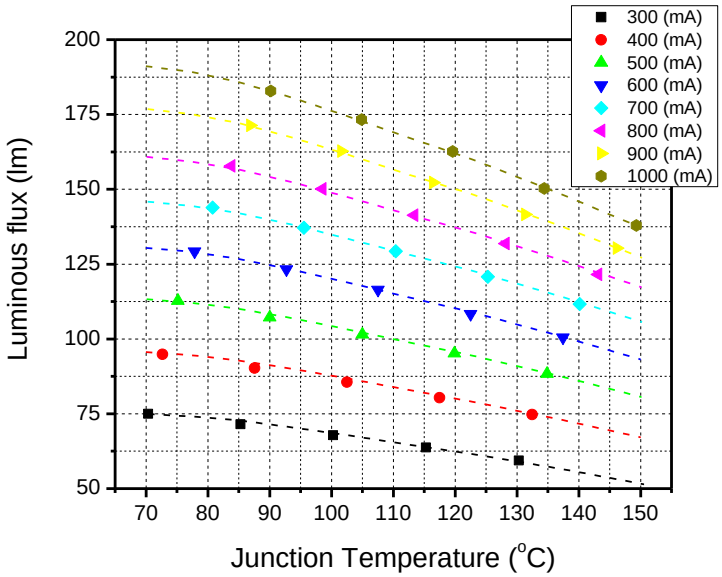

Figure 2.8 Luminous flux at different currents as a function of junction temperatures

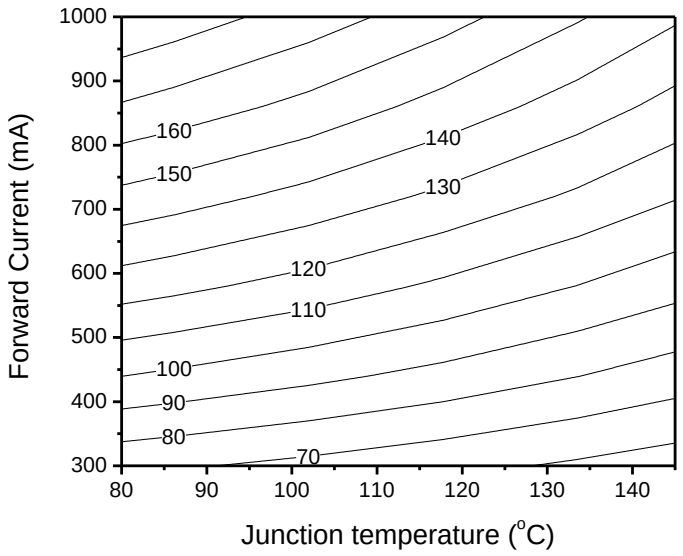

Figure 2.9 *Lumen/LED* as a function of I_f and T_j

2.2.2. Energy Consumption (Luminaire Efficacy)

One of the key attributes of LED lighting is low power consumption. In other words, LED-based luminaire can deliver the same amount of luminous flux with lower power consumption compared to the conventional light sources. This property is expressed as *luminaire efficacy* [40], which is defined as the total lumens produced by a luminaire divided by the total wattage drawn by the power supply/driver, expressed in lumens per watt (lm/W); i.e.,

$$\left|LE\right|_{luminaire} = \left|LE\right|_{LED} \times F_{fixture} \tag{2.2}$$

where $\left|LE\right|_{luminaire}$ is the luminaire efficacy (lm/W), $\left|LE\right|_{LED}$ is the luminous efficacy of each LED (lm/W) and $F_{fixture}$ is the luminaire fixture efficiency (%). It is important to note that the luminaire efficacy remains the same regardless of the

number of LEDs used in a luminaire as long as the forward current and the junction temperature remain the same.

Luminaire efficacy is a function of luminous flux and power consumption. The luminous efficacy of an LED can be obtained by dividing the lumen/LED (Fig. 2.9) by power consumption (Fig. 2.5b). The luminaire efficacy contour is shown in Fig. 2.10, where the fixture efficiency of 90% is assumed based on the values provided in Ref. [41]. The light output does not increase linearly with the increasing current due to the efficiency drooping [42-44] at a fixed junction temperature and it is well known that LED light output decreases with an increasing junction temperature at a fixed current. As expected, the luminaire efficacy increases with the decreasing forward current and junction temperature.

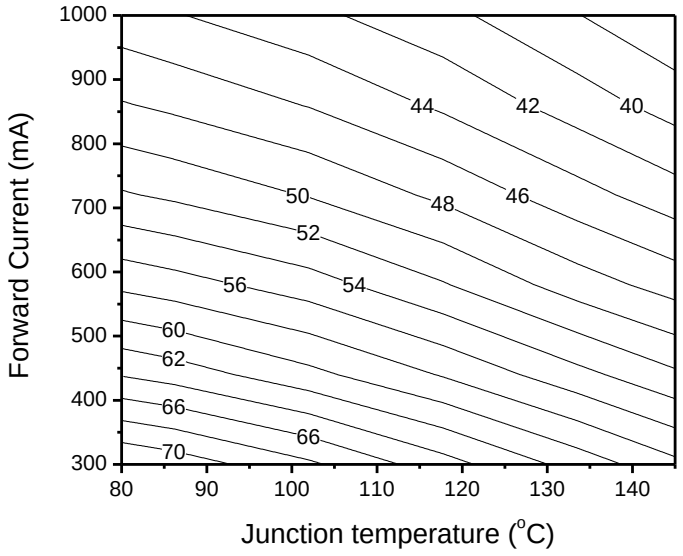

Figure 2.10 *Luminaire Efficacy* as a function of I_f and T_j

2.2.3. Reliability (L70 Lifetime)

All electrically powered light sources experience light reduction as they continuously illuminate light under normal operating conditions. This is known as lumen depreciation [45]. The lifetime of an LED is characterized by its *L70 lifetime*, which is the time to 70% of an initial light output. In order to estimate the LED lifetime, major LED manufacturers have adopted IESNA LM-80 [46]. The document prescribes standard test methods to measure lumen maintenance of LEDs under controlled conditions (constant junction and ambient temperatures with a constant DC mode). Since LEDs have very long expected lifetime (> 30,000 hours), a complete lifetime test is not practical. The LM-80 recommends a minimum of 6,000 hours testing with 1,000 hours measurement interval. Then, the lifetime of LED has to be extrapolated from the test data. Although the empirical equation of LED lumen depreciation is known to take an exponential form [3, 7], LED manufacturers use their own extrapolation schemes [47, 48].

The LED lifetime is dictated by operating conditions: longer lifetimes are expected at the lower junction temperature and the lower forward current. Ambient temperature is also an important factor for the LED lifetime. When LEDs are exposed to high temperature ambient conditions, the package of LEDs is degraded [23, 49]. The well-known package degradation mechanisms are reflective coating degradation and optical lens yellowing. They not only decrease the total light output but also change CCT [7, 17, 49].

Figure 2.11 shows the *L70 lifetime* at different junction temperatures and forward currents at two different ambient temperatures of 65℃ and 75 ℃ [48]. The

data in Fig. 2.11 is converted to contour plots in Fig. 2.12. The contour plot clearly shows that the lifetime of LED is more sensitive to the junction temperature than the forward current under the same ambient temperature.

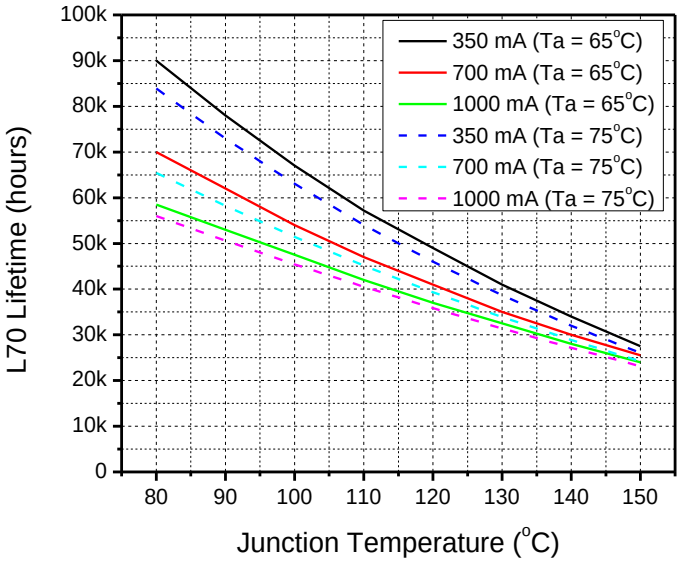

Figure 2.11 *L70 lifetime vs.* T_j at different I_f*s* at T_a = 65 ℃ and 75 ℃ [48]

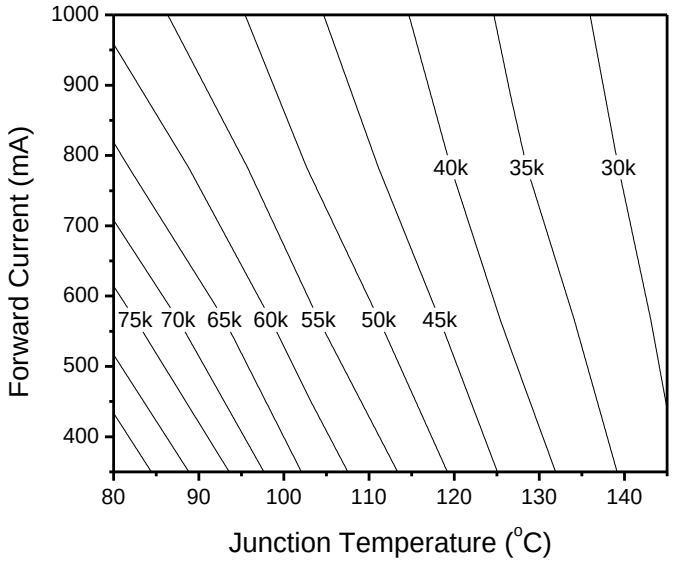

(a)

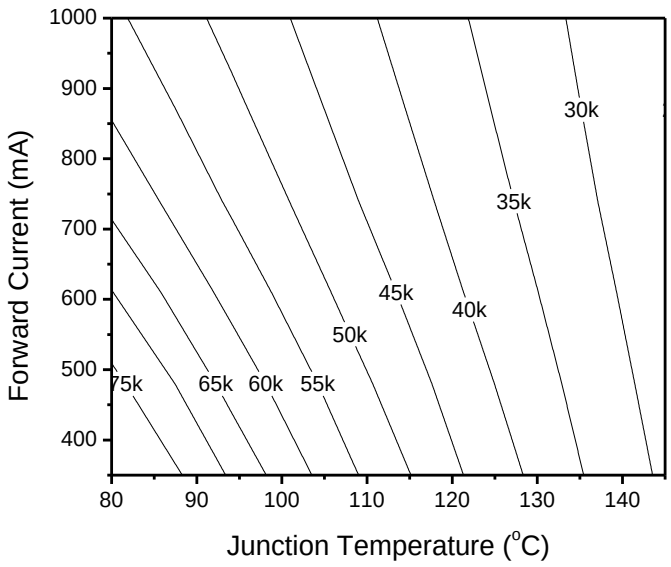

(b)

Figure 2.12 *L70 lifetime* as a function of I_f and T_j at (a) T_a = 65 ℃ and (b)T_a = 75 ℃

2.2.4. Extra Consideration: Minimum Junction Temperature

In the previous sections the data has been shown over the whole junction temperature range. In practice, the junction temperature is always higher than the solder point temperature (and the ambient temperature), and there should be a low bound of the junction temperature, below which a design solution is not valid.

The thermal network model can be utilized to determine the low bound. Figure 2.13 illustrates a simplified thermal resistance network model of the LED considering only the downward path through the heat slug to the mold, substrate and solder point [36]. The upward path through the encapsulant to the lens surface can be ignored since the upward heat transfer is less than 1% of the total heat transfer.

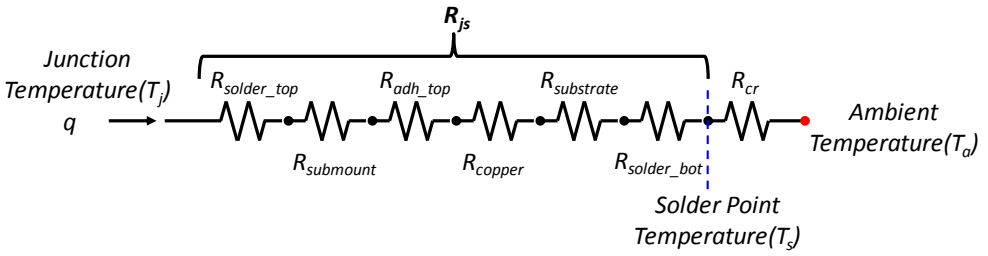

Figure 2.13 Simplified resistance network model of LED package

The network model can be further simplified by breaking the full network into two parts: internal (conductive) and external (convective and radiative) resistances [36]. It is expressed as

$$q = \frac{T_s - T_a}{R_{cr}} = \frac{T_j - T_s}{R_{js}} \tag{2.3}$$

where q is the heat generated by the LED (W) at a given current; R_{js} is the conduction resistance in (℃ /W); R_{cr} is the effective external resistance (℃ /W); T_j is the junction temperature (℃); T_s is the solder point temperature of the downward path (℃); and T_a is the ambient temperature. The effective internal thermal resistance for conduction, R_{js}, and the effective external thermal resistance (including convection and radiation), R_{cr}, can be defined as

$$R_{js} = \frac{t}{kA_{cd}} \quad \text{and} \quad R_{cr} = \frac{1}{A_{cr}\left(h + h_r\right)} \tag{2.4}$$

where t is the thickness (m), k is the heat conductivity (W/mK), h is the convection coefficient (W/m^2), h_r is the effective convection coefficient for radation (W/m^2), A_{cd} and A_{cr} are the effective areas of the conduction and the convection /radiation (m^2), respectively.

Since T_s is always higher than T_a , the lowest possible junction temperature T_j^{min} can be defined as:

$$T_j^{min} = R_{js} \cdot q^{min} + T_s^{min} \tag{2.5}$$

where q^{min} is the minimum heat generation at a given forward current, which can be defined as:

$$q^{min} = P^{min}\left(1-\eta^{max}\right) \tag{2.6}$$

The minimum power and the maximum power efficiency at a given forward current can be obtained from Fig. 2.5b and Fig. 2.6, respectively.

The power consumption and the power efficiency of LED are dictated by the LED junction temperature. The minimum power consumption for a given forward current can be achieved at the highest junction temperature while the maximum power efficiency for a given forward current can be achieved at the lowest junction temperature (Fig. 2.7). Figure 2.14 shows the minimum junction temperatures as a function of ambient temperatures obtained from Eqs. (2.5) and (2.6). The junction temperatures shown in Fig. 2.14 are the practical lower bound under the ambient temperatures.

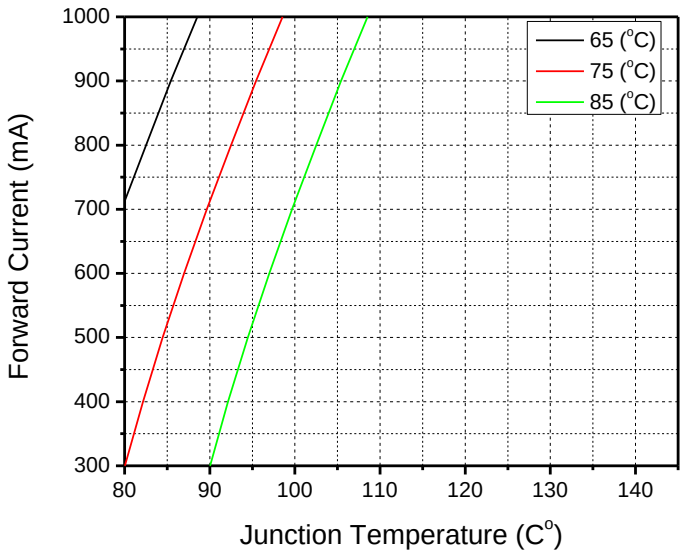

Figure 2.14 Minimum junction temperatures for different ambient temperature conditions.

2.3. Implementation for Wall Wash Light

In order to illustrate the proposed approach, wall wash light was selected as an example for implementation. Wall wash lights (Fig. 2.15) are used to illuminate walls in buildings, bridges and towers for decoration and lighting purpose. The requirements of a wall wash light are specified as [33]:

- Luminous flux: 575 lm
- Luminaire Efficacy: 40 lm/W
- L70: 35000 h

Figure 2.15 Example of wall wash light [50]

Assuming the same LED (CREE XR-E) is used for the wall wash light, the *lumen/LED* (Fig. 2.9) can be used first for cost consideration. The lumen output that each LED has to deliver is

$$\text{Lumen output} = \frac{575}{N} \times \frac{1}{F_{fixture}} \tag{2.7}$$

where N is the number of LEDs used in the luminaire and $F_{fixture}$ is the luminaire fixture efficiency. Considering again the typical fixture efficiency of 90%, the above relationship can be used to convert Fig. 2.9 to Fig. 2.16 where each contour line shows available operating conditions for the corresponding number of LEDs used in the wall wash light. The next step is to define domains for the required *luminaire efficacy* of 40 lm/W using Fig. 2.10. The domain that satisfies the requirement of luminaire efficacy is shown in Fig. 2.17. Since LED has very high luminaire efficacy, most of the domain satisfies the requirement.

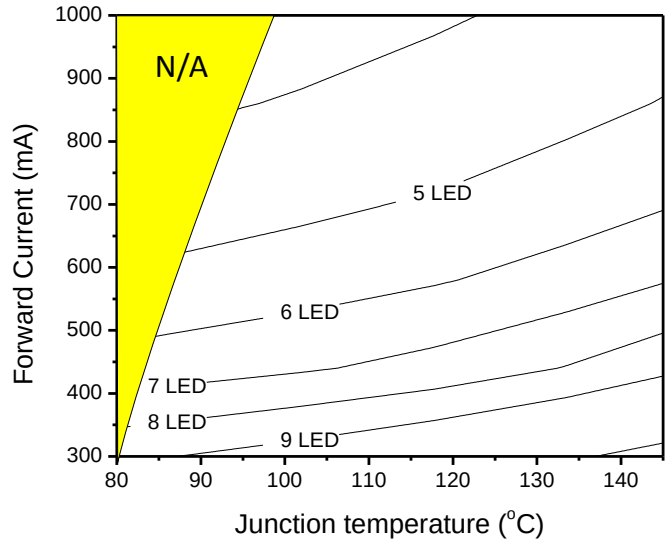

Figure 2.16 Domain of *lumen/LED* for various numbers of LED

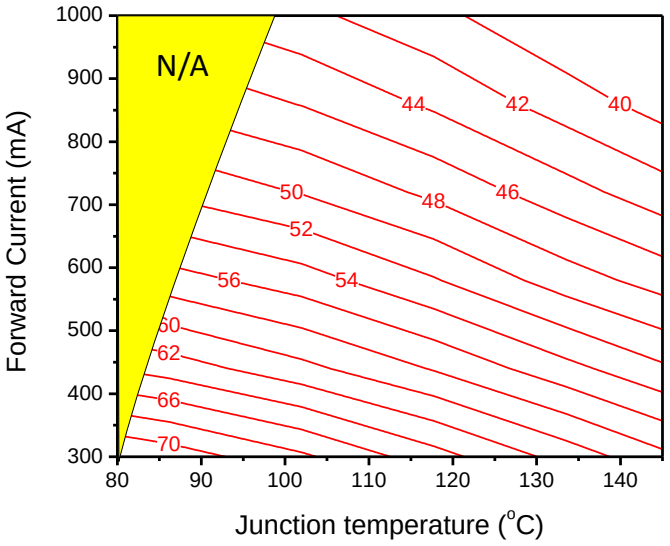

Figure 2.17 Domain of *luminaire efficacy* (lm/W) for wall wash light

The lumen/LED can be converted to "Dollar/Lumen" if an LED price is given. Since wall wash lights illuminate walls, the irradiance parameter (lux) is more important than luminous flux in practice. The luminous flux can be converted to lux if the wall condition and beam angle of the application are given.

Finally the required *L70 lifetime* of 35000 hours is considered. Most LED-based luminaires use secondary optics such as a reflector cup and a polycarbonate lens. The ambient temperature of LED is higher than the air temperature surrounding the luminaire since the LED is confined in the secondary optics. The domain of the *L70 lifetime* considering the ambient temperature of 75 ℃ is shown in Fig. 2.18. It should be noted that the low bound of junction temperatures defined in Sec. 2.2.4 is shown in Figs. 2.16, 2.17 and 2.18 and the domain below the minimum junction temperature is marked as "N/A".

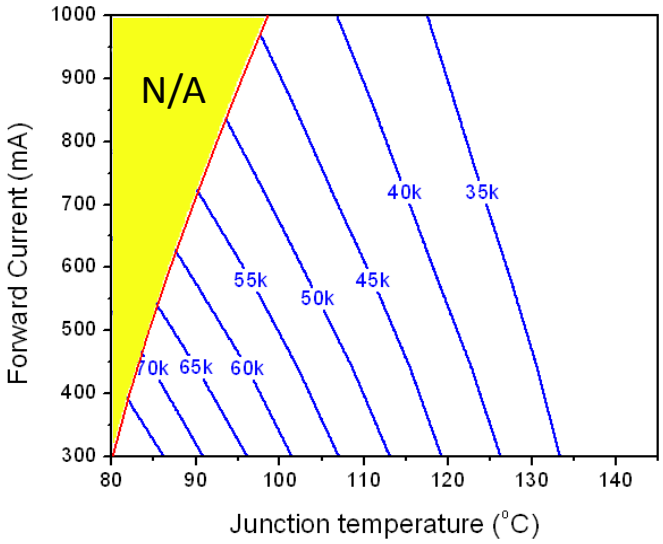

Figure 2.18 Domain of *L70 lifetime* for wall wash light under an ambient temperature of 75 °C.

Figure 2.19 shows design solutions for a wall wash light under an ambient temperature of 75 ℃. Any operating conditions within the area satisfy the requirements for the corresponding number of LEDs. Yet several points in the domain offer solutions that would carry more importance in practice. The solutions indicated by red dots in Fig. 2.19 offer the maximum luminaire efficacy and lifetime within each LED-quantity based solution line: i.e., the lowest current as well as junction temperature. These solutions require a more expensive cooling solution to maintain the low junction temperature. As opposed to these, the solutions indicated by blue dots offer solutions with the most relaxed thermal requirement. The lumen maintenance is obviously compromised in these solutions.

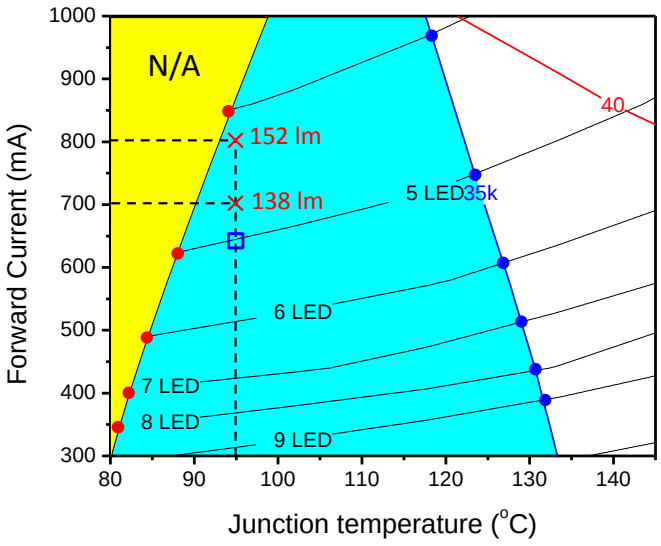

Figure 2.19 Design domain for wall wash light under an ambient temperature of 75 °C: red points represent the solutions for the maximum luminaire efficacy and lifetime; and blue points represent the solutions for the maximum allowable junction temperature.

The optimized operating condition for a given number of LEDs can be chosen along the Lumen/LED lines in Fig. 2.19. This is illustrated for the solution with 5 LEDs. If the junction temperature is to be 95℃, the proper current level should be 645mA (marked as "□" along the 5 LED solution line in Fig. 2.19). If the current levels are higher than the value along the dashed line (marked as "□" in Fig. 2.19) while maintaining the same junction temperature (95 ℃), the luminaire will produce the face lumen higher than the required value (575 lm): at the points marked as "x" the lumen/LED will be 138 and 152 lm and the total luminous flux of the luminaire will be 621 and 684 lumen, respectively. This extra luminous flux will increase the L70 lifetime. It should be noted that this condition requires a better thermal management solution to maintain the same junction temperature.

2.4. CONCLUSION

Design parameters of LED-based luminaires have been analyzed to suggest a design domain that optimizes cost, energy consumption and reliability. The required data sets were Lumen/LED, Luminaire efficacy, and L70 lifetime. The data sets were obtained by measuring the SPD of an LED as a function of forward current as well as junction temperature (I_f and T_j). The minimum junction temperature limit was also defined as a low bound of a valid design domain. The proposed scheme was implemented for a wall wash light and the optimum design solutions were presented. The scheme is general and can be applied to LED–based luminaires with either passive or active cooling solutions.

Chapter 3: Life Prediction of LED-Based Recess Downlight Cooled by Synthetic Jet[3]

Abstract

This paper details the adaptation and implementation of a proposed hierarchical model to the reliability assessment of LED-based luminaires. An Edison base – 6 inch, compatible can, downlight – LED replacement bulb, cooled by an active *synthetic jet,* is used as the test vehicle. Based on the identified degradation mechanisms and the experimentally obtained degradation rate of the cooling device, the reduction in the heat sink enhancement factor, and thus the increase in the LED junction temperature, is determined as a function of time. The degradation mechanisms of the dual-function power electronics – providing constant current to the LEDs and to the drivers of a series of synthetic jets – are also analyzed and serve as the basis for a hybrid model which combines these two effects on the luminaire lifetime. The lifetime of a prototypical luminaire is predicted from LED lifetime data using the degradation analyses of the synthetic jet and power electronics.

[3] This chapter has been published in the *Microelectronics Reliability* under the title of "Life Prediction of LED-Based Recess Downlight Cooled by Synthetic Jet" by B. Song, et al.

3.1. Introduction

Various types of LED based luminaire have been released in the market attracting considerable interest due to advantages such as compact size, high color quality, high luminaire efficacy, and long lifetime compared to conventional light sources (Table 3.1) [51]. Although LEDs are attractive for lighting applications due to the aforementioned advantages, the extreme sensitivity of light output and useful lifetime to the LED junction temperature remains a unique technical challenge. To overcome this challenge, innovative passive and active cooling solutions have been developed continuously and thus the appropriate methodologies to assess the reliability of LED-based luminaires are required.

Table 3.1 Comparison of various luminaires [51]

	Luminous Efficacy (lm/W)	Fixture Efficiency (%)	Luminaire Efficacy (lm/W)	Lifetime (hrs)
Incandescent	10	60	6	3k
CFL	60	40	24	10k
LED	80	77.5 (including driver and thermal efficiency)	62	>50k

Typical LED-based luminaires consist of LED light engine, cooling device, optical component, and power electronics. Each component has unique degradation mechanisms. In order to assess the reliability of the luminaire a hierarchical reliability model was proposed by the authors [52]. In the paper, the concept of the

hierarchical model was described and its implementation was illustrated by assuming some possible degradation mechanisms.

This paper is an extension of our previous research. [52], and details a procedure to adopt and implement the hierarchical model. Section 3.2 describes an LED-based luminaire cooled by a synthetic jet and presents a refined hierarchical model that is specifically aimed for the luminaire. In Section 3.3, the synthetic jet is analyzed in detail and the junction temperature change due to the degradation of the cooling device is evaluated. The effect of power electronics degradation on the luminaire is provided in Section 3.4. Finally, in Section 3.5, the lifetime of the luminaire is predicted from the LED lifetime using the results of the analyses of the previous sections.

3.2. Luminaire and Hierarchical Lifetime Prediction Model

3.2.1. Description of Luminaire

The high brightness (HB) LED-based luminaire analyzed in the paper is shown in Fig. 3.1a [53]. The luminaire is an Edison base, 6 inch compatible can downlight, LED replacement bulb producing 1500 face lumens at 75 lm/W, CRI > 80, CCT = 2700–3200 K [53].

The luminaire is actively cooled by synthetic jets. Synthetic jets are zero net mass flow devices that comprise a cavity or volume of air enclosed by a flexible structure and a small orifice through which air is forced [54, 55]. The structure is induced to deform periodically in a bending mode in a periodic manner causing a corresponding suction and expulsion of the air through the orifice. The synthetic jet

employed in the luminaire is shown in Fig. 3.1b. It comprises two thin piezoelectric actuators separated by a compliant ring. Each piezoelectric actuator comprises a metallic substrate bonded to a piezoelectric material.

In order to deliver the proper beam uniformity and angle of light while satisfying the size constraints, polycarbonate lens are employed. They provide an overlapping beam with approximately 50° beam angle control.

As the power electronics drives the LED light engine as well as synthetic jets, a fly-back converter topology was chosen to provide galvanic isolation between the input ac voltage of 120-V rms at 60 Hz and the output voltages. The fly-back transformer converts an input voltage (with peak value V_i) to dc voltages V_o for the LEDs, V_{cc} for auxiliary electronics that power "house-keeping" circuits, and also the power electronics for synthetic jets [53].

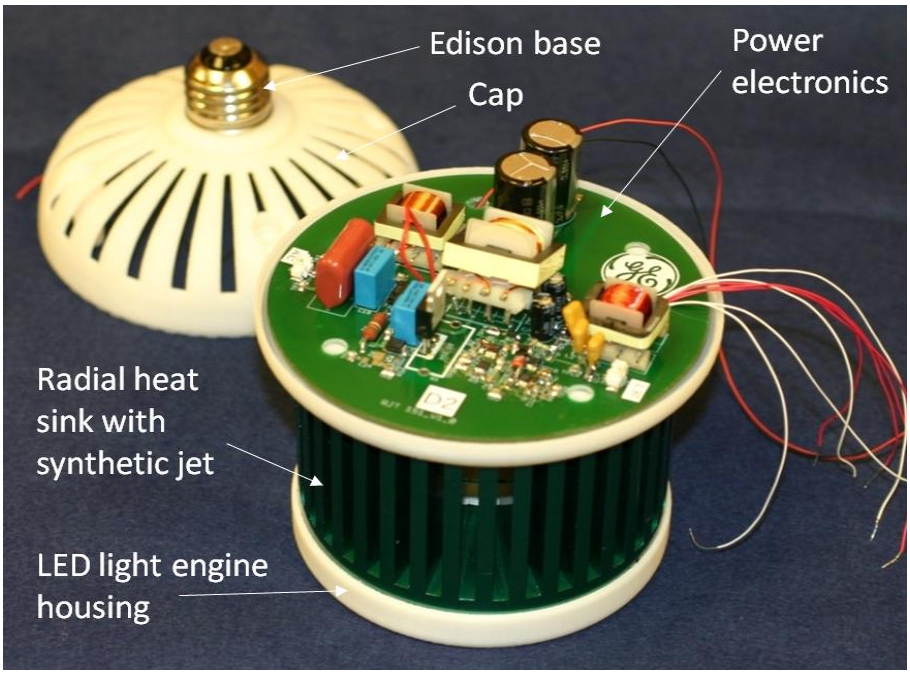

(a)

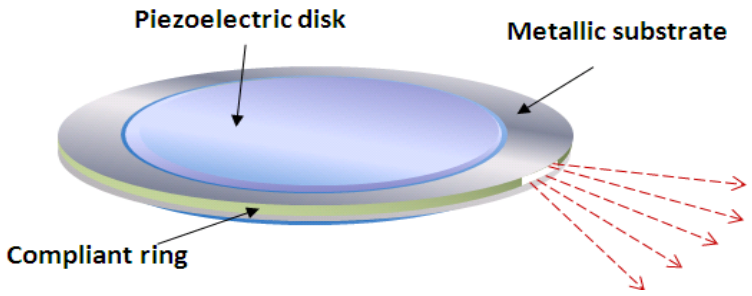

(b)

Figure 3.1 (a) Photo of an LED-based luminaire cooled by synthetic jet [52] and (b) schematic of synthetic jet

3.2.2. Hierarchical Life Prediction Model

The concept of a hierarchical model was proposed in Ref. [52]. A model refined to be specifically aimed for the luminaire of Fig. 3.1a is presented in Fig. 3.2. The model is articulated on four levels: LED chip/package, optical components in the fixture, synthetic jet with a heat sink, and power electronics. Figure 3.2 also shows all the sub-models and the associated loading conditions at each level.

The lifetime of the luminaire is determined by the lumen maintenance of LED and the reduction of the fixture efficiency, which can be expressed as [52]:

$$t_{life} = F\left(g_{LED}(t), F_{fixture}(t)\right) \tag{3.1}$$

where t_{life} = luminaire lifetime at lumen maintenance of 70%, g_{LED} = lumen maintenance of LED, and $F_{fixture}$ = fixture efficiency.

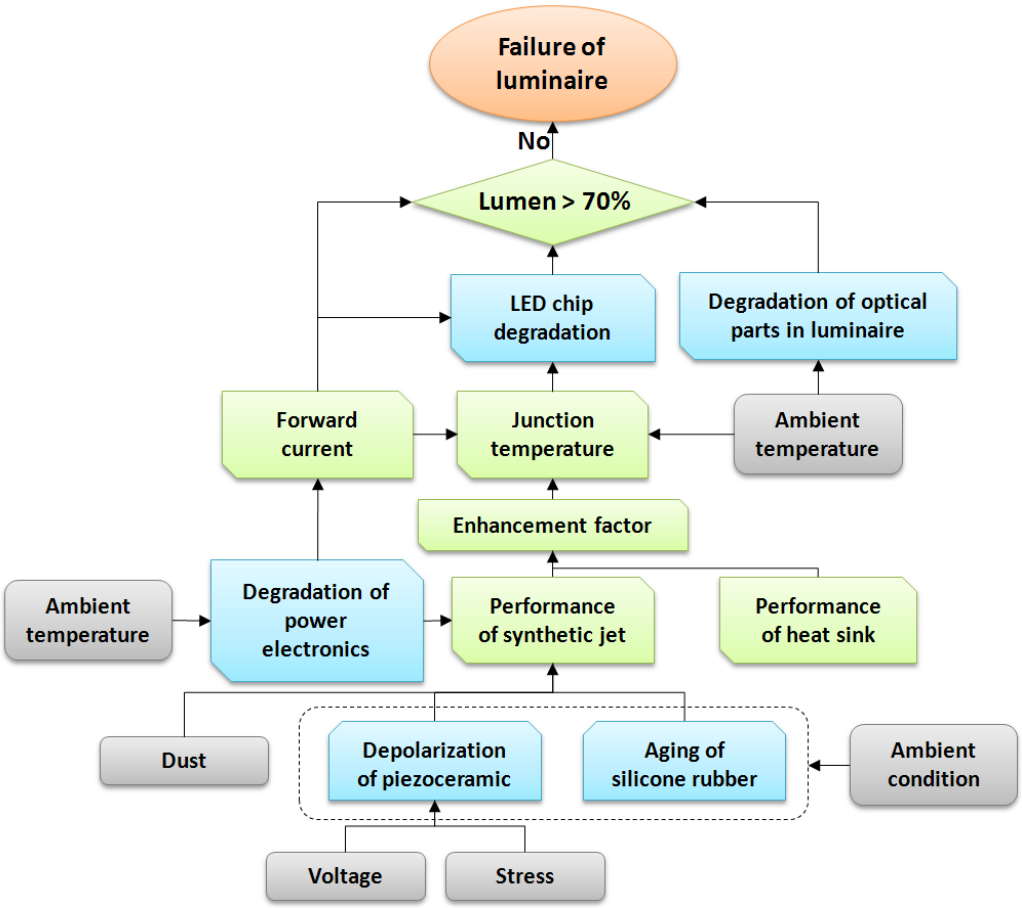

Figure 3.2 Hierarchical life prediction model for LED-based luminaire cooled by synthetic jets

The lumen maintenance of LED is the most critical sub-model, which has an empirical exponential form. The light output of LEDs, L_{LED}, can be expressed mathematically as:

$$L_{LED} = L_0 g_{LED}(t) = L_0 e^{-\alpha(T_j, I_f)t} \tag{3.2}$$

where α is the light output degradation rate that depends on the junction temperature (T_j) and the forward current (I_f) [6, 7, 23], t is the operation time measured in hours, and L_0 is the initial light output in lumen [3, 56].

The cooling performance of synthetic jets is expressed with an enhancement factor (*EF*) which is defined as the ratio of heat removed with an active cooling device (Q_{active}) to the heat removed through passive means only, largely through natural convection (Q_{nc}), at the same temperature, i.e., $EF = \frac{Q_{active}}{Q_{nc}}$. Considering the fact that the junction temperature increases as the ambient temperature and forward current increase, the dependence of the junction temperature on the aforementioned terms can be expressed as [52]:

$$T_j = T(T_a, R_{cond}, I_f, EF) \tag{3.3}$$

where $T_a =$ ambient temperature; $R_{cond} =$ internal conduction resistance of LED.

The power electronics drives the LED light engine and the synthetic jet. The degradation of power electronics is mainly caused by capacitance reduction of electrolytic capacitors. The reduced capacitance increases the ripple voltage, and thus the applied current to LED is reduced [57]. The decreased current affects the light output and junction temperature. As mentioned above, the decay constant is a function of forward current; as a result the decay constant decreases with the decreasing current.

The remaining sub-models of the proposed hierarchical model are physics-of-failure (PoF) models to describe the degradation mechanisms of the synthetic jet performance. The PoF models of the synthetic jet degradation can be separated into depolarization of the piezoceramic disk and aging of the compliant ring. The degradation mechanisms change the amplitude response of the synthetic jet, thereby reducing the *EF* at any given time.

3.3. Reliability Analysis of Synthetic Jet

The degradation of synthetic jet performance (i.e., the reduction in amplitude) increases the junction temperature of the luminaire, which is a dominant factor for the lifetime of the luminaire. After developing a model that can predict amplitude response, the time-dependent performance of the synthetic jet can be predicted by aging characteristics of each component in the synthetic jet. The performance change is then converted into the junction temperature change using the relationships between the amplitude of the synthetic jet and junction temperature.

3.3.1. Performance Characterization

The performance of the synthetic jet was tested by applying a harmonic voltage input at various frequencies. The center out-of-plane displacement amplitudes of the disk were measured by a laser doppler vibrometer [CLV-1000, Polytech].

The junction temperature is directly related to the performance of the synthetic jet and the heat sink. The enhancement factor (*EF*) is proportional to the amount of air-flow rate, which is a function of the amplitude of the jet and the excitation frequency.

Assuming that the deflection of the disk can be modeled as a part of a perfect sphere, the air flow rate can be approximated as (Fig. 3.3):

$$AFR = 4\pi \left\{ \frac{(R-a)^3 - R^3}{3} + R^2 a \right\} \times f_{jet} \tag{3.4}$$

where *AFR* = air flow rate; f_{jet} = operating frequency of synthetic jet; *a* = amplitude of synthetic jet; and *b* = radius of nickel coated substrate. Geometrical considerations require that, the radius of the sphere, *R*, be expressed as $R = \frac{a^2 + b^2}{2a}$.

A relationship between the *EF* and the air-flow rate is depicted in Fig. 3.4a, which was obtained by changing the amplitude of the disk (or by changing the amplitude of the excitation voltage) at a fixed excitation frequency. In order to determine the junction temperature for a given *EF*, an empirical relationship should be obtained for each synthetic jet and heat sink design. Figure 3.4b shows such a relationship, obtained from synthetic jets incorporated with a radial heat sink.

The enhancement factor decreases as the synthetic jet ages. The aging is caused by two degradation mechanisms: depolarization of the piezoceramic and change in the elastic modulus and damping ratio of the compliant ring. This can be expressed as:

$$EF = EF(P_{jet}); \quad P_{jet} = P_{jet}(T_a, D_{pzt}, E_{td}, \zeta_{td}, P_{ps}) \tag{3.5}$$

where P_{jet} = performance of jet; D_{pzt} = depolarization effect of piezoceramic; E_{td} = elastic modulus change of compliant ring ; ζ_{td} = damping ratio change of compliant ring; and P_{ps} = performance of synthetic jet driving circuit.

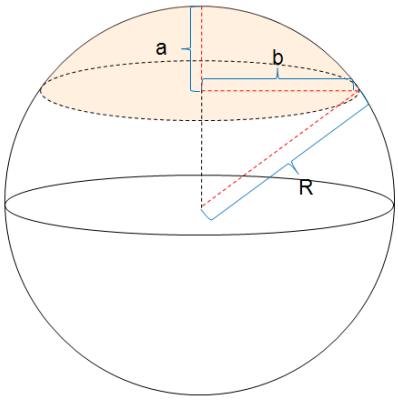

Figure 3.3 Air volume in a synthetic jet (colored region), where *a* = amplitude of synthetic jet, *b* = radius of metal substrate and *R* = radius of a sphere.

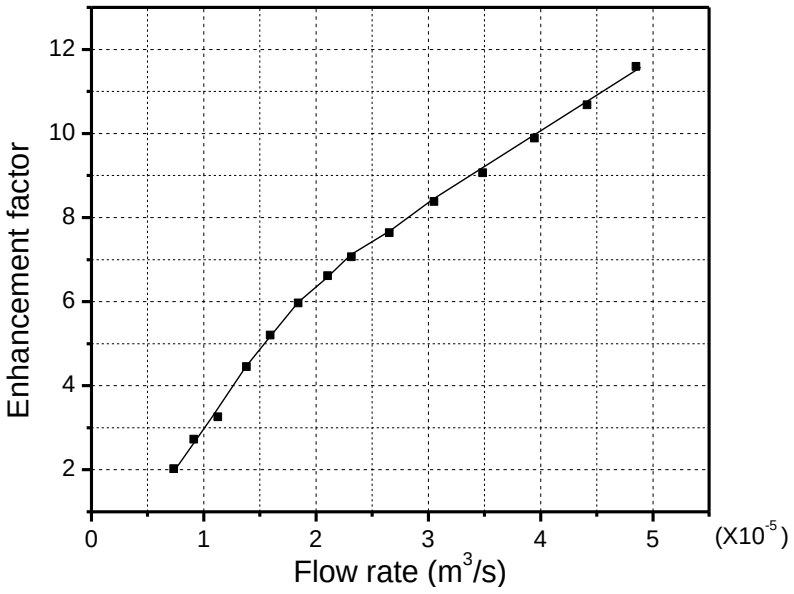

(a)

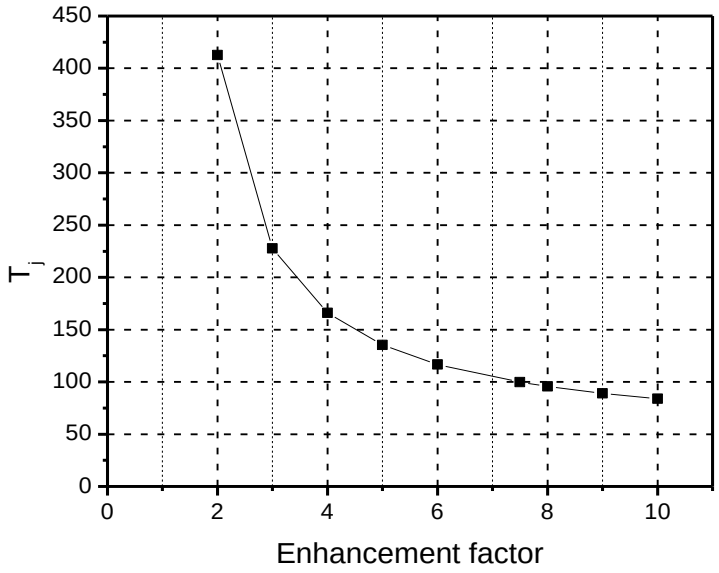

(b)

Figure 3.4 (a) Air flow rate vs. enhancement factor (EF) and (b) EF vs. junction temperature

3.3.2. Hybrid Modeling

The amplitude reduction can be predicted using numerical modeling if the degradation rates of the piezoelectric disk and the compliant ring are known. A hybrid experimental/numerical model is developed to predict the amplitude reduction as a function of time by adopting the property degradation characteristic of each material used in the synthetic jet.

A commercial FEM package (ANSYS 12.1) was used to build an FEM model for a harmonic analysis using the quarter symmetry (Fig. 3.5a). In order to incorporate the material damping, Rayleigh damping was used [58], which can be expressed as:

$$\zeta_{mr} = \frac{\alpha}{2\omega_R} + \frac{\beta\omega_R}{2} \tag{3.6}$$

where ζ_{mr} is the r^{th} modal damping ratio, ω_R is the resonant frequency in rad/s, α is the mass damping multiplier, and β is the stiffness damping multiplier. Since α is zero for the current case of viscous damping [58], Eq. (3.6) can be rewritten as:

$$\beta = \frac{2\zeta_{mr}}{\omega_R} \tag{3.7}$$

The damping ratio of each material in the synthetic jet was converted to β by using Eq. (3.7). Figure 3.5b shows the comparison between simulation and experimental result at vacuum condition. The simulation result is in good agreement with experimental results.

The ambient pressure at the operating condition is 1 atm and thus the effect of the air damping known as "squeeze film damping" [59] must be considered in the modeling. Squeeze film damping occurs when two surfaces separated by a thin viscous fluid film move symmetrically. This effect is illustrated in Fig. 3.6a, where the amplitude response of the synthetic jet at 1 atm and the vacuum are compared. As expected, the resonant frequency and the amplitudes were altered significantly with damping: the resonant frequency decreased and the amplitude at the resonant frequency also decreased.

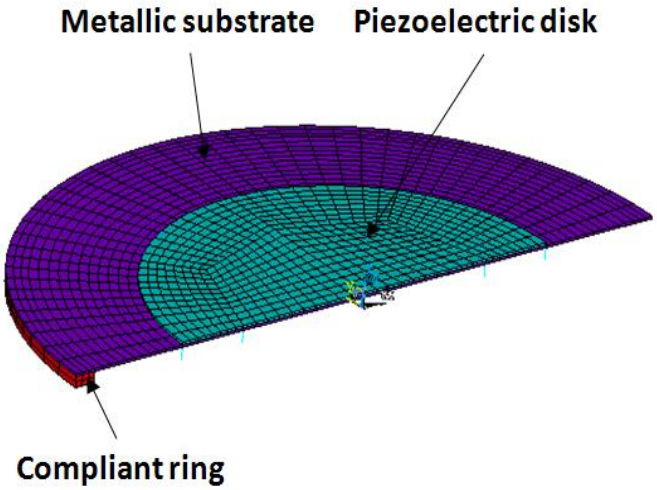

(a)

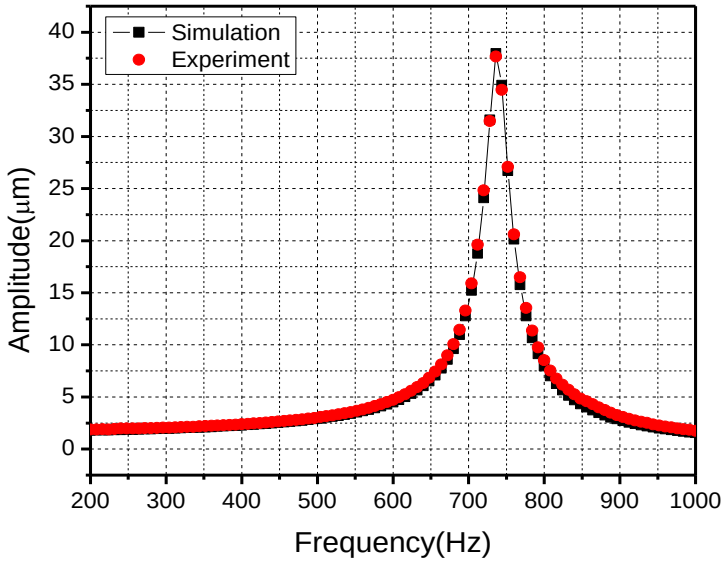

(b)

Figure 3.5 (a) FEM model of a synthetic jet for harmonic analysis using the quarter symmetry and (b) experimental data obtained at vacuum is compared with simulation results considering only material damping

The data of Fig. 3.6a was normalized and plotted again in Fig. 3.6b to distinguish the characteristics of amplitude distributions more clearly. The frequency

and the amplitude were normalized by the resonant frequency of each case and the amplitude at the resonant frequency, respectively. It can be seen from Fig. 3.6b that the amplitudes at frequencies other than the resonant frequency tend to decrease more slowly with the air damping, especially at the frequencies higher than the resonant frequency ($f > f_R$). An advanced CFD model can be used to handle the squeeze film damping effect. In this study, a hybrid numerical/experimental scheme was developed since the reliability model only concerned the final amplitude.

The rationale for the hybrid approach can be explained by comparing the numerical prediction of synthetic jet with the experimental data. The goal of the approach is to force the numerical prediction to match the experimental data by effectively adjusting the original properties to account for the effect of squeeze film damping.

The jet is essentially a second order system subjected to a sinusoidal input. The resonant frequency of the second order system, ω_R, is expressed as [60]:

$$\omega_R = \omega_n \sqrt{1-2\zeta^2} = \sqrt{\frac{k}{m} - \frac{c^2}{2m^2}} \tag{3.8}$$

where m is the mass, c is the damping coefficient, k is the stiffness, ζ is the damping ratio ($\zeta = \frac{c}{2\sqrt{km}}$), and ω_n is the natural frequency ($\omega_n = \sqrt{\frac{k}{m}}$). For a given mass, the resonant frequency can be changed by adjusting the stiffness or the damping coefficient.

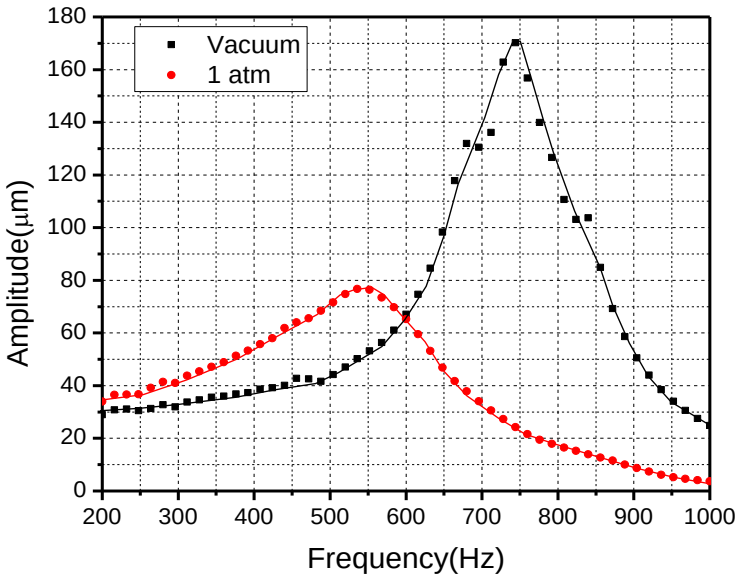

(a)

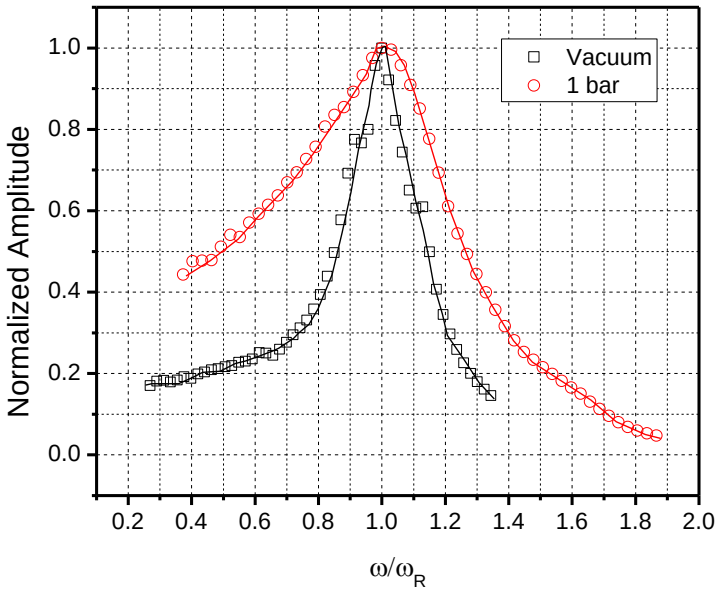

(b)

Figure 3.6 Squeeze film damping effect in synthetic jet: (a) Comparison between with and without squeeze film damping effect and (b) normalized plot of (a) where the frequency is normalized by the resonant frequency and amplitude is normalized by the amplitude at the resonant frequency.

The amplitude of the second order system subjected to a harmonic excitation is expressed as [60]:

$$X = \frac{F_0}{k} \frac{1}{\sqrt{\left\{1-\left(\frac{\omega}{\omega_n}\right)^2\right\}^2 + \left\{2\zeta\left(\frac{\omega}{\omega_n}\right)\right\}^2}} = \frac{F_0}{\sqrt{\left\{k-\omega^2 m\right\}^2 + \left\{\frac{\omega^2 c^4}{4mk}\right\}}} \tag{3.9}$$

where X is the amplitude at each frequency, F_0 and ω are the excitation force and frequency, respectively. Equation (3.9) implies that the most practical way of adjusting the amplitude is to manipulate the force. Then the amplitude normalized by the amplitude at the resonant frequency can be expressed as:

$$\bar{X} = \frac{X}{X_R} = \sqrt{\frac{\left(\frac{kc^2}{m}\right) - \left(\frac{c^4}{4m^2}\right)}{\left\{k-\omega^2 m\right\}^2 + \left\{\frac{\omega^2 c^4}{4mk}\right\}}} \tag{3.10}$$

For a given mass, the normalized amplitude can also be changed by adjusting the stiffness or the damping coefficient.

A sequential optimization procedure was developed for the hybrid approach. The flowchart is shown in Fig. 3.7 and the detailed description of each step is provided below.

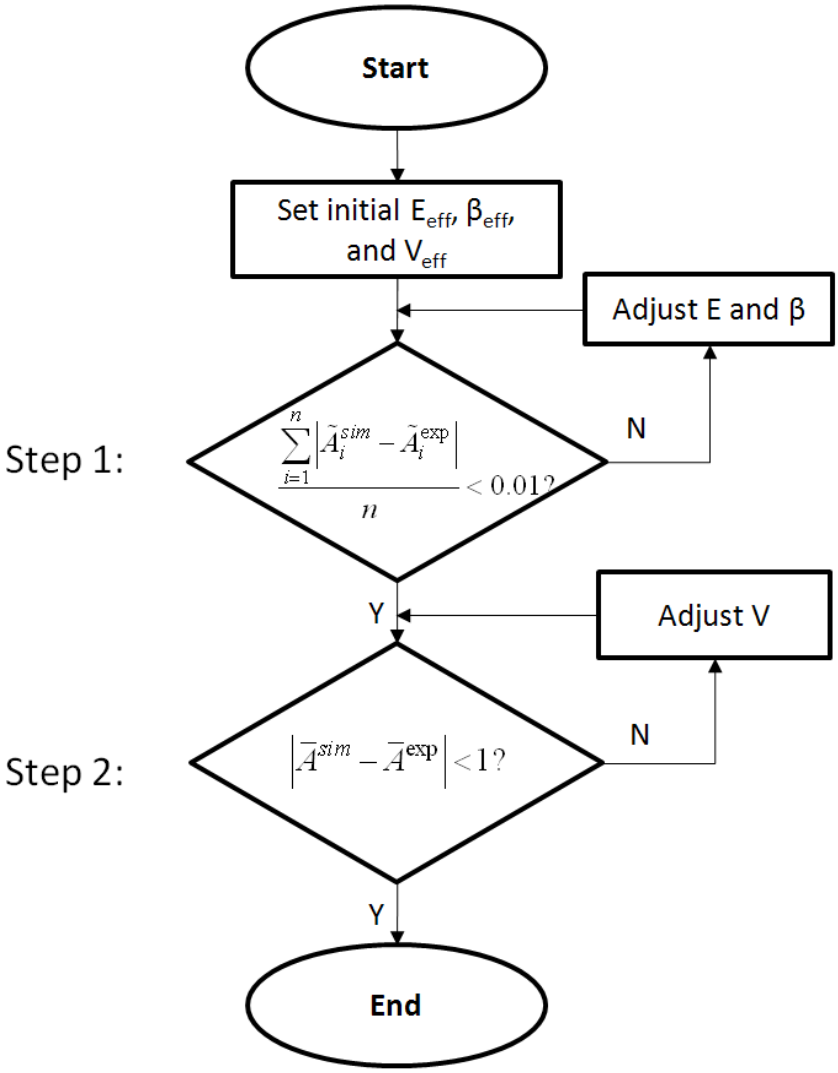

Figure 3.7 Flow chart to determine effective properties for the hybrid model

- **Step 1: Profile of normalized amplitude**

Since the elastic and damping properties of the piezoceramic disk/substrate assembly do not change with time, the effective modulus and the stiffness damping multiplier of the assembly are used to modify the system stiffness and the damping.

The effective properties of the piezoceramic disk/substrate assembly can be expressed as:

$$E_{eff} = \frac{E_{sub}V_{sub} + E_{PZT}V_{PZT}}{V_{sub} + V_{PZT}}$$
$$\beta_{eff} = \frac{\beta_{sub}V_{sub} + \beta_{PZT}V_{PZT}}{V_{sub} + V_{PZT}} \quad (3.11)$$

where E , β and V represent the modulus, the stiffness damping multiplier and the volume, respectively. The subscripts of "sub" and "PZT" denote the substrate and piezoelectric disk, respectively.

The objective of this step is to adjust the amplitude response. The amplitude data normalized by the maximum amplitude was used to determine an effective E-β combination by using an optimization routine. The objective function (R_1) can be expressed as:

$$R_1 = \frac{\sum_{i=1}^{n} \left| \tilde{A}_i^{\exp} - \tilde{A}_i^{sim} \right|}{n} \quad (3.12)$$

where $\tilde{A}^{\exp}$ and $\tilde{A}^{sim}$ are the amplitudes of experimental and simulation data normalized by each maximum, respectively; and n is the number of data points. The optimization routine adjusts the E-β combination until the objective function has the minimum value. Figure 3.8a shows the results obtained using the effective E-β set at an input voltage of 30V.

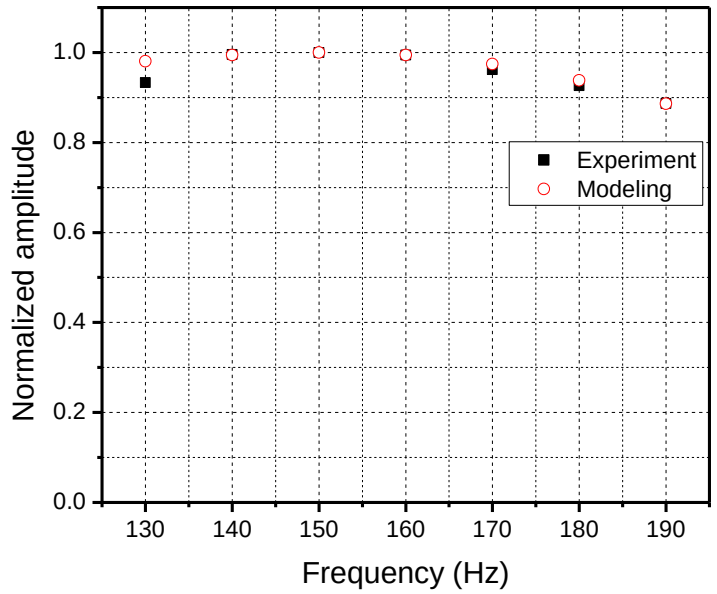

(a)

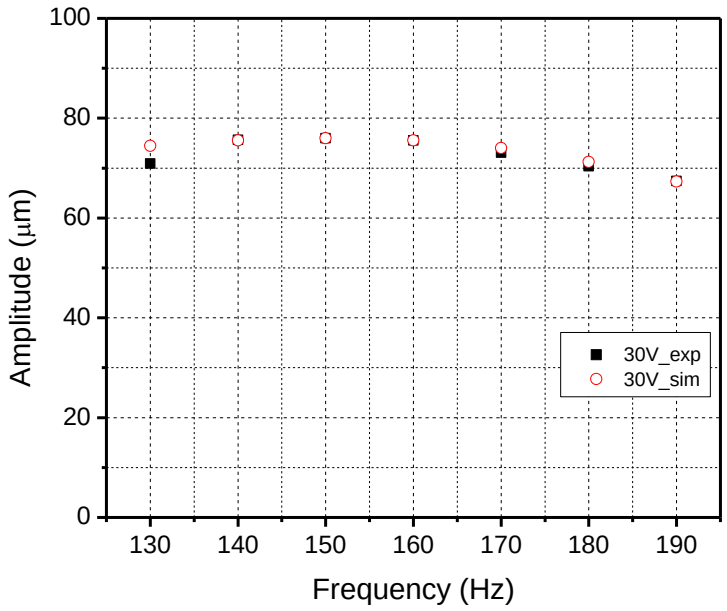

(b)

Figure 3.8 Results of hybrid model at an input voltage of 30V: (a) normalized amplitudes and (b) absolute amplitudes.

- **Step 2: Absolute amplitude**

The absolute amplitude level can be adjusted by changing the input voltage. The objective function (R_2) for the optimized V quantifies the degree of coincidence between the experimental and the simulated data. The metric can be expressed as:

$$R_2 = \left| \bar{A}_{\exp} - \bar{A}_{sim} \right| \tag{3.13}$$

where $\bar{A}_{\exp}$ and $\bar{A}_{sim}$ is the average amplitude of all the experimental and the numerical data points, respectively.

The optimum combination of the effective properties and the input voltage is computed and the result obtained is compared with the experimental data in Fig. 3.8b. The result corroborates the effectiveness of the hybrid approach.

3.3.3. Depolarization of Piezoelectric Disk

The depolarization of the piezoelectric disk is attributed to the applied voltage, the mechanical stress, and the ambient temperature. If significant, it reduces piezo-coupling and thus reduces the amplitudes. In order to characterize the depolarization effect, three groups of synthetic jets have been tested for 3000 hours at three different temperature conditions (60, 90 and 120℃). The planer coupling coefficient which indicates the amount of polarization property has been measured during operation.

Figure 3.9 shows the experimental results. The coupling coefficient decreased initially but stabilized at 0.9, 0.86 and 0.81 for 60, 90 and 120 ℃, respectively. The results confirm that the effect of depolarization on the piezoceramic disk is not significant and thus it will not be considered when the performance of the synthetic jet is to be evaluated in the PoF model.

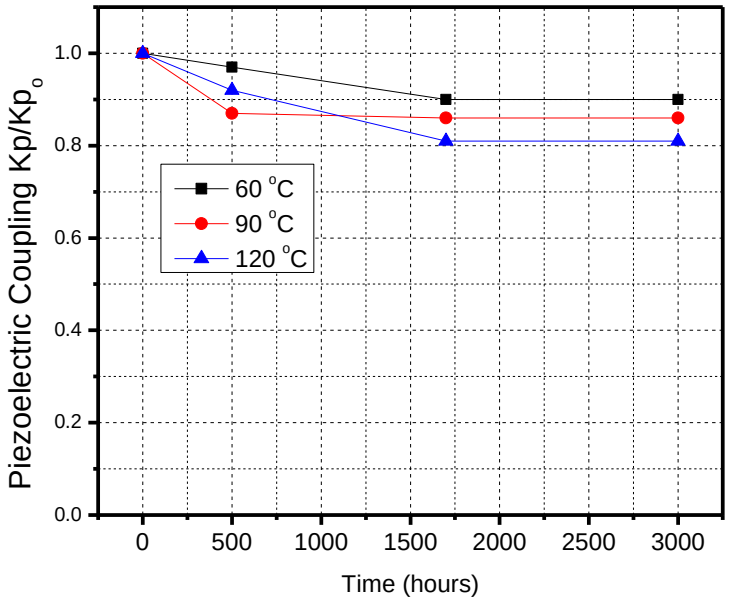

Figure 3.9 Coupling coefficient of piezoelectric disk during aging

3.3.4. Aging of Compliant Ring

For most polymers in oxygen-containing environments, oxidation is the dominant factor in aging [61]. The ductile polymer material becomes brittle due to the chemical reaction; the material modulus increases and the damping ratio decreases. In order to predict the material property change of polymer as a function of time and temperature, the Arrhenius relation, which is well known in chemical kinetics, can ascertain thermo-oxidative aging of polymers.

3.3.4.1. Time/Temperature Superposition Method

The principle of time/temperature superposition was adopted to characterize the aging of the compliant ring. The time/temperature superposition is a well known

procedure, which can be applied to verify the temperature dependence of the rheological behavior of a polymer or to expand time or frequency regime for a polymer at a test temperature. This is accomplished by multiplying the data points from the experiment with a shift factor a_T at a temperature of interest. The shift factors a_T are chosen empirically, to give the best superposition of the data. The shift factors a_T are related to the Arrhenius activation energy, E_a, by the following expression [61]:

$$a_T = \exp \frac{E_a}{R}\left(\frac{1}{T_{ref}} - \frac{1}{T}\right) \tag{3.14}$$

where a_T is the shift factor, E_a is the activation energy, R is the Boltzmann constant, T_{ref} is the reference temperature, and T is the testing temperature.

Equation (3.14) can be rewritten as:

$$\ln(a_T) = \frac{E_a}{R}\left(\frac{1}{T_{ref}} - \frac{1}{T}\right) \tag{3.15}$$

By plotting three shift factors using Eq. (3.15), the activation energy is obtained from the slope of the linear relationship.

3.3.4.2. Accelerated Test for Compliant Ring

In order to characterize the aging behavior of the compliant ring, aging test has been conducted. Three different aging temperatures (230, 250 and 275 ℃) have been selected to accelerate the aging rate. Ten specimens have been exposed to each temperature. DMA tensile tests were conducted to measure the storage modulus and the loss tangent (tan δ) at 175 Hz at various time intervals.

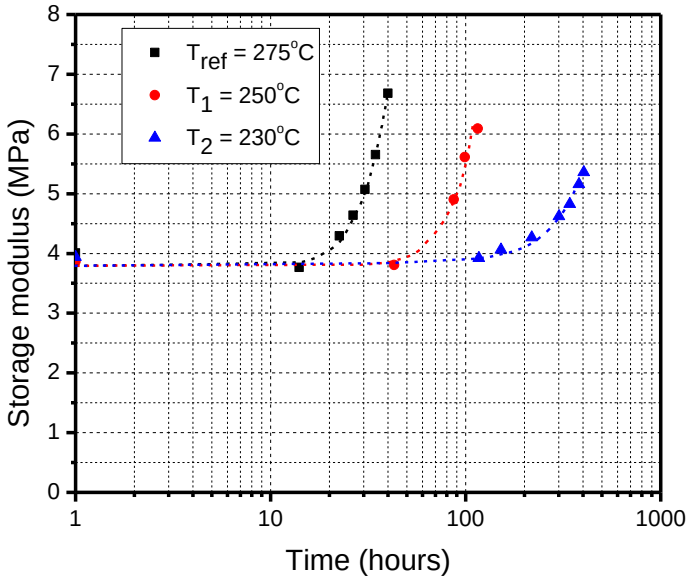

(a)

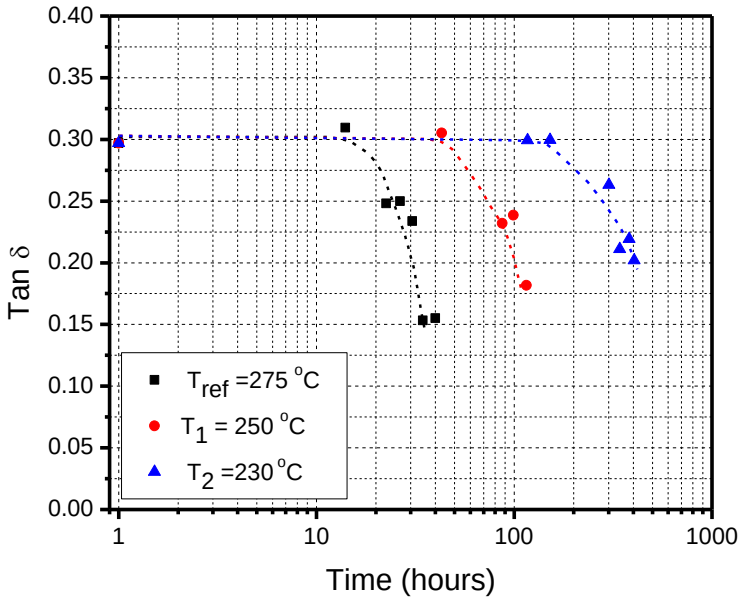

(b)

Figure 3.10 (a) Storage modulus and (b) tan δ over time at different aging temperatures

Figure 3.10 shows the storage modulus and the loss tangent, changes over time at the three different aging temperatures. Each data point represents the average value of 10 specimens. The principle of time/temperature superposition was implemented with the reference temperature of 275℃. All other curves were shifted to the curve at 275℃ to determine the shift factors.

The shift factors for the storage modulus and loss tangent were plotted in Fig. 3.11(Eq. (3.15)). The slopes of linear lines represent the activation energies (E_a): the activation energies of the storage modulus and the loss tangent are 126 kcal and 128 kcal, respectively.

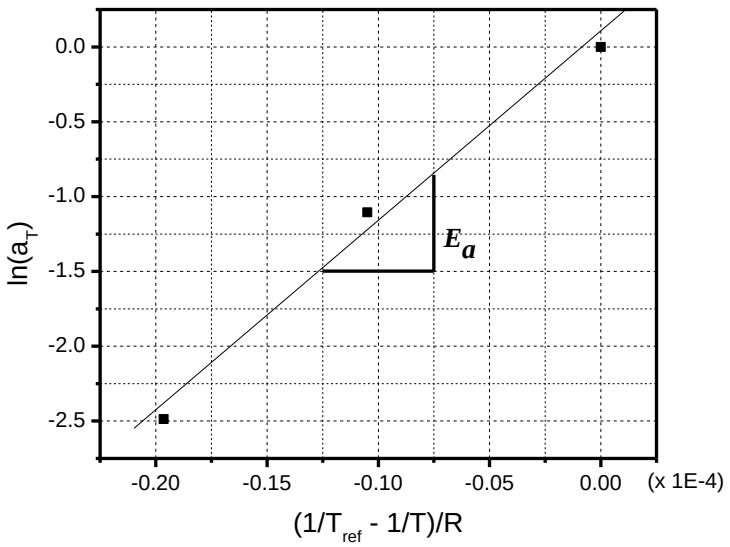

(a)

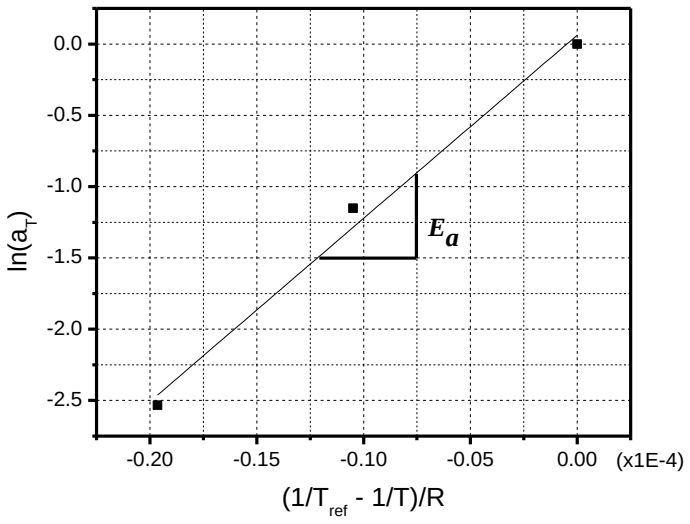

(b)

Figure 3.11 Activation energies of (a) storage modulus and (b) tan δ

The data shifted by the shift factors are shown in Fig. 3.12. The results clearly indicate that the time/temperature superposition is valid for the data. The master curves for the storage modulus and the loss tangent can be expressed by the following exponential functions:

$$E(t;T) = A\exp\left(\frac{a_T(T)}{B}t\right) + E_0 \tag{3.16}$$

$$\tan\delta(t;T) = C\exp\left(\frac{a_T(T)}{D}t\right) + \tan\delta_0 \tag{3.17}$$

where $E(t;T)$ and $\tan\delta(t;T)$ are the time-dependent modulus and the loss tangent at a given temperature T. Three unknown constants (A, B and E_0) for the storage modulus and (C, D and $\tan\delta_0$) for the loss tangent can be determined by a non-linear regression analysis: the constants for Eq. (3.16) and (3.17) are summarized in Table

3.2. The function described by Eq. (3.16) and (3.17) are also shown in Fig. 3.12(a) and (b), respectively.

The actual operating temperature of the synthetic jet is 55 ℃ [53]. The shift factor for 55℃ was obtained from Eq. (3.14): 8.63 x 10^{-9} and 6.55 x 10^{-9} for the storage modulus and tan δ, respectively. The change in storage modulus and loss tangent were subsequently predicted by Eq. (3.16) and (3.17) and the results are shown in Fig. 3.13(a) and (b). The storage modulus is predicted to be 3.8 MPa at 50,000 hours while the loss tangent does not show any noticeable change.

Table 3.2 Constants of master curves of modulus and tan δ

Constant	Value
A	0.103
B	-11.9
E_0	3.70
C	-0.00178
D	-8.63
$tan\ \delta_0$	0.298

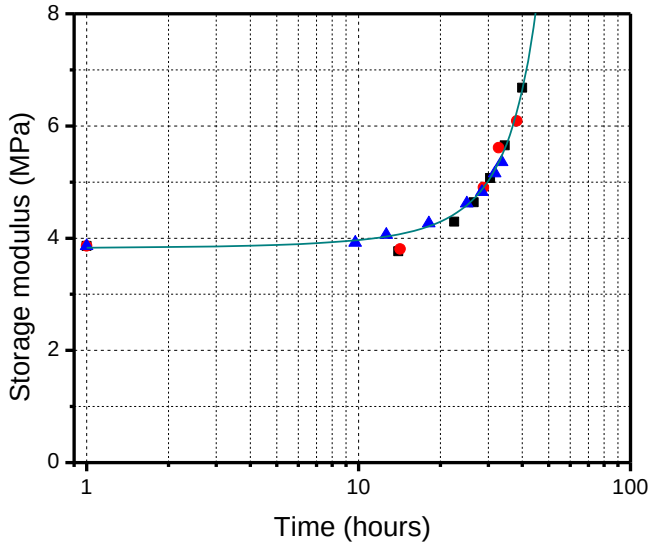

(a)

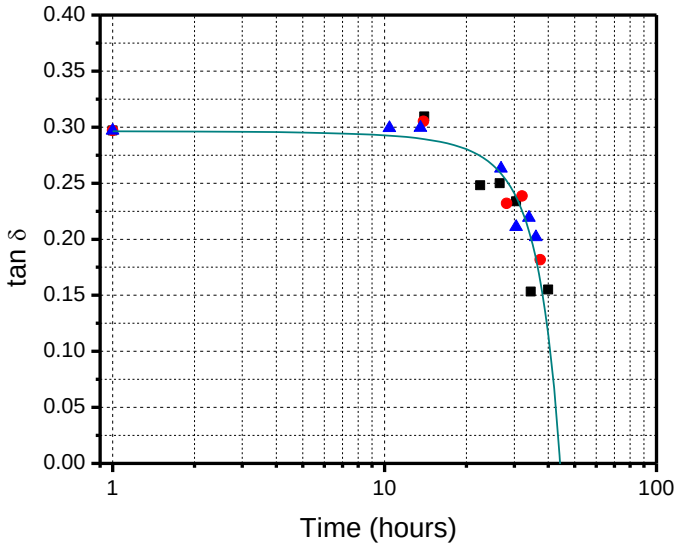

(b)

Figure 3.12 Master curves of (a) storage modulus and (b) tan δ obtained from Fig. 10 where the reference temperature is 275℃.

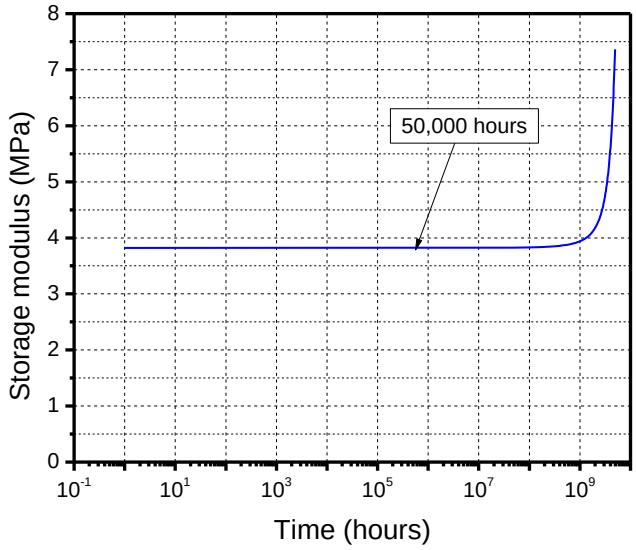

(a)

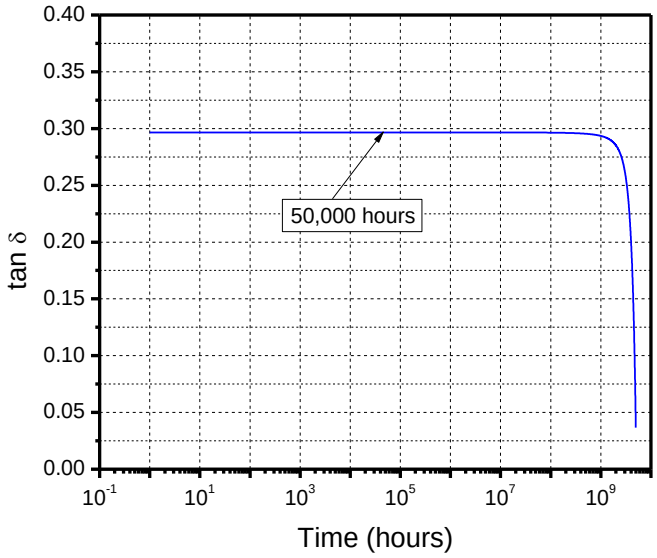

(b)

Figure 3.13 (a) Storage modulus and (b) tan δ at 55℃ as a function of time

3.3.5. Prediction of Junction Temperature vs. Time

The amplitude change of the synthetic jet is shown in Fig. 3.14a. The amplitude data is converted to the air flow rate (Eq. (3.4)) and the air flow rate is

subsequently converted to enhancement factor (*EF*) using the empirical relationship between EF vs. air flow rate (Fig. 3.4a). The *EF* is plotted in Fig. 3.14b. Finally, the junction temperature is determined from the relationship between the junction temperature and the *EF* (Fig. 3.4b). The result is shown in Fig. 3.14c. The junction temperature remains nearly the same after 50,000 hours.

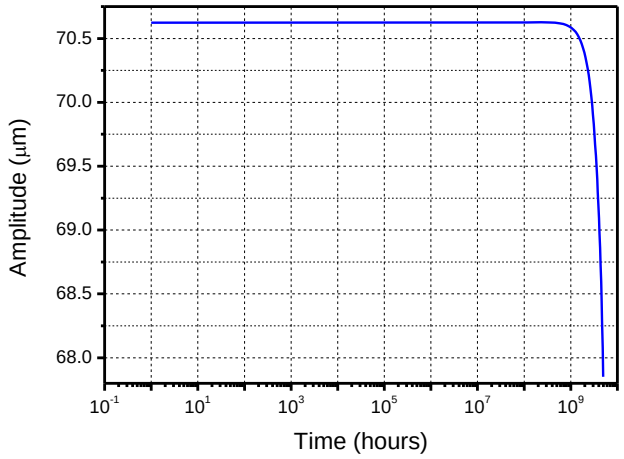

(a)

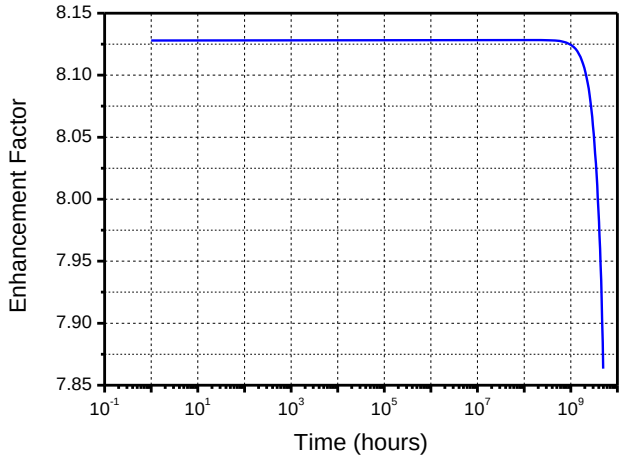

(b)

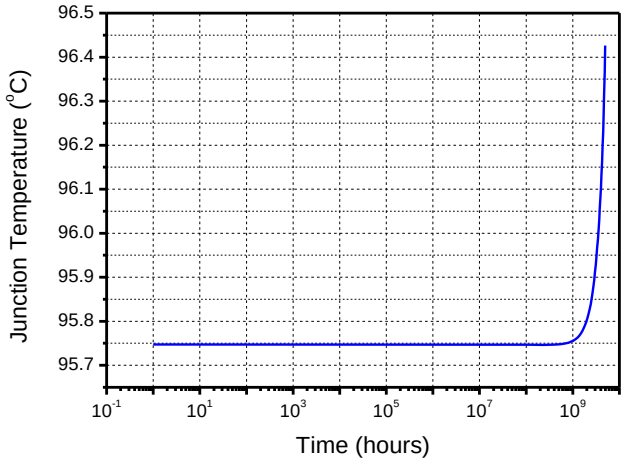

(c)

Figure 3.14 (a) Amplitude, (b) enhancement factor and (c) junction temperature as a function of time

3.4. Analysis of Power Electronics

The reliability of power electronics is critical to the operation of the synthetic jet and LED light engine. The analysis of the power electronics in this section is limited only to the degradation mechanisms that cause output voltage drop; the breakages of other passive devices that cause catastrophic failure of the circuits is not considered.

3.4.1. Synthetic Jet Driving Circuit

The synthetic jet driving circuit is a resonant circuit, which provides an excitation voltage of ±30V at 175 Hz of frequency. The piezoceramic disks in the synthetic jets act as one of the capacitors in the circuit. The capacitance of the piezoceramic disk can be degraded over time [62, 63], which in turn can change the operating voltage of the driving circuit.

The impedance of the resonant circuit can be expressed as:

$$X_{total} = \sqrt{R^2 + (2\pi fL - \frac{1}{2\pi fC_{total}})^2} \tag{3.18}$$

where X_{total} is the impedance of the circuit in ohms, R is the resistance in ohms, f is the frequency in Hz, L is the inductance in henrys, and C_{total} is the total capacitance of capacitors in the circuit and a synthetic jet in parallel in farads. Then the current (I) of the circuit is expressed as:

$$I = \frac{V}{X_{total}} \tag{3.19}$$

where V is input voltage. Table 3.3 shows the actual values of the passives used in the circuit.

Table 3.3 Values of passives in the jet driving circuit

Component	Value
R	200 Ω
L	500 mH
C_{jets}	565 nF
$C_{circuit}$	1220 nF

The applied voltage to synthetic jet then becomes:

$$V_{jets} = IX_C = \frac{I}{2\pi fC_{total}} = \frac{V}{2\pi f\left(C_{circuit} + C_{jets}\right)\sqrt{R^2 + (2\pi fL - \frac{1}{2\pi f\left(C_{circuit} + C_{jets}\right)})^2}} \tag{3.20}$$

where V_{jets} is the applied voltage to synthetic jets and X_C is the impedance of the total capacitance.

The effect of capacitance reduction of synthetic jet (C_{jets}) on applied voltage (V_{jets}) is shown in Fig. 3.15. The initial capacitance of synthetic jet was 565 nF and

the voltage was about 30V. The result shows that the voltage remains about 30V even when the capacitance of synthetic jet becomes 0. The capacitance degradation of piezoceramic disk does not have a significant effect on the applied voltage in the synthetic jet.

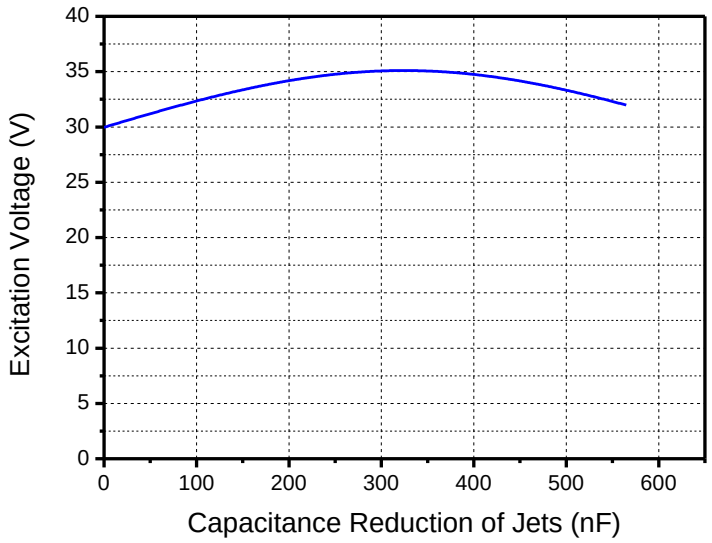

Figure 3.15 Effect of SJ capacitance reduction on excitation voltage

3.4.2. LED Driving Circuit

The current design of power electronics which drives LED light engine is composed of many electronic components such as capacitors, diodes, resistors, inductors and transistor-transistor logic (TTL). The most critical parts have been identified as electrolytic capacitors [64-67]. The effect of electrolytic capacitor degradation on the LED driving circuit is evaluated.

The LED drive circuit supplies a constant power to the LEDs, which are connected in series, set by the DCM (Discontinuous Conduction Mode) operation of

the standard flyback converter. Any fluctuation of the voltage output will thus affect the current through the LEDs [57]. The current fluctuation can be estimated by the forward voltage and the current relationship [10, 26] assuming that the LED impedance remains constant over the range of voltage fluctuation. The major source of voltage fluctuation is the ripple voltage magnitude in the dc output.

The forward voltage oscillates between V_{max} and V_{min}; the magnitude of ripple voltage, V_r, is $V_{max} - V_{min}$. The amount of ripple voltage can be estimated through the relationship between the capacitance and the ripple voltage, which is expressed as:

$$V_r = \frac{I}{2fC} \tag{3.21}$$

where V_r is the ripple voltage, I is the current, f is the frequency, and C is the capacitance of capacitors in the circuit. Then the average voltage (V_{ave}) can be expressed as:

$$V_{ave} = V_{\max} - \frac{V_r}{2} \tag{3.22}$$

The capacitance degradation can be expressed as [37]:

$$C = C_0\left(Ee^{-\frac{t}{t_1}} + F\right) \tag{3.23}$$

where C is capacitance, C_0 is initial capacitance, t is time and E, t_1 and F are constants. The data in Ref. [10, 26] was also used as a conservative representation of the capacitance degradation. The percentage drop of the capacitance based on the function is shown in Fig. 3.16a.

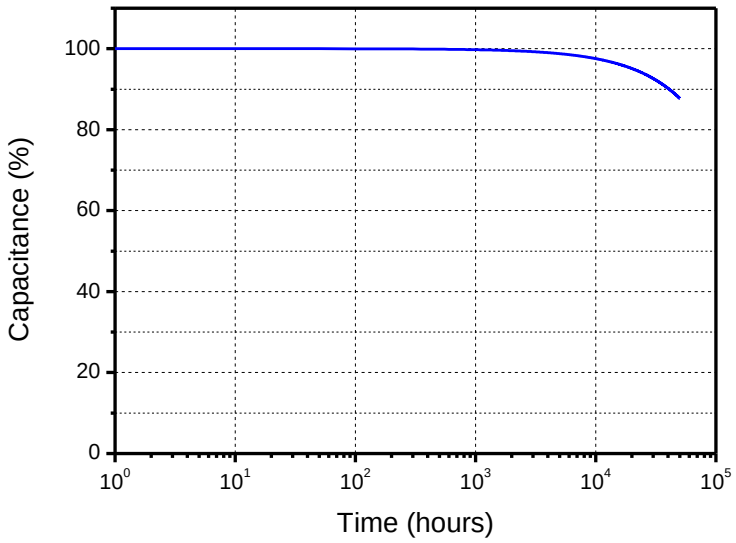

(a)

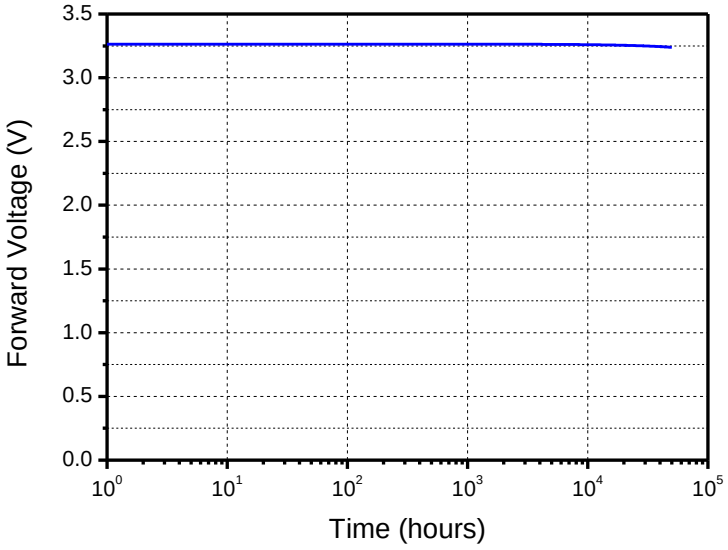

(b)

Figure 3.16 Reduction as a function of time: (a) capacitance and (b) forward voltage

The voltage applied to each LED can be estimated by

$$V_f = \frac{V_{ave}}{N} \tag{3.24}$$

where V_f is the voltage drop across each LED and N is the total number of LED in the circuit. The forward voltage decrease can be shown in Fig. 3.16b. The decrease of forward voltage can be converted to forward current reduction with the V_f *vs.* I_f relationship. If the data in Ref. [37] is used, the current decreases by about 5% while the capacitance decreases by 12%. Since the current reduction is not significant with this data, it will not be considered when the performance of the power electronics is to be evaluated in the PoF model.

3.5. Life Time Prediction

3.5.1. Lifetime of LED

Since the lifetime of luminaire is governed by the lumen maintenance of LED, LED lifetime directly affects the failure of the luminaire (L70 lifetime). In order to estimate the LED lifetime, major LED manufactures adopted IESNA LM-80 which prescribes standard test methods for LED under controlled conditions to measure lumen maintenance of LED while controlling the junction temperature and ambient temperature in DC constant current mode [46].

The lifetime of LED in the luminaire is estimated based on data in Ref. [48]. The luminaire utilizes the polycarbonate lens and the ambient temperature inside the lens is 65℃. The L70 lifetime at 65℃ of ambient temperature is shown in Fig. 3.17.

It is to be noted that the L70 lifetime at the applied current of 500 mA was interpolated using the data at 350 and 700 mA.

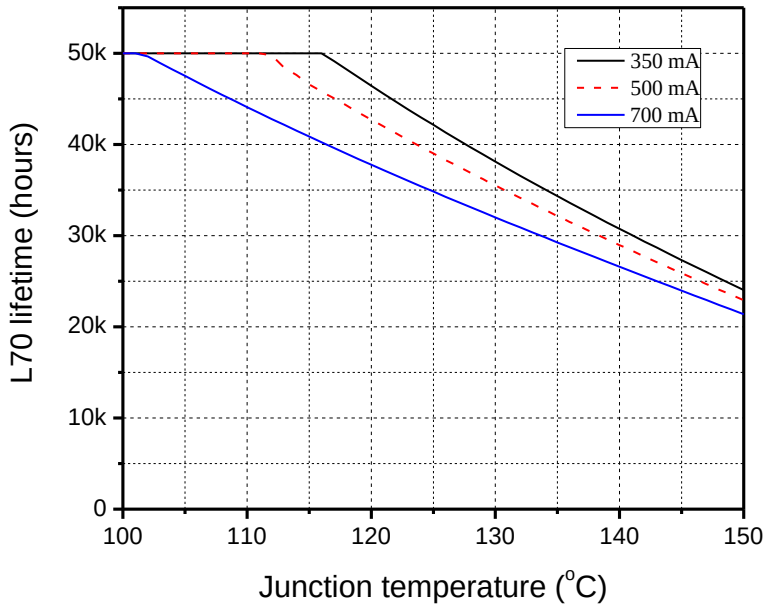

Figure 3.17 Mean L70 Lifetime at 65℃ of ambient temperature, operated at I_f =350mA and 700mA [48]

3.5.2. Computation of Luminaire Lifetime

All the information for the computation of lifetime has been obtained in the previous sections. The purpose of experiments and calculations was to predict the decay constant profile with time by using the junction temperature and forward current prediction data. The lumen maintenance then can be determined using the decay constant profile.

Figure 3.18 summarizes the procedure to compute the luminaire lifetime. The left track shows all the processes from the amplitude degradation of the synthetic jet

to the junction temperature. The amplitude degradation of the synthetic jet is first determined through the hybrid experiment/numerical model considering the compliant ring aging. The amplitude is converted to the air flow rate (Eq.(3.4)). Then the junction temperature is determined as a function of time using the empirical relationship between the enhancement factor and the junction temperature (Fig. 3.4b).

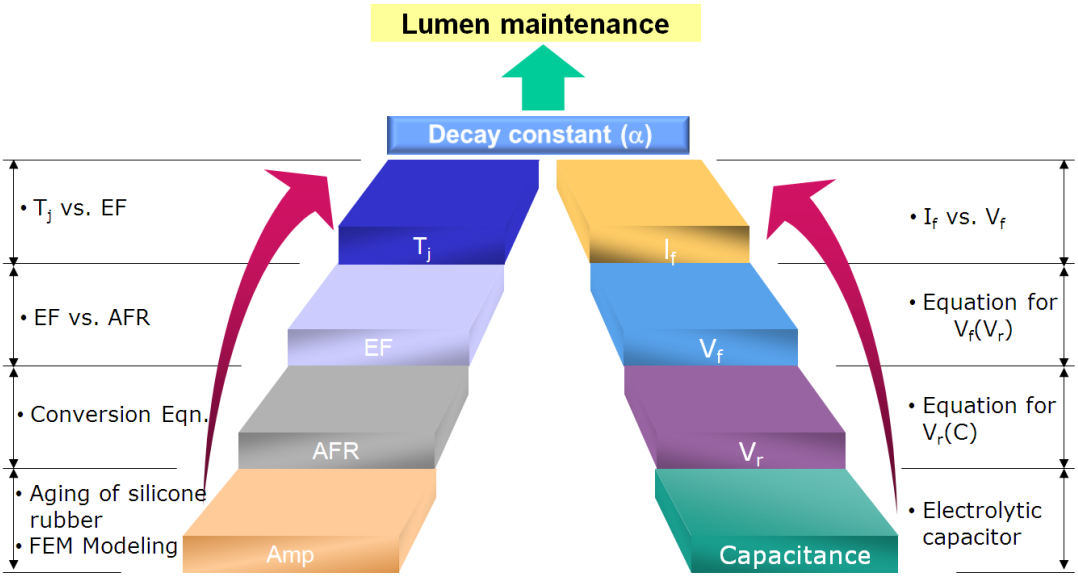

Figure 3.18 Computation procedure for luminaire lifetime

The right track deals with the issues associated with the driver electronics. The increase in the ripple voltage, caused by the capacitance degradation of the electrolytic capacitors in the LED driving circuit, is determined as a function of the operating time using the data in Ref. [48]. Then the reduction of the forward current is subsequently determined from the relationship between the forward current and forward voltage.

From Eq. (3.2), the decay constant for a given junction temperature and a forward current can be expressed as:

$$\alpha(T_j, I_f) = -\frac{1}{t_{L70}(T_j, I_f)} \ln 0.7 \tag{3.25}$$

where t_{L70} is the time at the lumen maintenance of 0.7.

The junction temperature will rise with time, which can be expressed in a general form as $T_j(t) = T_j^0 + K(t)$ where T_j^0 is the initial junction temperature and $K(t)$ is a function that defines the junction temperature increase as a function of time. The forward current will decrease with time, which can also be expressed as $I_f(t) = I_f^0 + I(t)$ where I_f^0 is the initial forward current and $I(t)$ is a function that defines the forward current decrease as a function of time.

As illustrated in Fig. 3.19, the lumen maintenance after each small time interval of Δt can be expressed as:

$$L_k = L_0 \exp\left[-\Delta t \sum_{i=1}^{k} \alpha(\tilde{T}_j^i, I_f^i) \right] \quad \text{for } k = 1, 2, 3... \tag{3.26}$$

where L_k is the lumen maintenance after the k^{th} time interval; $\tilde{T}_j^k$ is the averaged junction temperature over the k^{th} time interval; I_f^k is the averaged forward current over the k^{th} time interval; L_0 is the initial lumen output at time zero. It is worth noting that the function, $K(t)$, is directly related to the time-dependent performance degradation of the active cooling system (i.e., *EF* reduction). The function, $I(t)$, in

the computation is 0 due to the small amount of reduction of the current and thus I_f^k is constant (500mA). Then the lifetime criterion can be expressed as:

$$0.7L_0 \geq L_k \tag{3.27}$$

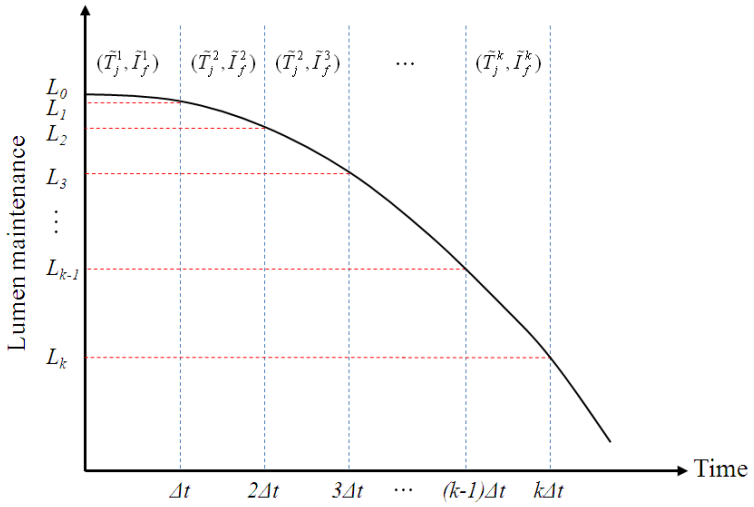

Figure 3.19 Illustration of lumen maintenance after each time interval

If Δt is set, the unknown "k" can be determined. In practice, the optical component degradation in the fixture as a function of temperature is ignorable. Then the final expected life at 70% lumen maintenance can be determined as

$$t_{life} = k\Delta t \tag{3.28}$$

The decay constant for each time interval can be computed by Eq. (3.25). The result is shown in Fig. 3.20. Then, the lumen maintenance is calculated by Eq. (3.26). Figure 3.21 shows the final result. Based on this calculation, the lumen maintenance is estimated to be 76% after 50,000 hours operation.

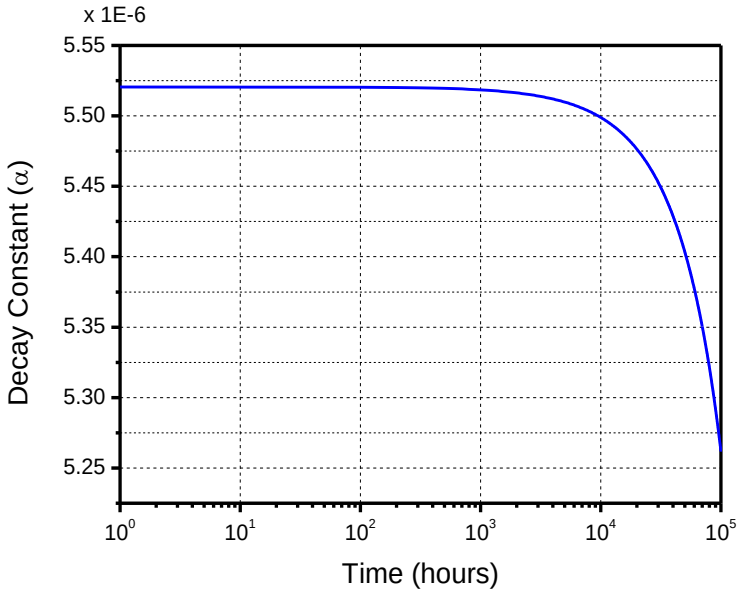

Figure 3.20 Decay constant vs. time

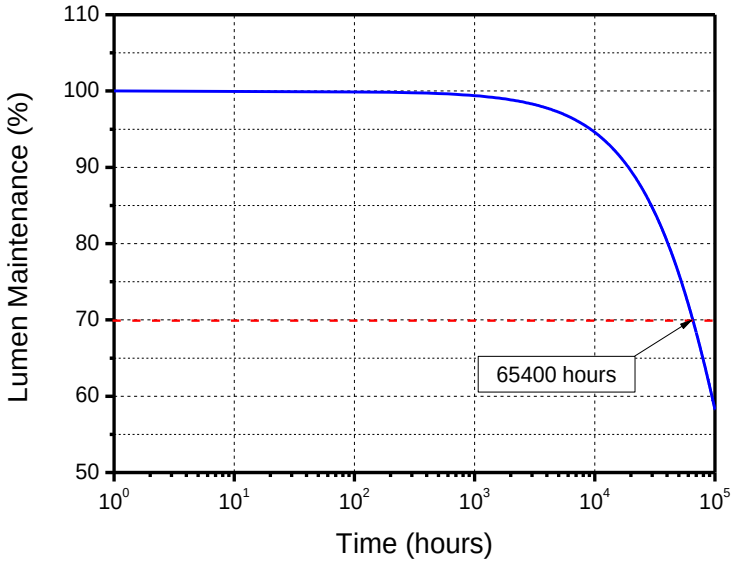

Figure 3.21 Lumen maintenance vs. time

3.6. Conclusion

A physics-of-failure based, hierarchical reliability model was implemented to determine the lifetime of an Edison base - 6 inch, compatible can, downlight - LED replacement bulb, cooled by synthetic jets. The degradation mechanisms of each of the main components (LED light engine, cooling system, and power electronics) were analyzed and their combined effect on luminaire reliability was calculated. The degradation rate of the synthetic jet was extremely low and the junction temperature rise over the intended life (50,000 hr) was negligible. For the power electronics, only time-dependent degradation of large electrolytic capacitors was considered and its effect on the ripple voltage increase was estimated using the existing data in the literature. Based on the proposed hierarchical model, the lumen maintenance was estimated to be 76% after 50,000 hours operation.

Chapter 4: SPD Deconvolution Scheme for Phosphor Converted White LED Using Multiple Gaussian Functions[4]

Abstract

We propose a novel procedure to deconvolute the spectral power distribution (SPD) of phosphor-converted LEDs (pc-LEDs). The procedure involves a two-step process using multiple Gaussian functions. The first step is a preliminary process to deconvolute an SPD using a pair of Gaussian functions. Using the results from the first step, the second step determines (1) the number of Gaussian functions to be used in the analysis and (2) the initial values and regression domains of the coefficients of each Gaussian function for subsequent multiple-regression operations. Successful deconvolution is confirmed by comparing the values of lumen, CCT and CRI with the experimental data of cool and warm pc-LEDs. The proposed approach is illustrated to evaluate the yellow to blue ratio and the phosphor power conversion efficiency.

[4] This chapter has been submitted for review to the *Applied Optics* under the title of "SPD Deconvolution Scheme for Phosphor Converted White LED Using Multiple Gaussian Functions" by B. Song and B. Han

4.1. Introduction

A phosphor converted light emitting diode (pc-LED) has a very unique profile of spectral power distribution (SPD) compared to the conventional incandescent light source which shows an evenly distributed spectrum over the wide range of visible light. The SPD of a pc-LED (white light: will be referred to as "SPD^W") is the combination of blue light from an LED chip (leaked blue light: will be referred to as "SPD^B") and yellow light from a phosphor layer (phosphor converted light: will be referred to as "SPD^P").

The optical parameters such as lumen, CCT, and CRI are functions of the power ratio between SPD^B and SPD^P. For example, the color of white light becomes cooler or warmer as the ratio of the leaked blue light increases or decreases. Consequently, the separate distributions of SPD^B and SPD^P are critically needed in order to enable the performance optimization of a pc-LED. The two separate SPD's are also required to analyze the performance of a pc-LED as a function of time since each SPD is altered by different degradation mechanisms. The reduction of leaked blue light is attributed to lens yellowing [29, 30], while the reduction of phosphor converted light is an apparent indication of phosphor layer degradation [24, 68].

An approach using the Gaussian function seems attractive to deconvolute SPD^B and SPD^P from SPD^W since it can describe the spectral distribution of light sources. The Gaussian function approach has been used in numerous LED-related applications such as the peak finding [69-71], the SPD design [72-75], the current and junction temperature dependent model of SPD [76, 77] and the LED radiation pattern simulation [78, 79].

The applications most relevant to deconvolution can be found in Ref. [72-75]. In Ref. [72, 74], an SPD simulation about a multichip LED was performed, where the SPD of each chip was described by a single Gaussian function. The SPD of a cool white pc-LED was described in Ref. [75], where SPD^B was represented by a single Gaussian function and an asymmetric Gaussian function was used to describe SPD^P considering its asymmetric nature. In Ref. [73], the Gaussian function was used to design the SPD of a UV LED and the mixture of blue, orange, yellow, and green phosphors, where each phosphor emission spectrum was represented by a single Gaussian function.

Neither SPD^B nor SPD^P has a symmetric distribution. In addition the SPD^P often shows an arbitrary shape when several phosphors are used (e.g., warm white pc-LED). Consequently the approaches to represent each spectrum by a single Gaussian function may not deconvolute the spectra most accurately. This paper presents a novel procedure to deconvolute the SPD of pc-LEDs. The procedure involves a two-step process using multiple Gaussian functions. The first step is a preliminary process to deconvolute an SPD using a pair of Gaussian functions (each one for the peaks of SPD^B and SPD^P, respectively), which is similar to the methods used in Ref. [75] . Using the results from the first step, the second step determines (1) the number of Gaussian functions to be used in the analysis and (2) the initial values and regression domains of the coefficients of each Gaussian function for subsequent multiple-regression operations. A detailed procedure is described in Section 4.2 and two implementations of the proposed procedure are presented in Section 4.3.

4.2. Two-Step Multiple Gaussian Function Method

The procedure for deconvolution is presented using a normalized SPD of a cool white pc-LED. The final goal is to determine the number of required Gaussian functions and the coefficients of each Gaussian function that best describes the original SPD. To achieve the goal, multiple regression operations are conducted in a two-step process.

4.2.1. Two-Step Process

STEP 1: Initial Pair of Gaussian Functions

This step is a preliminary process to deconvolute an SPD using a pair of Gaussian functions (each one for the peaks of SPD^B and SPD^P, respectively). The results are used for the next step that refines the deconvolution.

A cool white pc-LED was operated under a forward current of 350 mA. The SPD was measured while maintaining the junction temperature at 25 °C. The SPD normalized by the maximum value is shown in Fig. 4.1. The normalized SPD shows two maximum points (or peaks, P_1 and P_2) from SPD^B and SPD^P as well as a local minimum point (or valley, V) between the two peaks.

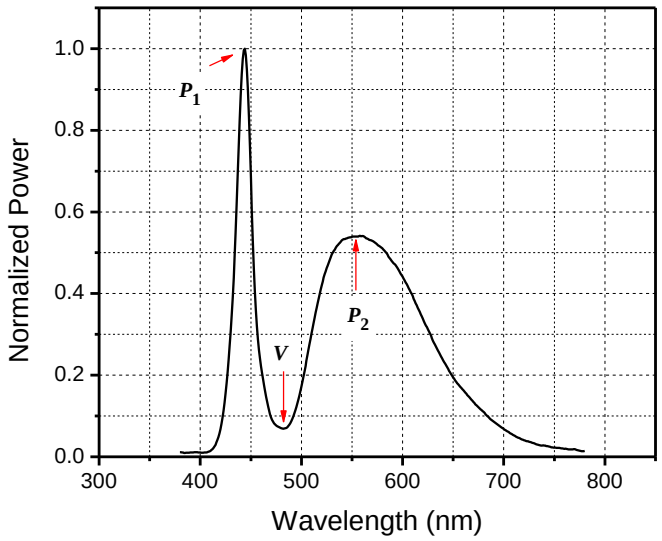

Figure 4.1 SPD of a cool white pc-LED normalized by its maximum value at P_1.

The initial regression begins with a pair of Gaussian functions, which are expressed as:

$$\sum_{i=1}^{2} G_i(\lambda) = \sum_{i=1}^{2} A_i \exp\left\{-\frac{(\lambda - B_i)^2}{C_i^2}\right\} \tag{4.1}$$

where A is the amplitude, B is the center wavelength and C is the width of the Gaussian function.

As mentioned earlier, neither SPD^B nor SPD^P has a symmetric distribution, and it is difficult to fit the SPD with only two Gaussian functions. The specific goal of the first step is to obtain a pair of Gaussian functions that offers the highest R^2 among those whose combined SPD match the wavelengths and amplitudes at the two peaks and the valley of the normalized SPD (P_1, P_2, and V in Fig. 4.1).

There are six unknowns in Eq. (4.1). The center wavelengths (B_1 and B_2) are fixed at the wavelengths of P_1 and P_2. Considering the fact that SPD^P has a wider

spectrum compared to SPD^B and thus it has a broader impact on the final spectrum, the amplitude of the second Gaussian function, A_2, is also fixed at the amplitude of P_2. Then the three remaining coefficients are determined using the following non-linear regression steps.

(1) Set an initial value of C_2 as well as its increment (ΔC_2).

(2) Determine A_1 by using the following relationship:

$$SPD^W(B_1) = A_1 + G_2(B_1) \tag{4.2}$$

(3) The remaining coefficient is C_1 and it can be determined as

$$C_1 = \frac{\left|\lambda_V - B_1\right|}{\sqrt{-\ln\left(\frac{SPD^W(\lambda_V) - G_2(\lambda_V)}{A_1}\right)}} \tag{4.3}$$

where λ_V is the wavelength at the valley, V.

(4) Determine the R^2 value using the following definition.

$$R^2 = 1 - \frac{S_{err}}{S_{tot}} \tag{4.4}$$

where $S_{tot} = \sum_{\lambda=\lambda_i}^{\lambda_f} \left\{ SPD^W(\lambda) - \overline{SPD^W}(\lambda) \right\}$ and $S_{err} = \sum_{\lambda=\lambda_i}^{\lambda_f} \left\{ SPD^W(\lambda) - G_1(\lambda) - G_2(\lambda) \right\}$

; $\overline{SPD^W}(\lambda) = \frac{1}{\lambda_f - \lambda_i + 1} \sum_{\lambda=\lambda_i}^{\lambda_f} SPD^W(\lambda)$, λ_i and λ_f are initial and final wavelengths of SPD^W, respectively.

(5) Repeat (2) to (4) while Eq. (4.3) is valid; i.e., $0 < SPD^W(\lambda_V) - G_2(\lambda_V) < A_1$.

Figure 4.2a shows the result of R^2 as a function of C_2. The SPD obtained using the value of C_2 at the maximum R^2 is shown in Fig. 4.2b. The SPD regenerated

by the pair of Gaussian functions (2G) produces exactly the same values at the three points as expected.

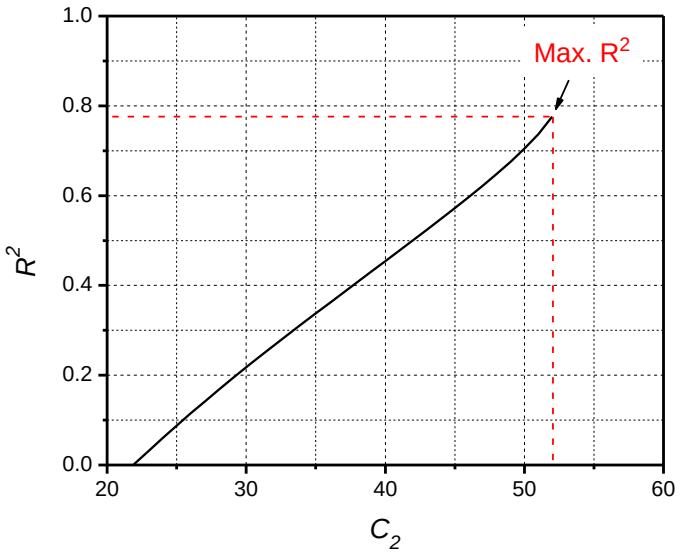

(a)

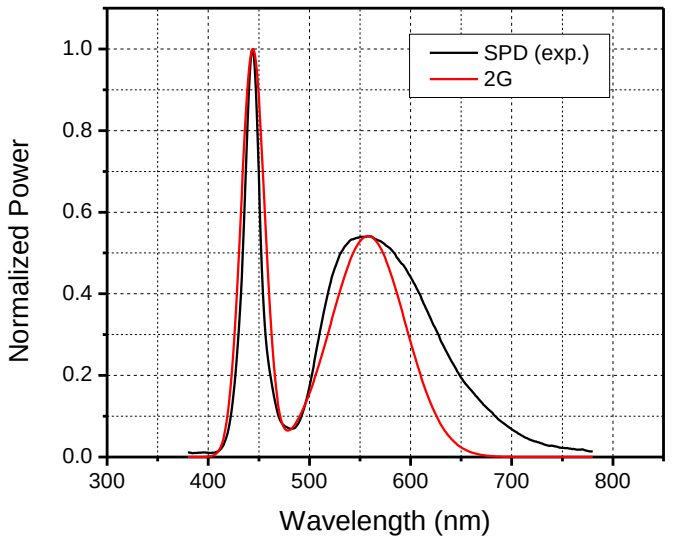

(b)

Figure 4.2 (a) R^2 vs. C_2 ; and (b) SPD obtained using the value of C_2 at the maximum R^2

STEP 2: Multiple Gaussian Functions for Refinement

In Step 2, the number of Gaussian functions required for deconvolution is first determined using the result obtained from Step 1. The result of Step 1 is subtracted from the experimental data. The resultant plot is shown in Fig. 4.3a. Then, the number (N_G) of Gaussian functions is determined from the number of local maxima and minima in the plot. For the current SPD, the total number of Gaussian functions is $N_G = 6$.

It is important to note that the first three Gaussian functions corresponding to three points below λ_V form SPD^B, and the rest forms SPD^P (Fig. 4.3b). A mathematical representation of SPD^W using the multiple Gaussian functions is:

$$SPD^W(\lambda) = SPD^B(\lambda) + SPD^P(\lambda) = \sum_{i=1}^{3} a_i \exp\left\{-\frac{(\lambda - b_i)^2}{c_i^2}\right\} + \sum_{i=4}^{N_G} a_i \exp\left\{-\frac{(\lambda - b_i)^2}{c_i^2}\right\} \quad (4.5)$$

There are a total of 18 unknown coefficients (= 3 times N_G) in Eq. (4.5). They are determined through multiple-regression operations. The objective function of the multiple-regression operation is the same as R^2 in the objective function defined by Eq. (4.4). The initial value of each coefficient for the regression is also defined using the result from Step 1, which is critically required to ensure the optimum convergence of the objective function.

The initial values of a_i's are given as the amplitude of P_i (A_{pi}) and the values of a_i's are decreased gradually during the regression. The initial values of b_i's are given as the wavelengths of P_i (λ_{pi}) and their regression domains are defined using the wavelengths of two adjacent points; for example, the initial value of b_2 is the wavelength of P_2 (or A_{p2}) and its regression domain is defined as

$\frac{\lambda_{p_1} + \lambda_{p_2}}{2} \le b_2 \le \frac{\lambda_{p2} + \lambda_{p_3}}{2}$. It is worth noting that the ranges of b_i's are critical since the center wavelength of each Gaussian function should not overlap during regression. Finally, the initial values of c_i's are given by the values of C_1 and C_2 obtained from Step 1; more specifically C_1 for $c_{1\sim3}$ and C_2 for $c_{4\sim6}$. This is valid as each set forms SPD^B and SPD^P, respectively.

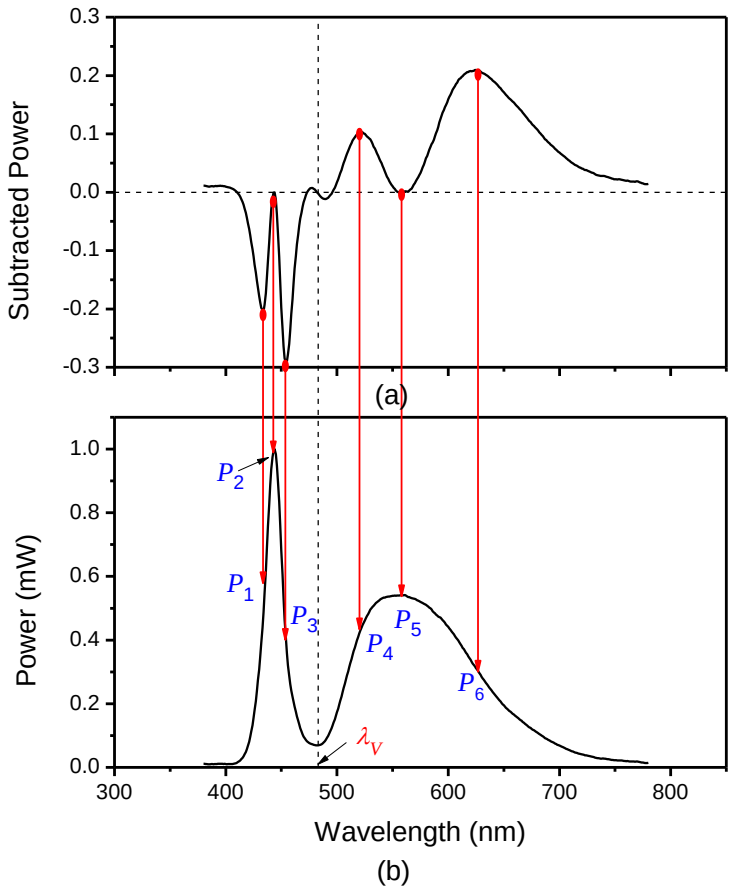

Figure 4.3 (a) Plot obtained by subtracting the SPD obtained from Step 1 from the experimental data; and (b) the points corresponding to the maxima and minima of (a).

The final regression result is shown in Fig. 4.4, where it is compared with the experimental data. Perfect agreement is evident; the R^2 value is nearly "1". The result can be presented more quantitatively using the optical parameters such as Lumen, CCT, CRI and color coordinates. Table 4.1 shows the comparison. The proposed deconvolution procedure produces an SPD virtually identical to the experimental data.

The 6 Gaussian functions used in the analysis are shown in Fig. 4.5a. As mentioned earlier, the sum of the first three Gaussian functions represents SPD^B and the rest of them form SPD^P. The two deconvoluted spectra are shown in Fig. 4.5b.

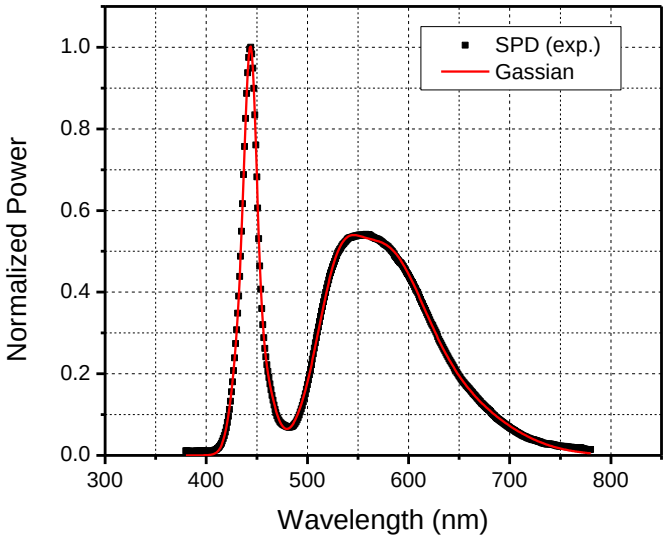

Figure 4.4 Results obtained from the multiple Gaussian function approach is compared with the experimental data

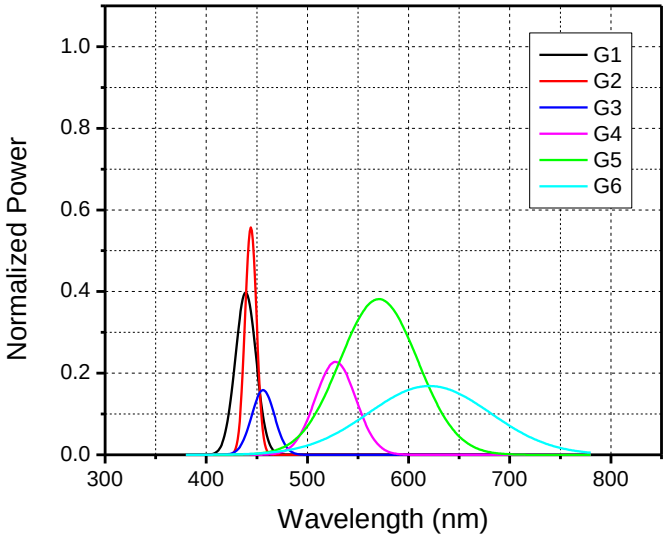

(a)

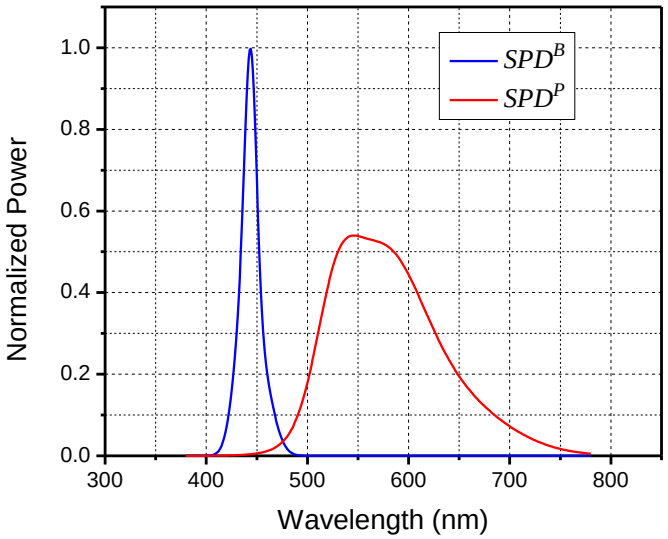

(b)

Figure 4.5 (a) Gaussian functions used for deconvolution; and (b) SPDs of the deconvoluted leaked blue light and phosphor converted light

Table 4.1 Comparison between the experimental data and the results of multiple Gaussian function approach in terms of optical parameters

	Experiment	Multiple Gaussian
Lumen	32.0	32.0
CCT (K)	5237	5238
CRI	68.2	68.2
CIEx	0.3393	0.3393
CIEy	0.3565	0.3565
CIEz	0.3041	0.3043

4.2.2. Deconvolution of Warm White pc-LED

The SPD of a warm white pc-LED was deconvoluted by the proposed scheme to confirm its validity. The result of Step 1 is shown in Fig. 4.6. The result after subtraction is shown in Fig. 4.7. The total number of local maxima and minima are N_G = 7. Consequently, multiple-regression operations were conducted with 7 Gaussian functions for the warm white pc-LED.

The regression result is shown in Fig. 4.8a, where perfect agreement is also evident. The 7 Gaussian functions used in the analysis are shown in Fig. 4.8b. Again, the sum of the first three Gaussian functions represents SPD^B and the rest of them form SPD^P. The two deconvoluted spectra are shown in Fig. 4.8c. Successful deconvolution is achieved in spite of the unsymmetrical nature of SPD^P.

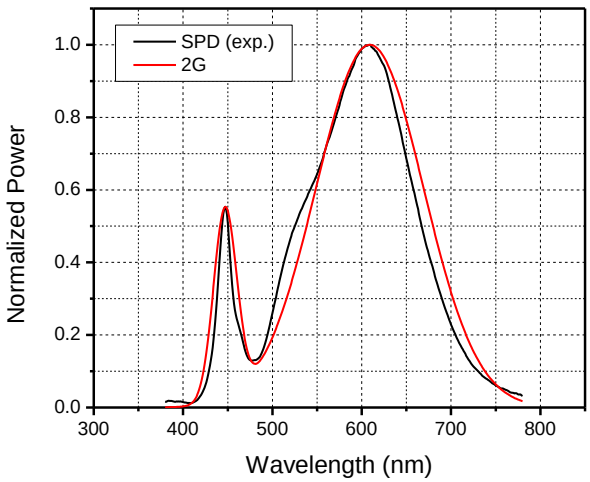

Figure 4.6 Step 1 result of warm white pc-LED

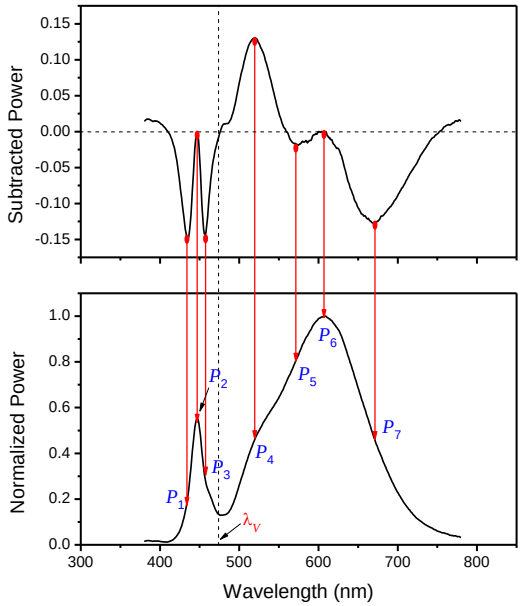

Figure 4.7 Experimental data subtracted by fitting function (warm white SPD)

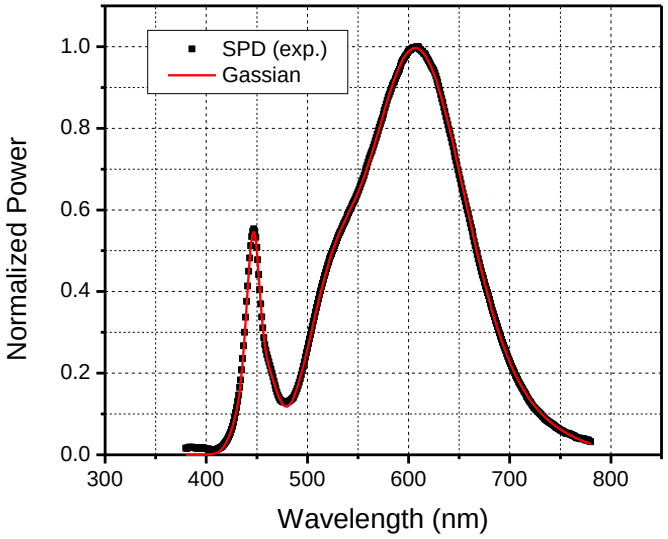
SPD (exp.)
Gassian
Normalized Power
Wavelength (nm)
1.0
0.8
0.6
0.4
0.2
0.0
300
400
500
600
700
800

(a)

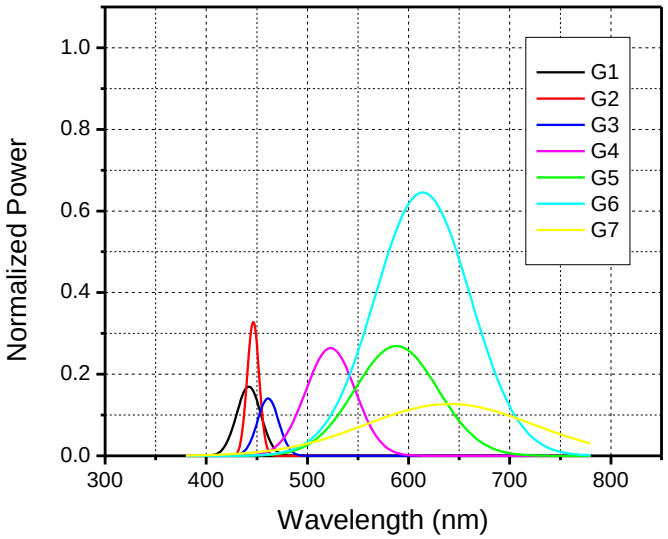
G1
G2
G3
G4
G5
G6
G7
Normalized Power
Wavelength (nm)
1.0
0.8
0.6
0.4
0.2
0.0
300
400
500
600
700
800

(b)

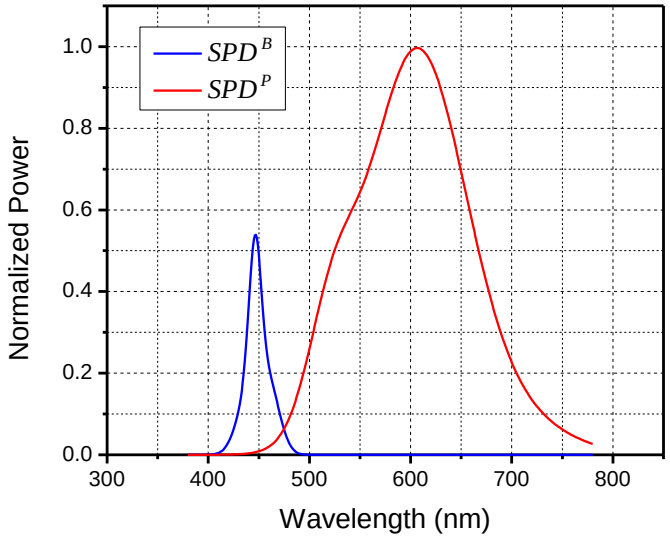

(c)

Figure 4.8 Results obtained from a warm white pc-LED: (a) the multiple Gaussian function approach is compared with the experimental data; (b) Gaussian functions used for deconvolution; and (c) SPDs of the deconvoluted leaked blue light and phosphor converted light

4.3. Implementation

The proposed scheme was implemented for (1) SPD design using YBR (yellow to blue ratio) and (2) calculation of phosphor power conversion efficiency. Warm and cool white pc-LEDs were tested at various forward current levels (100 ~1000 mA with an interval of 150 mA) while maintaining the junction temperature at 25 ℃. The SPDs of warm and cool white pc-LEDs are shown in Fig. 4.9(a) and (b), respectively.

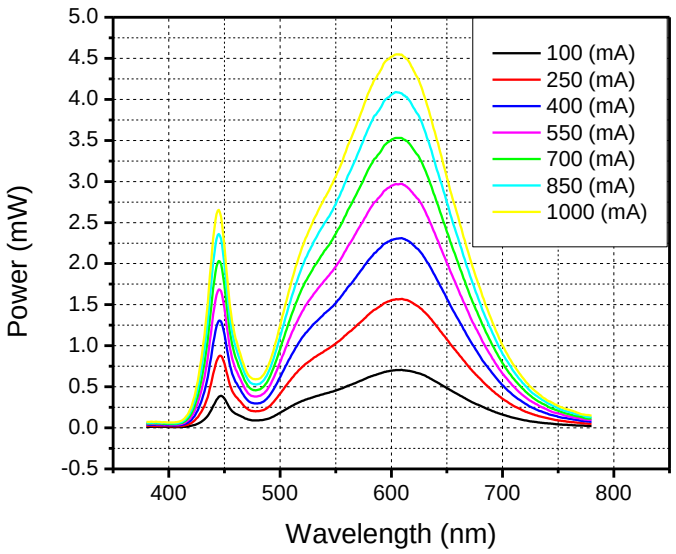

(a)

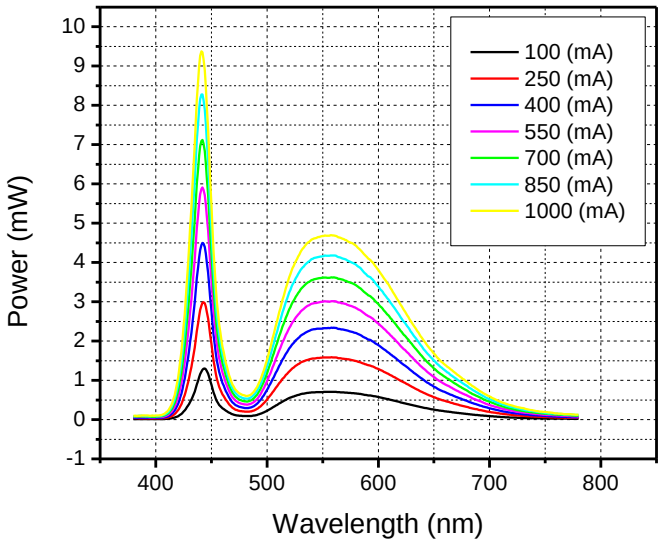

(b)

Figure 4.9 SPDs of (a) warm and (b) cool white pc-LEDs under various forward currents; T_j = 25 ℃ for all cases.

4.3.1. Yellow to Blue Ratio (YBR)

The yellow to blue ratio (YBR) is defined as

$$\text{YBR} = \frac{\int SPD^{P}(\lambda)d\lambda}{\int SPD^{B}(\lambda)d\lambda} = \frac{\sum_{i=4}^{N_G} a_i \exp\left\{-\frac{(\lambda - b_i)^2}{c_i^2}\right\}}{\sum_{i=1}^{3} a_i \exp\left\{-\frac{(\lambda - b_i)^2}{c_i^2}\right\}} \tag{4.6}$$

Since its value changes with phosphor configurations (e.g., thickness, concentration ratio, etc.) for a given LED package, the YBR was used extensively to analyze the phosphor performance in LED packages [80, 81] and chromatic degradation in degraded LED packages [22-24, 49].

Using the proposed scheme, the YBR can be calculated accurately. The SPDs in Fig. 4.9 were deconvoluted, and the YBRs were calculated using Eq. (4.6). The results are shown in Fig. 4.10a. As expected, the YBR of the warm white LED is higher than that of the cool white LED. As can be seen from the normalized YBR plot in Fig. 4.10b, however, the current dependence of YBR is nearly identical.

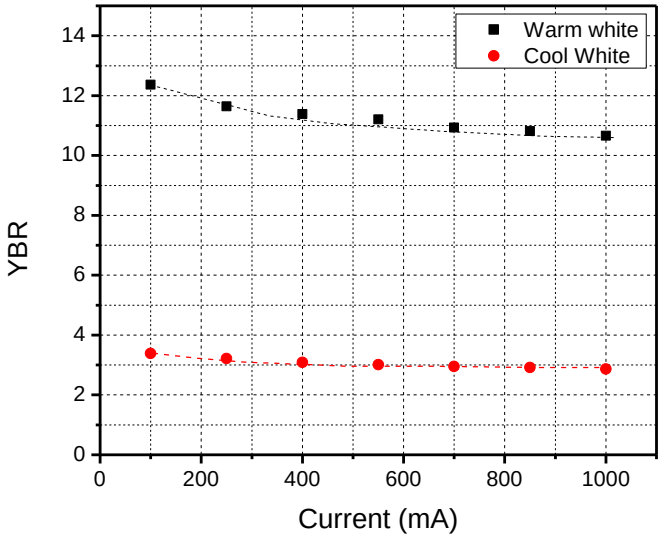

(a)

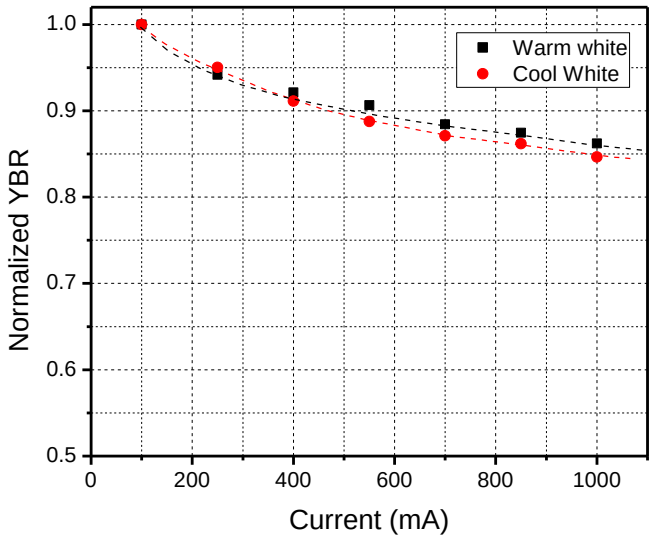

(b)

Figure 4.10 YBRs of warm and cool white pc-LEDs: (a) absolute; and (b) normalized

It is important to note that the shapes of SPD^B and SPD^P (i.e., their normalized distributions) remain the same even when the YBR is altered by changing the

phosphor concentration ratio. This concept can be used to estimate the ranges of CCT and CRI that the given SPD^B and SPD^P can produce.

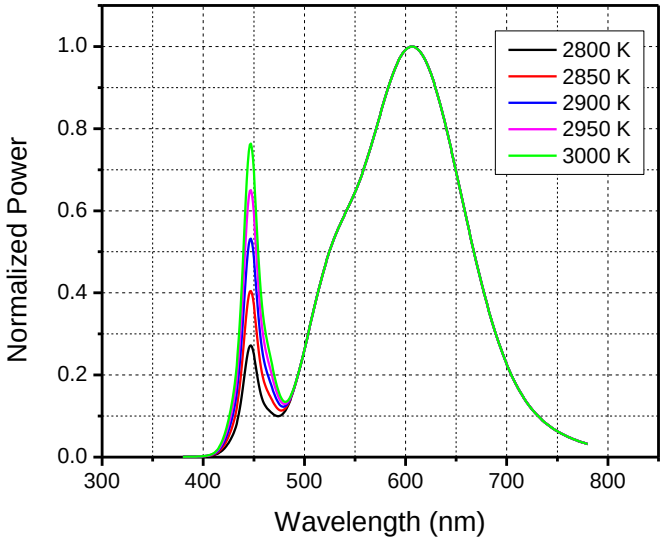

(a)

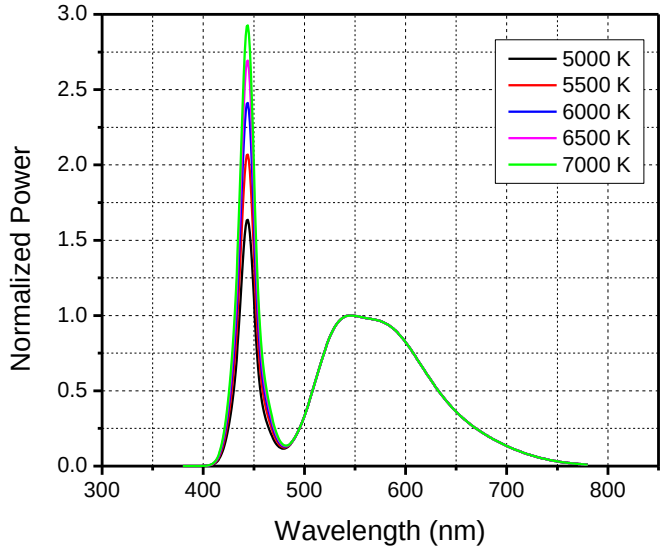

(b)

Figure 4.11 SPDs with various YBRs: (a) warm white; and (b) cool white

In Fig. 4.11, the normalized warm and cool white SPDs with various YBRs are shown. Each plot represents a CCT value within the range of typical warm white (from 2700 K to 3000 K) [82] and cool white (> 5000K). The plots were produced using the two deconvoluted SPDs while adjusting the YB ratios until a CCT value matches to a desired one.

The relationship among YBR, CCT, CRI is shown in Fig. 4.12. Both CCT and CRI decrease as YBR increases. For a given phosphor and LED package configuration, the available color options can be readily obtained from this approach. It is worth noting that lumen may have to be compromised for a better color option. The complete prediction about lumen, CCT and CRI can be done if a relationship with the YBR and the phosphor concentration can be determined experimentally.

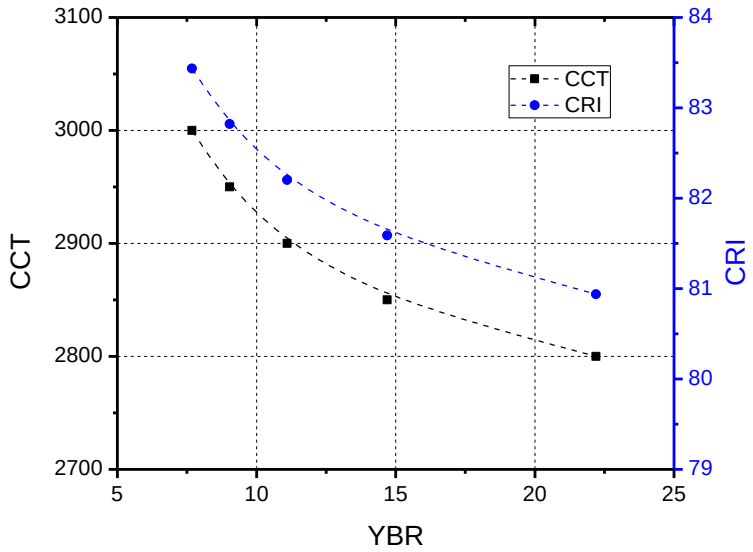

(a)

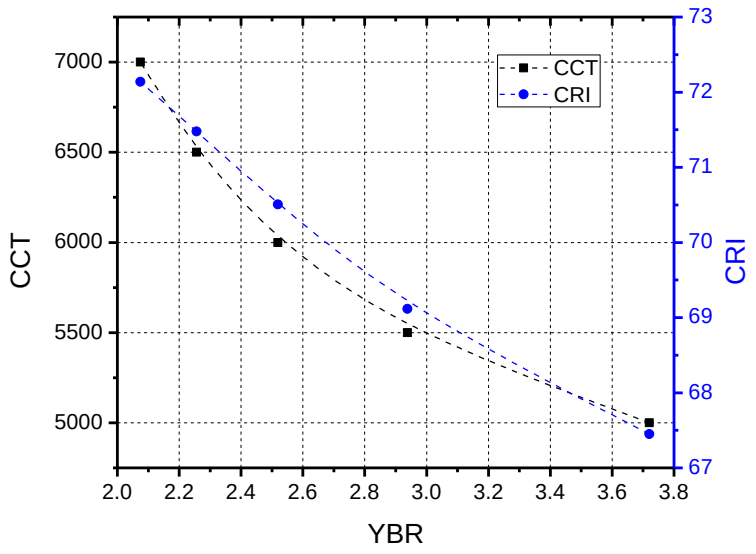

(b)

Figure 4.12 CCT and CRI variation with YBRs: (a) warm white; and (b) cool white

4.3.2. Phosphor Power Conversion Efficiency

The phosphor power conversion efficiency is defined as the ratio of the radiant flux of phosphor converted light to the total amount of radiant flux of blue light used in phosphor conversion. Mathematically, it can be expressed as

$$\eta_p = \frac{\int SPD^P(\lambda)d\lambda}{\int\left\{SPD^B_{total}(\lambda) - SPD^B\right\}d\lambda} = \frac{\sum_{i=4}^{N_g} a_i \exp\left\{-\frac{(\lambda - b_i)^2}{c_i^2}\right\}}{\int SPD^B_{total}(\lambda)d\lambda - \sum_{i=1}^{3} a_i \exp\left\{-\frac{(\lambda - b_i)^2}{c_i^2}\right\}} \quad (4.7)$$

where η_p is the phosphor power conversion efficiency and SPD^B_{total} is the total amount of blue light generated by a package without phosphor. The phosphor power conversion efficiency is an effective property dictated by various package parameters

including the package type, the number of phosphors used in the package, the phosphor concentration ratio, and the phosphor location in the LED package [83-90]. It can be employed to characterize the performance of multiple phosphors in LED packages.

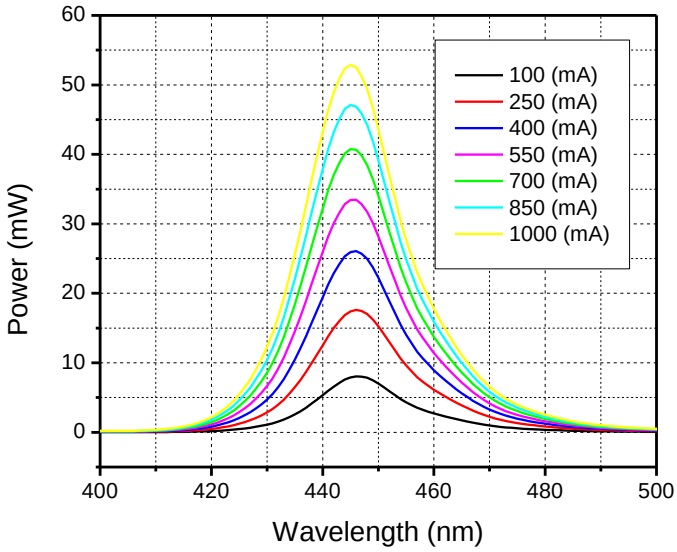

Figure 4.13 SPDs of blue LED under various forward currents; T_j = 25 ℃ for all cases.

The blue LED package was tested at the same conditions used to produce the SPDs in Fig. 4.9. The results of SPD_{total}^{B} are shown Fig. 4.13. Then, the phosphor power conversion efficiency can be calculated from the two deconvoluted SPDs using Eq. (4.7). The results are shown in Fig. 4.14a. The warm white LED shows lower phosphor power conversion efficiency than the cool white LED. The normalized plot in Fig. 4.14b shows that the phosphor conversion efficiency decreases linearly with the forward current and the reduction rate is larger in the warm white LED. The

lower conversion efficiency and the higher forward current dependency may be attributed to multiple phosphors used in the warm white LED.

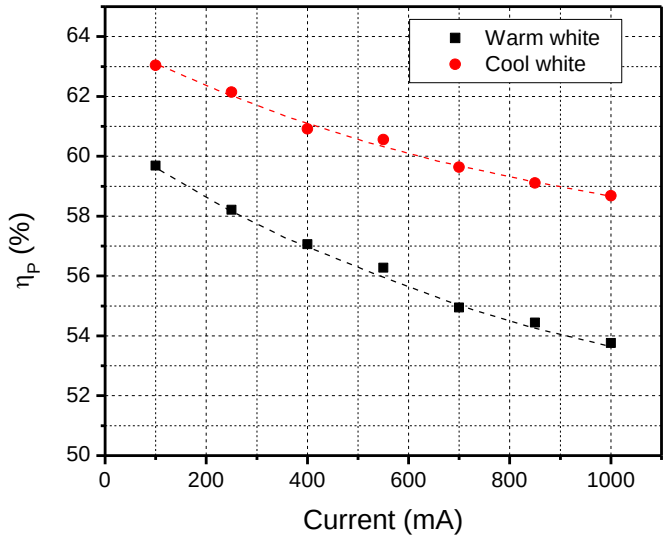

(a)

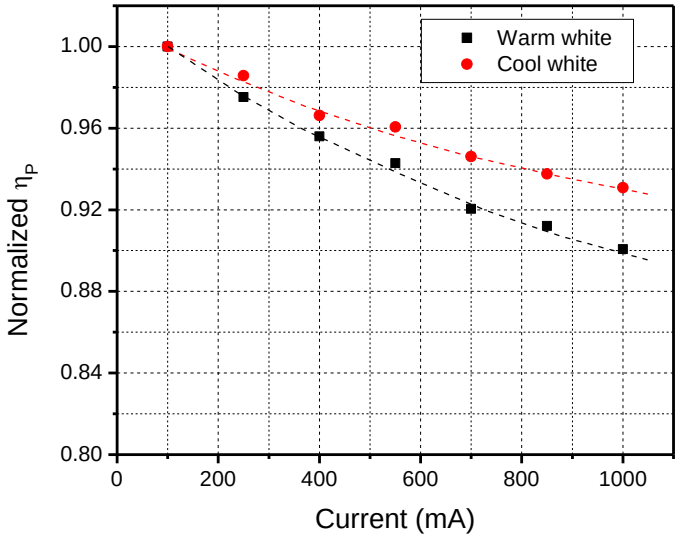

(b)

Figure 4.14 (a) Phosphor power conversion efficiency under various forward currents; and (b) the efficiency normalized by its maximum value at I_f = 100 mA.

4.4. Conclusion

A regression scheme using multiple Gaussian functions was proposed to deconvolute the SPDs of pc-LEDs. The scheme deconvoluted cool and warm white pc-LEDS into the leaked blue light and phosphor converted light. The results confirmed that the proposed scheme was effective and accurate. The scheme was implemented for calculations of YBR and phosphor power conversion efficiency. The scheme is very versatile and can be employed in various SPD analyses such as simulation of emission spectra of multiple phosphors, LED package degradation analysis, etc.

Chapter 5: Quantitative Analysis of Phosphor-Converted LED Degradation Using Spectral Power Distribution[5]

Abstract

Lumen depreciation and color quality change of phosphor-converted LED (pc-LED) are caused by the combination of various degradation mechanisms including chip, phosphor layer and packaging material degradations. We present a mathematical and experimental procedure to quantify the effect of each mechanism on pc-LED degradation. A mathematical model based on the spectral power distribution (SPD) is proposed after defining each degradation parameter. The model decomposes effectively the SPD change caused by the degradation into the contributions of individual degradation mechanisms. The model is implemented using the SPDs of a pc-LED with a conformally coated phosphor, obtained before and after 9,000 hours of operation. The analysis quantifies the effect of each degradation mechanism on the final values of lumen , CCT and CRI.

[5] This chapter has been submitted for review to the *IEEE Transactions on Device and Materials Reliability* under the title of "Quantitative Analysis of Phosphor-Converted LED Degradation Using Spectral Power Distribution" by B. Song and B. Han

5.1. Introduction

Phosphor converted LEDs (pc-LEDs) have been accepted as a general light source, which will eventually substitute the incandescent and fluorescent lights as the performance of pc-LEDs is improved continuously. It has been claimed that the luminous efficacy of 254 lm/W can be achieved under normal operating conditions [1]. This revolutionary transition is imminent as demands for green energy (no hazardous materials such as lead and mercury) and reduction of energy consumption continuously increase.

Reliability of pc-LEDs has been studied by numerous researchers since LED-based solid state lighting (SSL) was realized for residential and commercial applications. In Refs. [2-8], reliability of LEDs was assessed by simply monitoring light output. An empirical model was developed assuming the exponential decay of light output [3] and used for the lifetime prediction [9, 10]. The reliability was also assessed using both optical and electrical characteristics [8, 11-20]. An increase in the forward voltage was observed in degraded LEDs [12, 17, 20]. The degradation of phosphor was reported in Refs. [7, 21-24]. The degradation of phosphor was indicated by reduction in the phosphor converted light power [21-23]. The effect of packaging material degradation was reported in Refs. [24-32]. The dominant degradation phenomenon was silicone or epoxy lens yellowing.

In a typical pc-LED package (Fig. 5.1), a blue LED chip is mounted on a highly conductive substrate and a phosphor layer is coated conformally on top of the chip. Either reflective (Fig. 5.1a) or diffusive surface (Fig. 5.1b) around the chip

enhances light output extraction. Silicone-based materials encapsulate the chip-phosphor subassemblies to form a final package.

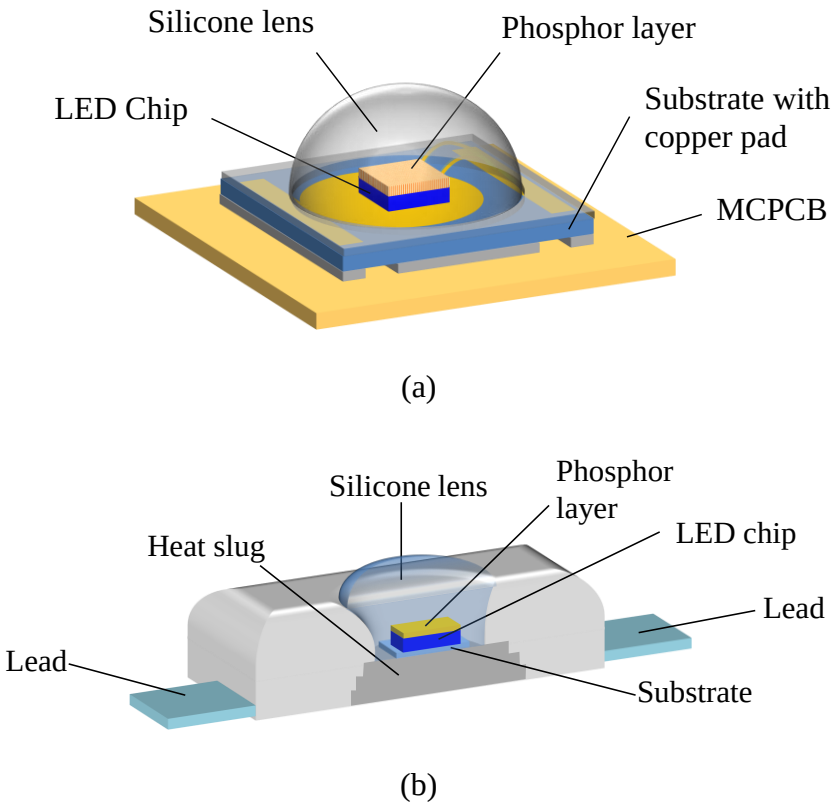

Figure 5.1 Typical pc-LED packages; (a) Package type 1 and (b) Package type 2

The degradation of pc-LEDs decreases lumen maintenance. ASSIST suggested a failure criterion as 30% reduction of initial lumen (Fig. 5.2); the lumen reduction of 30% can be a threshold for detecting gradual reduction of light output [91]. Another but more specific test condition is provided by Department of Energy in US [92], which suggests the lumen maintenance of 91.8% after 6000 hours of operation (Fig. 5.2) as a failure criterion; this is based on the test condition in LM80-

08 [46]. When an LED does not satisfy the criteria, i.e., it cannot sustain the lumen output for the required lifetime, the LED has to be improved until the criteria are met.

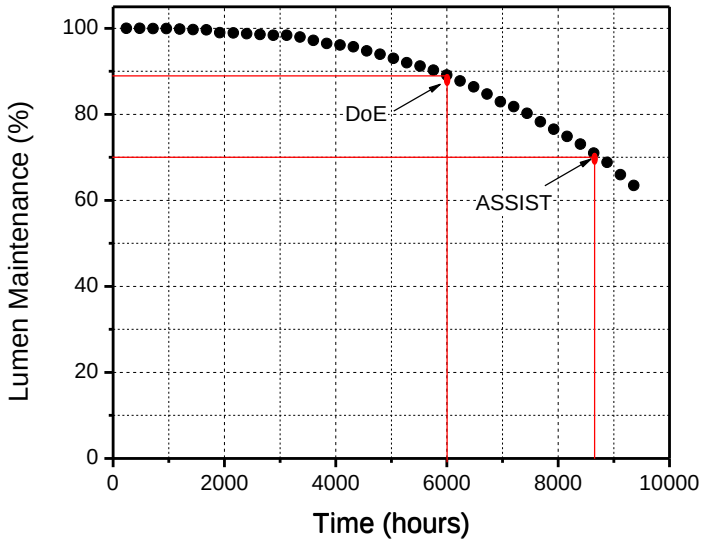

Figure 5.2 Illustration of lumen maintenance

The lumen depreciation, illustrated in Fig. 5.2, can be caused by a combination of various degradation mechanisms; i.e., degradation mechanisms can contribute at different rates to cause the same lumen reduction. The following example further illustrates the relationship between the lumen depreciation and the degradation mechanisms.

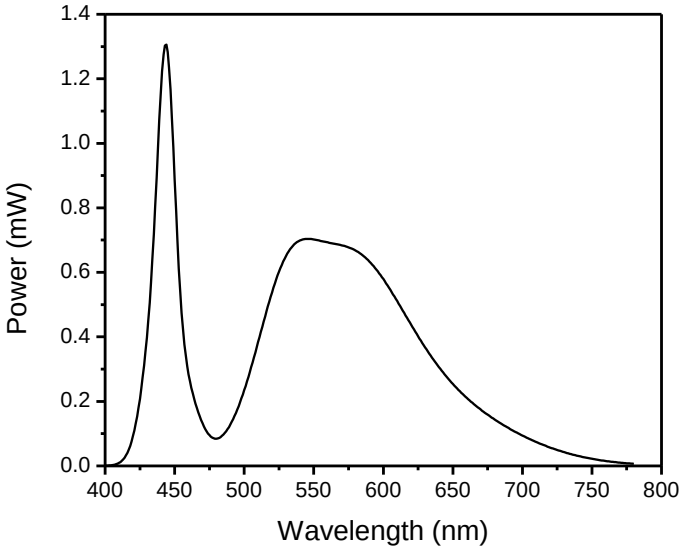

(a)

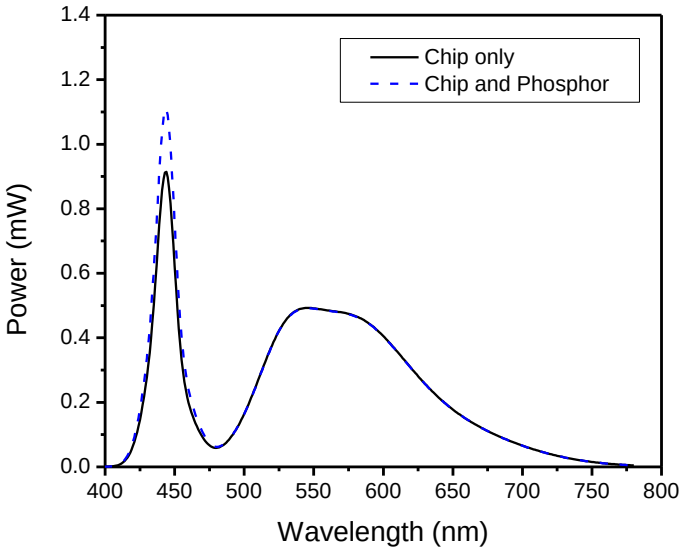

(b)

Figure 5.3 (a) SPD of a cool white pc-LED; and (b) two simulated SPDs that show the identical lumen reduction of 30%.

Let us consider the SPD of a cool white pc-LED (Fig. 5.3a), which has a luminous flux of 41.6 lm. Two different SPDs that show the same lumen reduction of 30% (a luminous flux of 29.1 lm) but are produced by different degradation mechanisms are shown in Fig. 5.3b. The solid line (black) represents the case of chip degradation only (internal quantum efficiency reduction) [93-97]; it was obtained by decreasing the SPD proportionally by 30% over the whole spectrum. The dashed line (blue) represents the case where both chip and phosphor layer degraded; it was obtained by a chip degradation amount of 20% and some additional reduction of the phosphor power conversion efficiency [83-85, 87, 89, 90, 98]. The two SPDs are very similar, especially in the yellow spectrum; and thus, it is difficult to quantify the contribution of each degradation mechanism.

As discussed earlier, the degradation of pc-LEDs has been studied extensively. To the best of authors' knowledge, however, it has not been possible to separate the effect of various degradation mechanisms from the SPDs of pc-LEDs degraded under normal operating conditions, which is critically required to improve the design of pc-LEDs for optimum reliability. The objective of this paper is, thus, to propose and implement a mathematical and experimental procedure to quantify the effect of each degradation mechanism on the final LED degradation. The goal is achieved by analyzing the SPDs of new and aged pc-LEDs in such a way that the SPD change after operation is decomposed into the contributions of individual degradation mechanisms.

Three major degradation mechanisms are described in Section 5.2. The corresponding degradation parameters are defined in Section 5.3. Section 5.4 is

devoted to an implementation using the SPDs of a pc-LED with a conformally coated phosphor, obtained before and after 9,000 hours of operation. Some experimental evidence about the package degradation is also discussed in Section 5.5.

5.2. Degradation Mechanisms

A pc-LED has a unique spectral power distribution (SPD). Some of blue light is converted through a phosphor layer and the rest escapes. Accordingly, the SPD is comprised of two parts: the leaked blue light and the phosphor converted light. Various regression schemes using multiple Gaussian functions can be found in the literature, which enable deconvolution of the SPD into the two parts. The SPD, then, can be expressed as:

$$\Phi_w(\lambda) = \Phi_{leak}(\lambda) + \Phi_{conv}(\lambda) \tag{5.1}$$

where $\Phi_w(\lambda), \Phi_{leak}(\lambda)$ and $\Phi_{conv}(\lambda)$ are the SPDs of the white light LED, the leaked blue light, and the phosphor converted light, respectively.

The pc-LEDs degrade through various mechanisms during normal operations, mainly by chip degradation, phosphor layer degradation and packaging material degradation. The SPD can be expressed more generally as:

$$\Phi_w(\lambda, t) = \Phi_{leak}(\lambda, t) + \Phi_{conv}(\lambda, t) \tag{5.2}$$

where $\Phi_W(\lambda, t)$, $\Phi_{leak}(\lambda, t)$, and $\Phi_{conv}(\lambda, t)$ are the SPDs of white light, leaked blue light, and phosphor converted light, respectively, at time = *t*.

The three degradation mechanisms are explained schematically in Fig. 5.4. The chip degradation is the radiant flux reduction of an LED chip, which is attributed to degradation mechanisms such as defect generation [95, 99], dislocation movement [93, 94], dopant diffusion [96, 97, 100], etc. Nonradiative recombination in the quantum well increases, which results in reduction in the light output.

If the blue LED chip degrades at a rate of $\eta_c(t)$, both leaked blue light and phosphor converted light are reduced at the same rate; i.e.,

$$\begin{aligned} \Phi_{leak}(\lambda,t) &= \eta_c(t)\Phi_{leak}(\lambda,0) \\ \Phi_{conv}(\lambda,t) &= \eta_c(t)\Phi_{conv}(\lambda,0) \end{aligned} \tag{5.3}$$

Various phosphors are used in pc-LEDs. When phosphors are exposed to a high humidity condition, the migration of phosphors increases through the moisture path [21, 101]. Phosphor converted light can be also reduced by the carbonization of phosphor layers [22, 102]. If the phosphor layer degrades at a rate of $\varepsilon_p(t)$, only phosphor converted light is reduced by the rate while the leaked blue light remains unchanged; i.e.,

$$\Phi_{conv}(\lambda,t) = \eta_c(t)\varepsilon_p(t)\Phi_{conv}(\lambda,0) \tag{5.4}$$

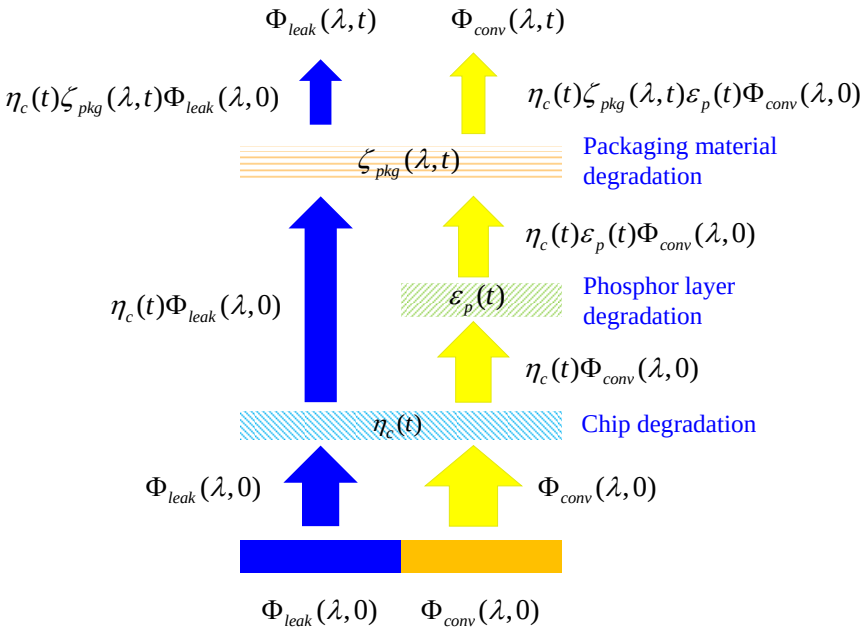

Figure 5.4 Schematic illustration of three degradation mechanisms

The encapsulation materials are incorporated to enhance the extraction efficiency. The silicone or epoxy is frequently used as the encapsulation material. The transmittance of the encapsulation materials is reduced when it is exposed to UV light or high temperature conditions [24, 26, 27, 29-32, 68, 103-105]. The packaging material degradation controls the transmittance reduction rate. Then, the packaging material degradation spectrum, $\zeta_{pkg}(\lambda,t)$, can be defined as:

$$\zeta_{pkg}(\lambda,t)=\frac{T(\lambda,t)}{T(\lambda,0)} \tag{5.5}$$

where $T(\lambda,t)$ and $T(\lambda,0)$ are the "effective" transmittance of packaging materials before and after degradation. Then, two deconvoluted SPDs finally become:

$$\begin{aligned}\Phi_{leak}(\lambda,t)&=\eta_c(t)\zeta_{pkg}(\lambda,t)\Phi_{leak}(\lambda,0)\\ \Phi_{conv}(\lambda,t)&=\eta_c(t)\zeta_{pkg}(\lambda,t)\varepsilon_p(t)\Phi_{conv}(\lambda,0)\end{aligned} \tag{5.6}$$

From Eq. (5.6), the SPD of an aged pc-LED (or at time = t) can be expressed as:

$$\begin{aligned}\Phi_W(\lambda,t) &= \Phi_{leak}(\lambda,t) + \Phi_{conv}(\lambda,t) \\ &= \eta_c(t)\zeta_{pkg}(\lambda,t)\left\{\Phi_{leak}(\lambda,0) + \varepsilon_p(t)\Phi_{conv}(\lambda,0)\right\}\end{aligned} \tag{5.7}$$

5.3. Definition of Degradation Parameters

The detailed descriptions of three degradation parameters are provided and their effects on the final SPD are illustrated using a cool white LED.

5.3.1. Chip Degradation Rate, $\eta_c(t)$

The chip degradation rate is the blue chip radiant flux ratio of new chip to aged chip, which can be expressed as:

$$\eta_c(t) = \frac{\int_{\lambda_1}^{\lambda_2} \Phi_B(\lambda,t)d\lambda}{\int_{\lambda_1}^{\lambda_2} \Phi_B(\lambda,0)d\lambda} \tag{5.8}$$

where $\Phi_B(\lambda,0)$ and $\Phi_B(\lambda,t)$ are the SPDs of new and aged bare blue chips (i.e., without any packaging materials including the phosphor layer and the silicone lens).

If the LED chip is degraded, the whole SPD will decrease proportionally (Fig. 5.5); i.e., the shape of the SPD (the SPD normalized by the maximum power) remains the same. Consequently, the luminous flux (lumen) decreases but the correlated color temperature (CCT) and color rendering index (CRI) hardly change as they are affected only by the shape of the SPD.

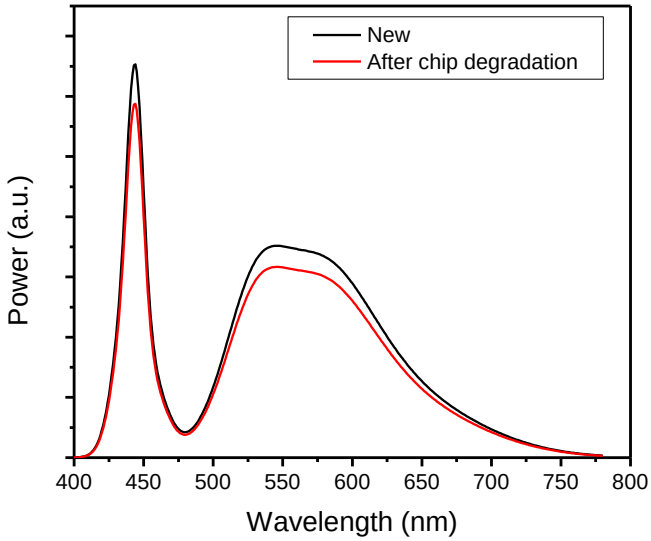

Figure 5.5 Illustration of chip degradation

5.3.2. Phosphor Layer Degradation Rate, $\varepsilon_p(t)$

The phosphor layer degradation is illustrated in Fig. 5.6, where the phosphor power conversion efficiency is reduced. This reduction decreases the luminous flux significantly (in the example, the lumen is reduced by approximately 20%). In addition, the relative power of the blue light is stronger (i.e., the color of light becomes more bluish), and thus the CCT increases.

The analysis of phosphor layer degradation is based on the fact that the phosphor degradation reduces the power of phosphor converted light while preserving the spectral shape of the phosphor converted light. Mathematically,

$$\overline{\Phi}_{conv}(\lambda,0) = \overline{\Phi}_{conv}(\lambda,t) \tag{5.9}$$

where $\overline{\Phi}_{conv}(\lambda,0)$ and $\overline{\Phi}_{conv}(\lambda,t)$ are the SPDs of the phosphor converted light normalized by their peak amplitudes ($\Phi_{conv}^{\max}(\lambda,0)$ and $\Phi_{conv}^{\max}(\lambda,t)$).

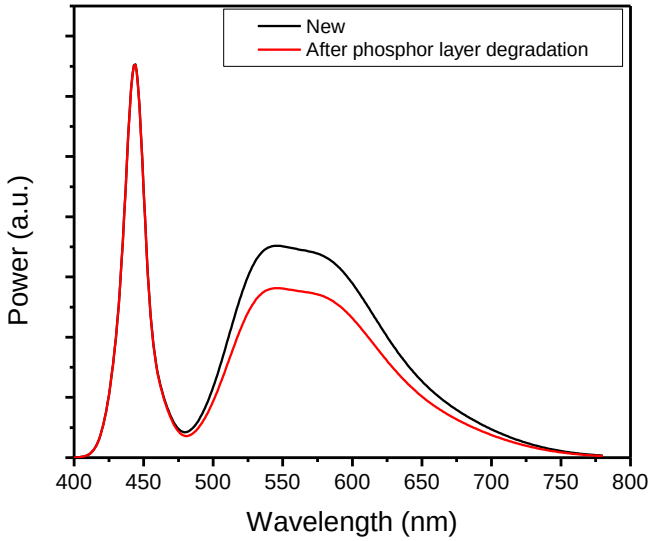

Figure 5.6 Illustration of phosphor layer degradation

It is important to note that the packaging material degradation can also alter $\Phi_{conv}(\lambda,t)$; i.e., Eq. (5.9) is valid only for the spectrum that is not affected by the packaging material degradation. Considering the well-known fact that the transmittance that is affected by the packaging material degradation is reduced typically only at low blue wavelengths [29, 31], the critical wavelength, λ_c, beyond which the packaging material degradation does not affect the $\Phi_{conv}(\lambda,t)$ can be determined from the following relationship:

$$f(\lambda) \equiv \frac{\overline{\Phi}_{conv}(\lambda,0)}{\overline{\Phi}_{conv}(\lambda,t)} = 1 \quad \text{if} \quad \lambda \geq \lambda_c \tag{5.10}$$

This is illustrated in Fig. 5.7, where the normalized SPDs of the phosphor converted light are shown in (a) and the value of $f(\lambda)$ is shown in (b). The critical wavelength is determined as the smallest wavelength that satisfies $f(\lambda)=1$.

Considering the critical wavelength, the phosphor layer degradation rate can be defined as:

$$\varepsilon_p(t)=\frac{\Phi_{conv}(\lambda,t)}{\eta_c(t)\Phi_{conv}(\lambda,0)} \quad \text{for any } \lambda \geq \lambda_c \tag{5.11}$$

It is worth noting that the phosphor converted light, $\Phi_{conv}(\lambda,t)$, contains the effect of the chip degradation. In Eq. (5.11), it is divided by the chip degradation factor, $\eta_c(t)$, to compensate the effect.

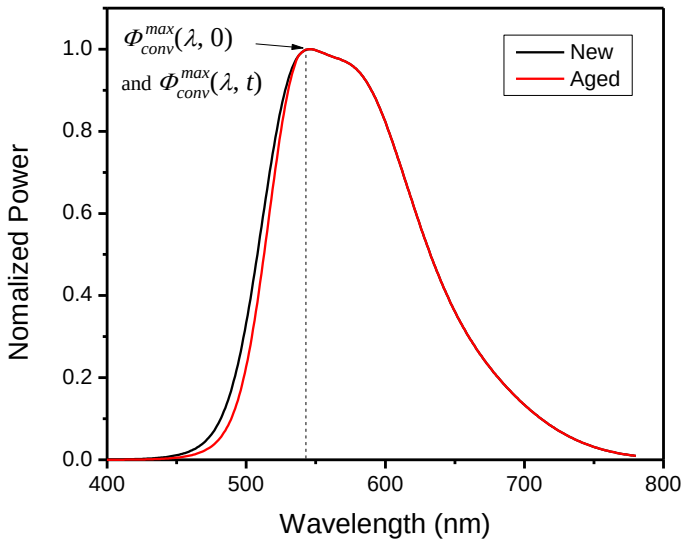

(a)

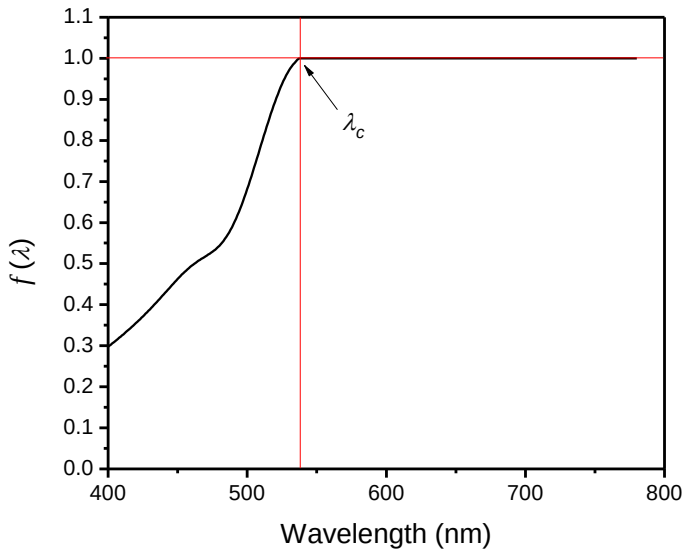

(b)

Figure 5.7 (a) SPDs normalized by the maximum power of the phosphor converted light; and (b) determination of the critical wavelength from the ratio between the normalized SPDs

5.3.3. Packaging Material Degradation Spectrum, $\zeta_{pkg}(\lambda,t)$

Considering again the critical wavelength, the packaging material degradation spectrum can be determined from Eq. (5.7) as

$$\begin{aligned} &\text{For } \lambda < \lambda_c \ , \quad \zeta_{pkg}(\lambda,t) = \frac{\Phi_W(\lambda,t)}{\eta_c(t)\left\{\Phi_{leak}(\lambda,0) + \varepsilon_p(t)\Phi_{conv}(\lambda,0)\right\}} \\ &\text{For } \lambda \geq \lambda_c \ , \quad \zeta_{pkg}(\lambda,t) = 1 \end{aligned} \tag{5.12}$$

The effect of the packaging material degradation on the SPD is illustrated in Fig. 5.8, where a typical packaging material degradation spectrum is assumed for illustration. The power of the leaked blue light decreases but the converted light is affected only slightly. This has an insignificant effect on the luminous flux (less than

3%). However, this does reduce the relative power of the leaked blue light with respect to the phosphor converted light (i.e., the color of light becomes more yellowish), and thus decreases the CCT.

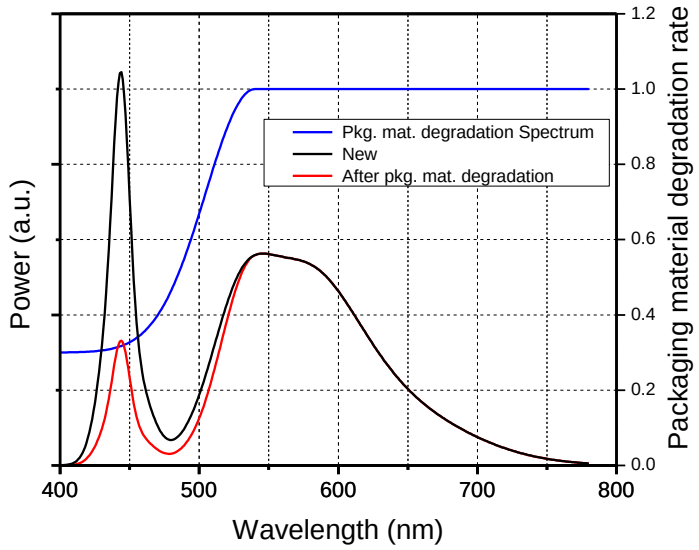

Figure 5.8 Illustration of packaging material degradation

5.4. Implementation

The proposed scheme is implemented for a warm white LED. The SPDs obtained before (new) and after operations (aged) are presented after the testing condition is described. The three degradation parameters are obtained from the SPDs. An analysis is followed to quantify the effect of each parameter on the optical parameters.

5.4.1. Test Condition and SPDs

A set of warm white LEDs whose configuration is similar to Fig. 5.1a was tested. They were operated at the forward current of 500 mA while maintaining the junction temperature at 100 ℃. The SPDs obtained before and after 9,000 hours of operation are shown in Fig. 5.9. The SPDs were measured by a 40" integrating sphere (LM40: Sphere Optics) and the junction temperature was controlled by a thermoelectric cooler installed inside the integrating sphere.

The initial lumen at 500mA was 94.3 lm. After 9,000 hours, the lumen maintenance decreased by 15.4%. The CCT and CRI were also changed from 3103 K to 2800 K (ΔCCT = –303 K) and from 83.1 to 79.2 (ΔCRI = –3.9), respectively.

The SPDs have to be deconvoluted to obtain the phosphor layer degradation rate and the packaging material degradation spectrum (Eqs. (5.11) and (5.12)). An effective regression scheme using multiple Gaussian functions was employed to deconvolute the SPDs [106]. The procedure involves a two-step process using multiple Gaussian functions. Briefly, the first step is a preliminary process to deconvolute an SPD using a pair of Gaussian functions (each one for the peaks of the leaked blue light and phosphor converted light, respectively). Using the results from the first step, the second step determines (1) the number of Gaussian functions to be used in the analysis and (2) the initial values and regression domains of the coefficients of each Gaussian function for subsequent multiple-regression operations. Then, the SPD can be expressed using Gaussian functions as:

$$\Phi_W(\lambda) = \Phi_{leak}(\lambda) + \Phi_{conv}(\lambda) = \sum_{i=1}^{3} a_i \exp\left\{-\frac{(\lambda - b_i)^2}{c_i^2}\right\} + \sum_{i=4}^{N_G} a_i \exp\left\{-\frac{(\lambda - b_i)^2}{c_i^2}\right\} \quad (5.13)$$

where a is the amplitude, b is the center wavelength, c is the width of the Gaussian function, and N_G is the number of total Gaussian functions used. A more detailed procedure can be found in [106].

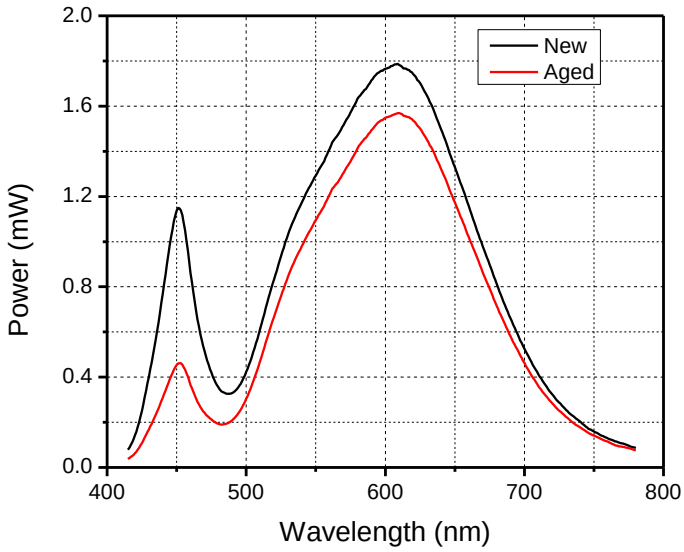

Figure 5.9 SPDs of LEDs before (new) and after (aged) 9,000 hours

The results of multiple-regression operations are shown in Fig. 5.10 (a) and (b) for the SPDs of the new and aged LEDs, respectively. Perfect agreement in the white light spectra is evident. The regression accuracy was confirmed further by comparing the optical parameters. Table 5.1 shows the comparisons. Besides the regression coefficient of nearly unity ($R^2 \approx 1$), the spectra provide virtually identical values of optical parameters. It should be noted that the values of optical parameters, especially CCT and CRI, can differ substantially even when the regression coefficient is very high.

The sum of the first three Gaussian functions represents the SPD of the leaked blue light and the rest of them form the SPD of the phosphor converted light [106]. The deconvoluted spectra are shown in Fig. 5.11.

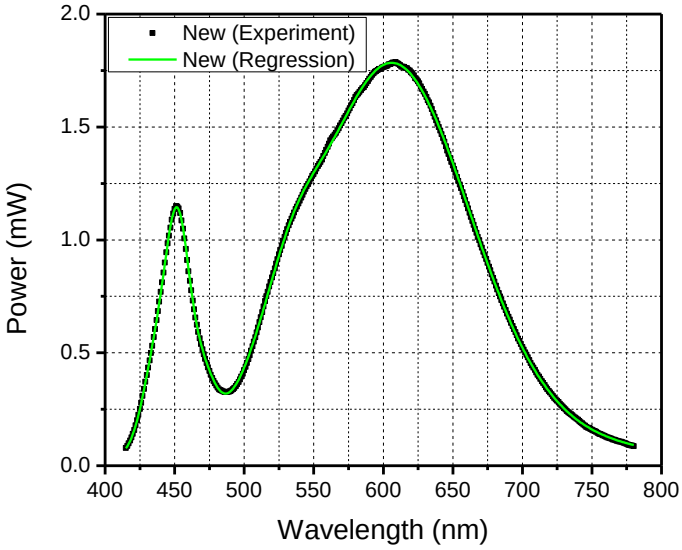

(a)

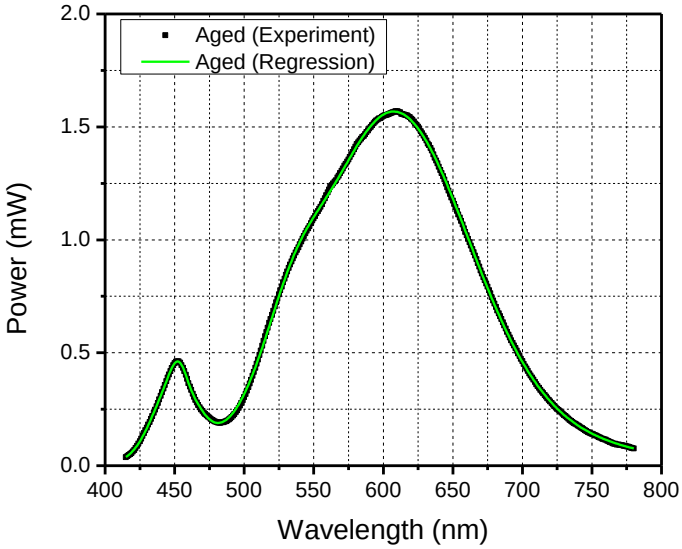

(b)

Figure 5.10 SPDs obtained from multiple-regression operations are compared with the experimental data for (a) the new LED as well as (b) the aged LED

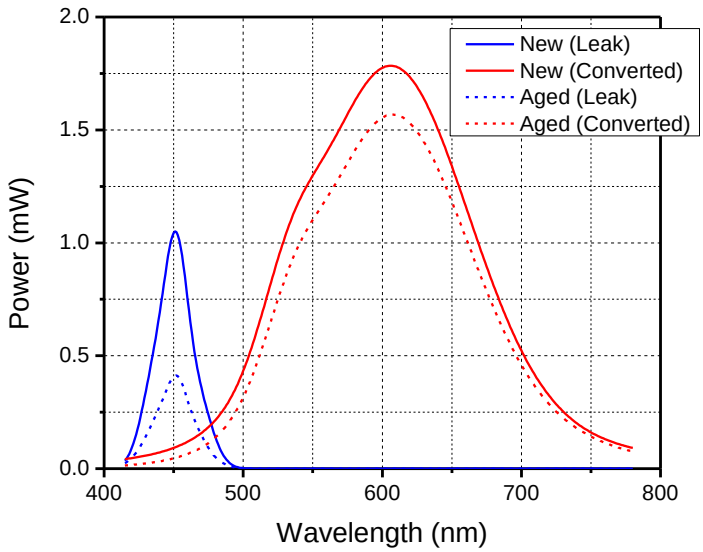

Figure 5.11 Deconvoluted SPDs of the new and aged LEDs

Table 5.1. Comparison of SPDs between experiment and multiple Gaussian functions

	New LED		Aged LED	
	Experiment	Regression	Experiment	Regression
Lumen	94.3	94.3	79.9	79.9
CCT (K)	3103	3103	2800	2803
CRI	83.1	83.1	79.2	79.2

5.4.2. Determination of Degradation Parameters

Chip Degradation Rate

To obtain the chip degradation rate, a set of new and aged LED packages were decapsulated by a decapsulation solution (PolyGone 505: RPM Technology). Figure 5.12 shows the SPDs of new and aged bare blue chips measured after the silicone lens

and the phosphor layer were removed. The chip degradation rate, $\eta_c(t)$, can be calculated using Eq. (5.8); it is 97%. The chip degraded only by 3% after 9,000 hours.

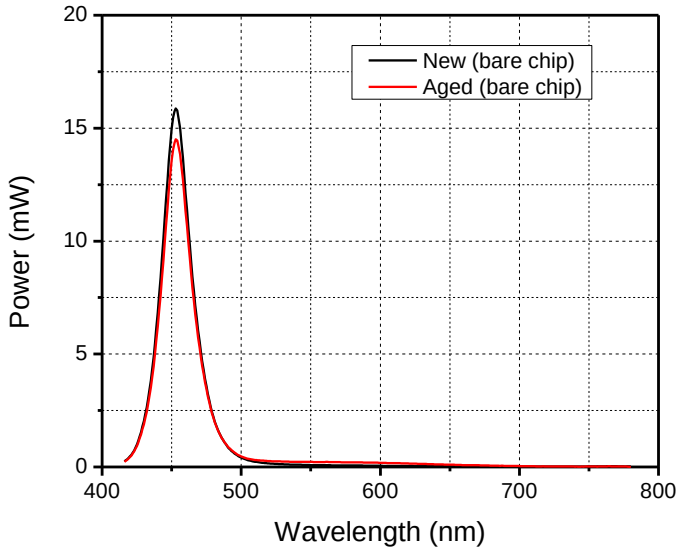

Figure 5.12 SPDs of bare chip LEDs before (new) and after operation (aged)

Phosphor Layer Degradation Rate

The critical wavelength must be determined first to calculate the phosphor layer degradation rate. The SPDs of phosphor converted light in Fig. 5.11 are normalized first by each maximum power (Fig. 5.13a). Then, the normalized phosphor converted light SPD of the aged LED is divided by that of the new LED (Fig. 5.13b). The critical wavelength is then determined in Fig. 5.13b; it is approximately 606 nm. The phosphor layer degradation rate can be calculated from Eq. (5.11) at any wavelength longer than the critical wavelength. The phosphor layer degradation rate was determined to be 90%.

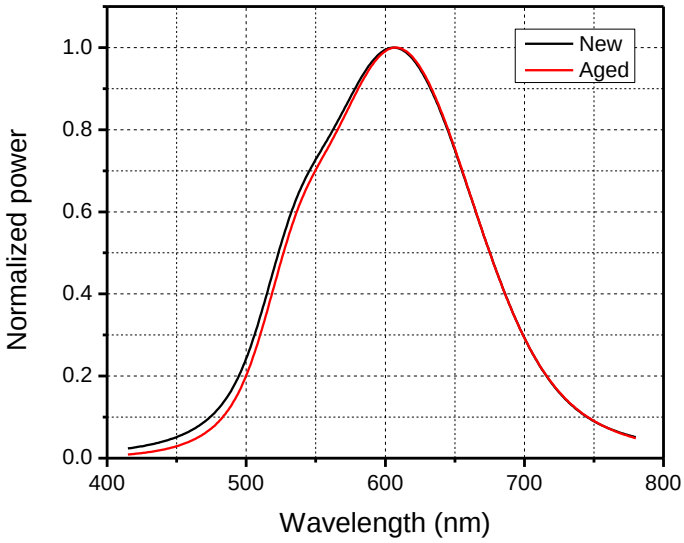

(a)

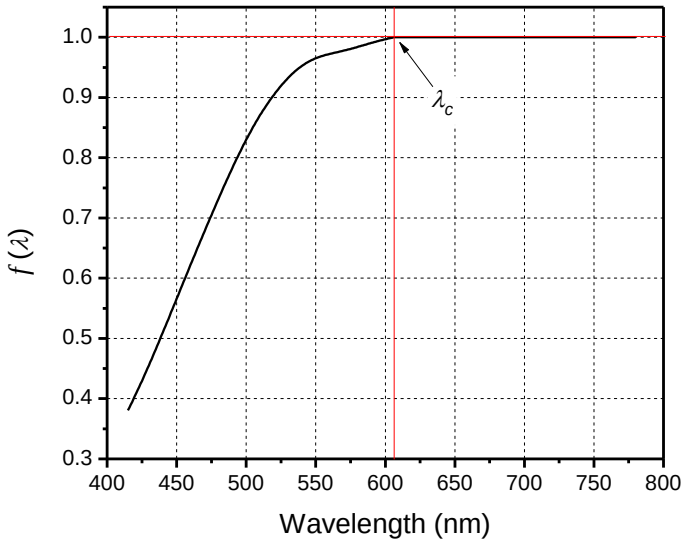

(b)

Figure 5.13 (a) Phosphor converted light SPDs normalized by each maximum value; and (b) the critical wavelength is determined from the ratio between the normalized SPDs.

Packaging Material Degradation Spectrum

The deconvoluted SPDs in Fig. 5.11 were utilized again to obtain packaging material degradation spectrum from Eq.(5.12). The result is shown in Fig. 5.14. The packaging material degradation results in significant reduction over the blue wavelength range.

It is worth noting that the packaging material degradation spectrum decreases as the wavelength decreases but it increases slightly below 450 nm. More importantly, the packaging material degradation spectrum becomes as low as 0.4, which is much smaller than the reported transmittance reduction after yellowing [29].

For the LED tested in the study, the phosphor layer was conformably coated over the chip, and thus the packaging material degradation spectrum was affected not only by the transmittance reduction of the silicone lens but also by the degradation of the encapsulation material that formed the phosphor layer. A possible reason for the large transmission reduction will be discussed later.

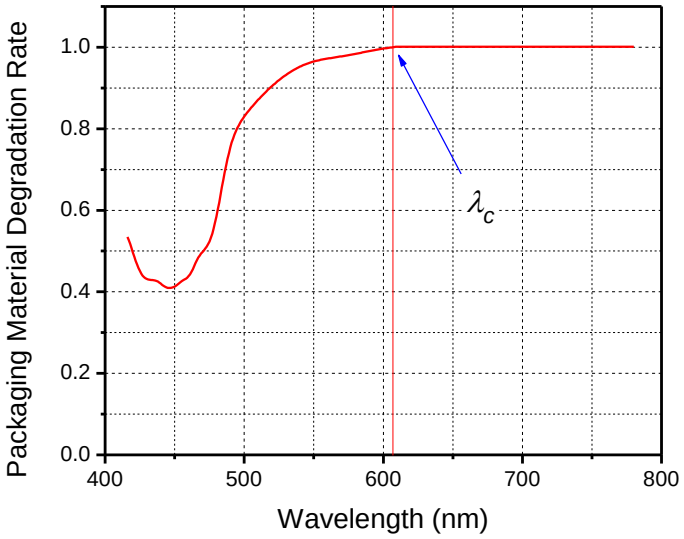

Figure 5.14 Packaging material degradation spectrum

5.4.3. Effect of Degradation Parameters on Optical Parameters

The effect of each degradation parameter on the optical parameters was analyzed. Using the values obtained from the previous section, the SPDs of the LED were first calculated from the deconvoluted spectra considering (1) chip degradation only, (2) chip degradation + phosphor layer degradation, and (3) chip degradation + phosphor layer degradation + packaging material degradation. The three SPDs with the original SPD are shown in Fig. 5.15.

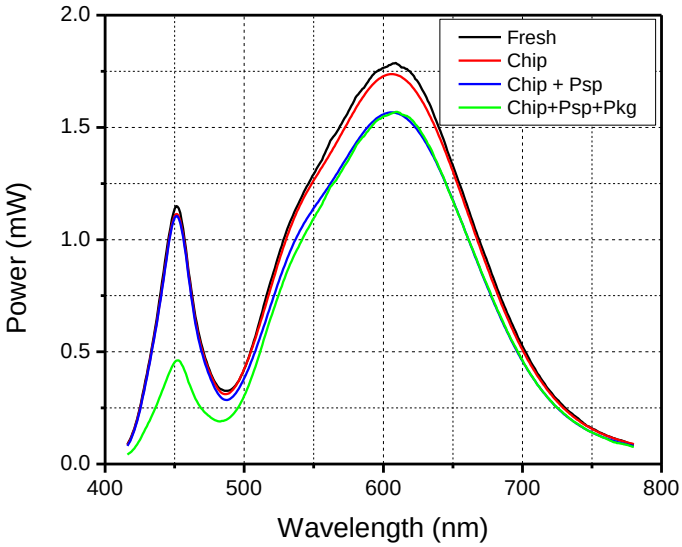

Figure 5.15 SPDs altered by the combinations of three degradation mechanisms

The optical parameters (lumen, CCT, CRI) were calculated from the SPDs. The results are shown in Fig. 5.16. The total lumen reduction was approximately 15%. The chip degradation and the packaging material degradation reduced the lumen by 3%, respectively. The phosphor layer degradation reduced the lumen most

significantly and caused the lumen reduction of 9% (Fig. 5.16a), which is three times as large as the reduction caused by the chip or packaging material.

As can be seen in Fig. 5.16(b) and (c), the effect of the chip degradation and the phosphor layer degradation on the CCT and CRI was virtually negligible. However, the packaging material degradation altered the CCT and CRI significantly; the CCT decreased by more than 300K and the CRI by nearly "4". The changes in CCT and CRI exceed the ENERGY STAR® Program requirements suggested by the US Department of Energy [107].

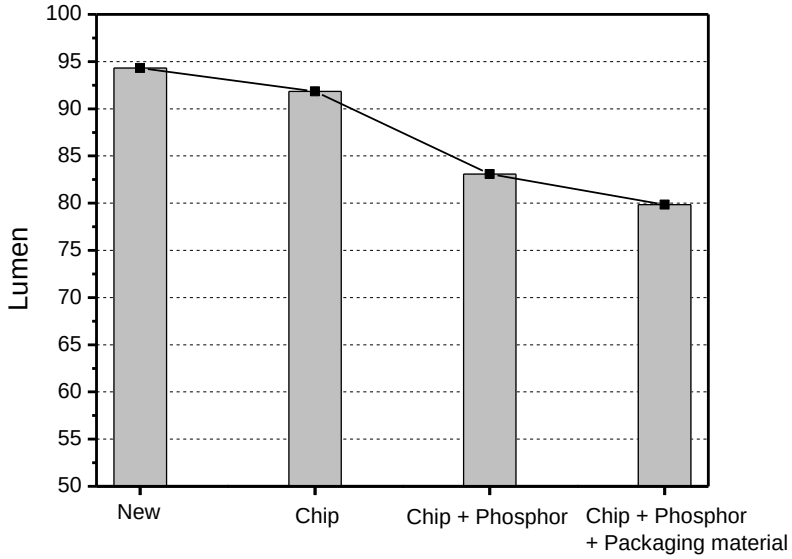

(a)

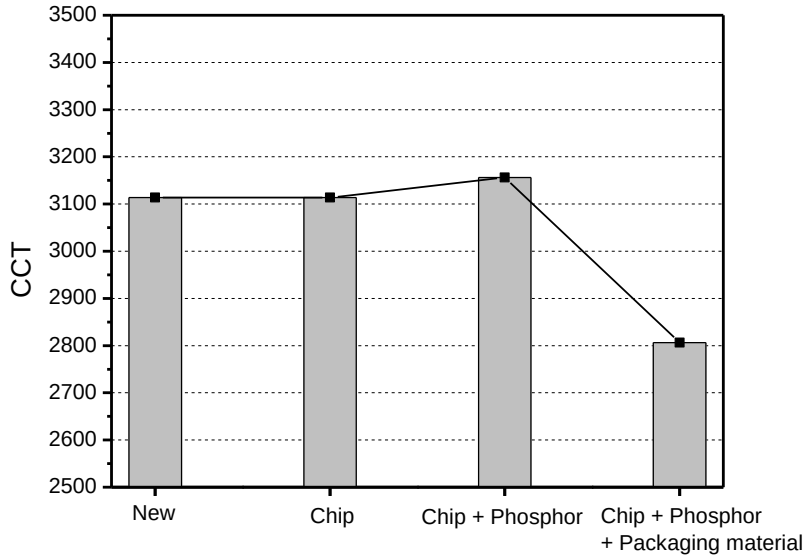

(b)

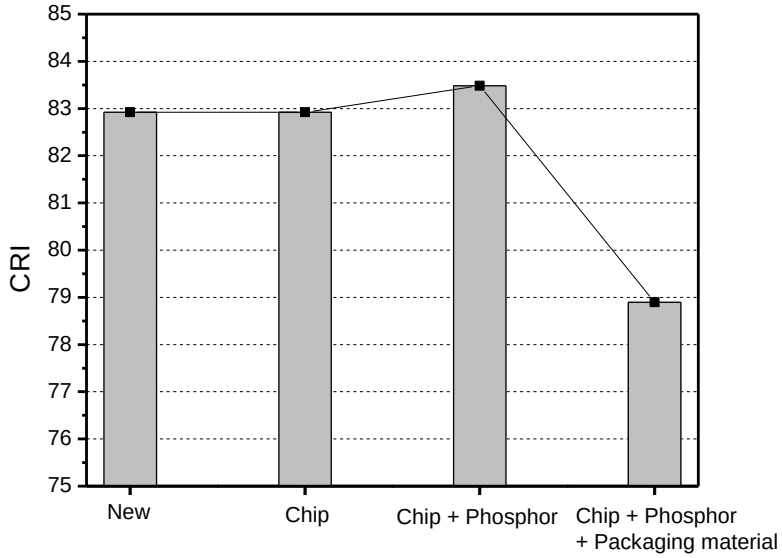

(c)

Figure 5.16 Effect of degradation parameters on optical parameters; (a) lumen; (b) CCT; and (c) CRI

5.5. Discussion

As mentioned earlier, the packaging material degradation spectrum was affected by the silicone lens degradation as well as the encapsulation degradation. The following failure analysis was conducted to evaluate the effect.

Figure 5.17 shows the cross sections of the new and aged LEDs. The yellowing near the outer lens boundary is clearly seen in the aged LED. The outer layer affected by yellowing is estimated to be approximately 30 μm.

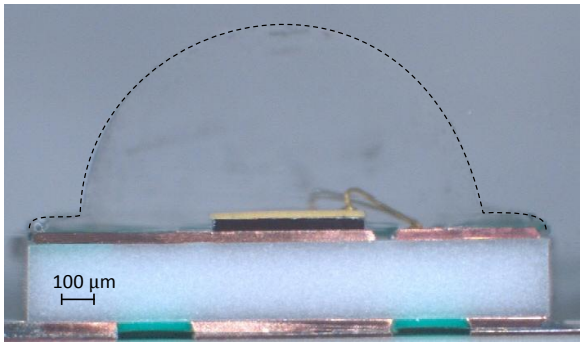

(a)

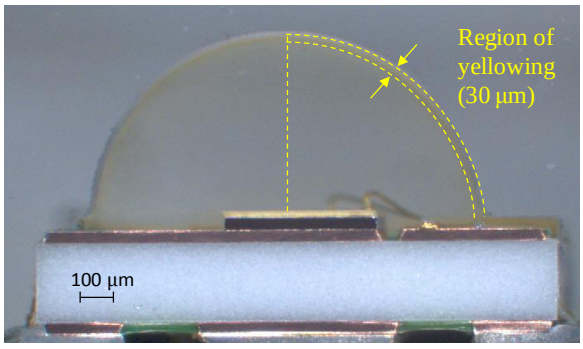

(b)

Figure 5.17 Cross section of (a) new LED and (b) aged LED

In order to quantify the effect of "yellowing", the outer layer of silicone lens was removed by approximately 50 μm. It was done by controlling the decapsulation time; a typical rate of decapsulation was 10 μm per minute and the LEDs were decapsulated for 5 minutes. The SPDs measured before and after the decapsulation are shown in Fig. 5.18. The SPDs remain virtually unchanged after decapsulation, which indicates that the effect of silicone lens yellowing on the SPD of the aged LED was minimal.

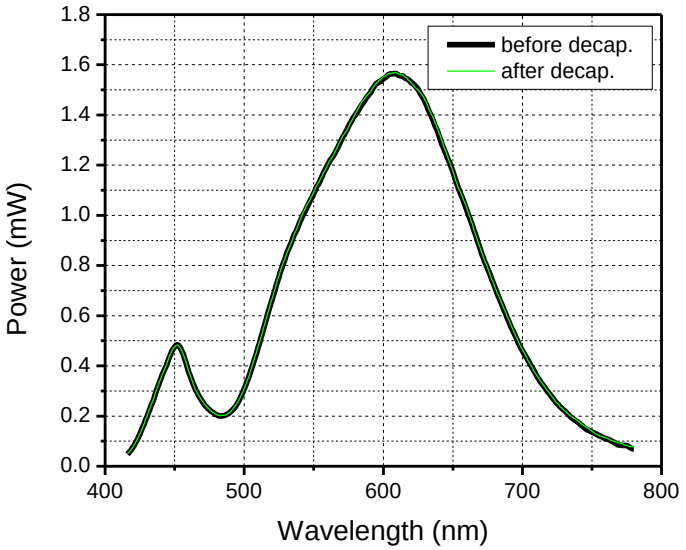

Figure 5.18 Effect of silicone lens yellowing

The failure analysis proceeded with the phosphor layer. The SEM images of the phosphor layers are shown in Fig. 5.19. It is evident that the thickness of phosphor layer was reduced significantly after aging (approximately 8%), and thus the phosphor concentration ratio increased proportionally.

The phosphor concentration ratio was optimized at time zero for both phosphor converted light and leaked blue light. The volumetric shrinkage of the encapsulation material through hardening altered the concentration ratio, and thus contributed to the phosphor layer degradation rate. It also decreased the leaked blue light significantly since the leaked blue light decreased more than the phosphor converted light as the phosphor concentration ratio increased [87]. It is speculated that the unusually smaller value of the packaging material degradation spectrum at the low blue wavelength range may be attributed to this phosphor concentration ratio increase.

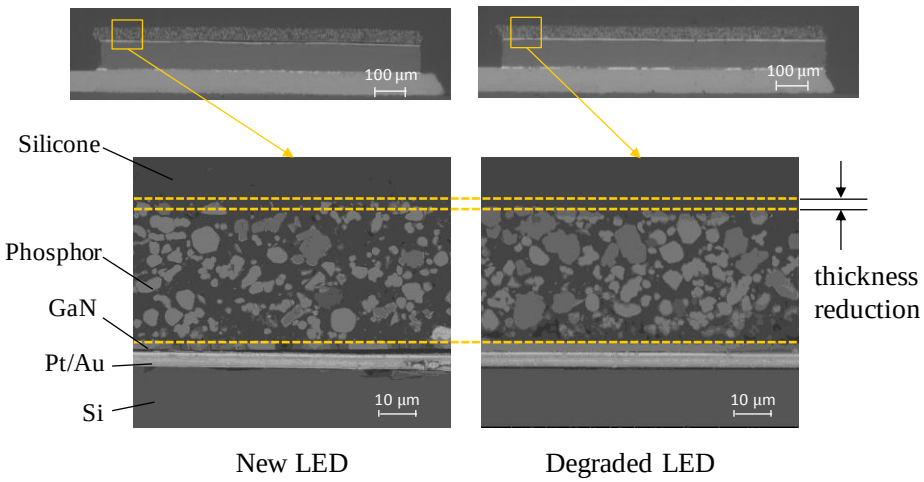

Figure 5.19 Phosphor layers before and after aging

5.6. Conclusion

A degradation analysis model for pc-LEDs were developed and implemented. The model utilized the deconvoluted SPDs before and after operation and

decomposed the SPD change caused by degradation into the contributions of individual degradation mechanisms including chip, phosphor layer and packaging material degradations. The model was implemented a pc-LED with a conformally coated phosphor. The SPDs obtained before and after 9,000 hours of operation were analyzed to quantify the effect of each degradation parameter on lumen, CCT and CRI. The results showed that the phosphor layer degradation contributed to the lumen reduction most significantly (more than 60% of the total lumen reduction). It also showed that the packaging material degradation altered CCT and CRI significantly while the effect of the chip degradation and the phosphor layer degradation on CCT and CRI were virtually negligible.

Chapter 6: Contributions and Future Works

6.1. Thesis Contributions

Design and reliability issues related to high power LED and LED-based SSL were analyzed with analytical and experimental approaches. The most significant contributions made in this dissertation are:

a) A systematic approach to define optimum design domains of LED-based SSL was developed; the domain optimizes cost, energy consumption and reliability. To the best of my knowledge, this systematic approach is not available in the literature. The approach will enable the design engineers of LED-based SSL to quickly evaluate various design solutions for given requirements.

b) A novel hierarchical physics-of-failure based reliability model was developed to estimate the lifetime of actively cooled luminaires. The hierarchical model organized the complicated reliability dependences of the luminaires into the main subassemblies including light engine, active cooling module, and driver electronics. The model is general and can be employed for the lifetime assessment of actively as well as passively cooled LED-based SSLs. The model has unique capability of handling arbitrary operating conditions (i.e., different junction temperatures and forward current levels) and is expected to be utilized widely for SSL reliability assessment.

c) An effective regression scheme using multiple Gaussian functions was developed to deconvolute the SPDs of pc-LEDs. The scheme is so effective that it can reproduce the SPD of LEDs at any stage of operations with extreme accuracy. With the scheme, important practical applications become possible, including the SPD design of pc-LED, the performance evaluation of LED with different package types, and the degradation analysis of LED.

d) A degradation model for pc-LEDs was developed. This is the first attempt to decompose the SPD change caused by the degradation into the contributions of individual degradation mechanisms quantitatively, which could not be done by the existing approaches that dealt with a single mechanism. It is expected that the model will be used effectively to improve the performance of high power pc-LEDs by quantitatively assessing the degradation mechanisms of the given design.

6.2. Future Work

The design and reliability issues of LED-based SSLs will become increasingly important as more and more of them appear in the market. The contributions by this dissertation can be extended in many directions. Some of them are described below.

Prediction of SPD degradation

In this dissertation, the pc-LED degradation model was implemented with SPDs at time = 0 and 9000 hours of operations. The model can be applied for any

SPD obtained during operations. If the SPD is analyzed as a function of time, each degradation parameter can be expressed as a function of time, and thus the SPD degradation can be predicted using appropriate extrapolation schemes. The lifetime of an LED can be predicted in terms of all three optical parameters (lumen, CRI and CCT) if this scheme is developed and implemented properly.

Heat generation by phosphor and its effect on local heating

The phosphor generates heat during conversion (Stokes' loss and non-radiative energy transfer). The heat can cause the junction temperature rise and the phosphor thermal quenching, which will eventually contribute to the reduction of phosphor conversion efficiency and thus the lumen depreciation. Furthermore, the effect of this localized heat on the phosphor layer degradation is still not clearly known. Development of an analytical model to quantify and predict this effect will further improve the reliability model developed in this dissertation.

Light scattering and phosphor conversion model in the phosphor layer

The lumen reduction is affected significantly by the degradation of phosphor layer which consists of phosphor powder and encapsulation material. The failure analysis conducted in this study showed that the thickness of phosphor layer was reduced significantly after aging and thus the phosphor concentration ratio increased proportionally. It was speculated that the unusually smaller value of the packaging material degradation spectrum at the low blue wavelength range might be attributed to this phosphor concentration ratio increase. Development of an analytical model

that considers scattering around phosphors and phosphorescence will be able to quantify the effect of the thickness change and hardening of the phosphor layer.

Failure analysis of LED-based SSL

The hierarchical model considers only degradation of the luminaire based on the LED lifetime. Components such as regulator and MOSFET in the driver electronics would experience failure rather than degradation during operations. The reliability assessment of these components and a subsequent investigation on their effects on the luminaire failure will be an excellent extension of the current study.

Analysis of lens degradation in the luminaire

LED-based luminaires are designed to redirect a light output pattern to produce a specific light distribution. Secondary lens systems, also called secondary optics, are often used to customize the light output pattern of an LED when its light distribution does not satisfy the desired light distribution of a luminaire. The luminaire tested in this study utilized polycarbonate lens systems. The degradation of the lens system can contribute to lumen depreciation and color change. The effect of the lens system degradation was included as a part of light engine degradation in the current study. If the lens system degradation is evaluated separately, the effect of the LED degradation on the SPD of the luminaire can be assesses more accurately, which will subsequently help identify the best suited LED for a given luminaire design.

Reference

[1] Cree. (2012). *Cree Sets New R&D Performance Record with 254 Lumen-Per-Watt Power LED.*

[2] C. Shun-Lien, *et al.*, "Kinetic model for degradation of light-emitting diodes," *IEEE Journal of Quantum Electronics,* vol. 33, pp. 970-979, 1997.

[3] N. Narendran, *et al.*, "Solid-state lighting: failure analysis of white LEDs," *Journal of Crystal Growth,* vol. 268, pp. 449-456, 2004.

[4] N. Narendran and Y. Gu, "Life of LED-based white light sources," *Journal of Display Technology,* vol. 1, pp. 167-171, 2005.

[5] T. Yanagisawa and T. Kojima, "Long-term accelerated current operation of white light-emitting diodes," *Journal of Luminescence,* vol. 114, pp. 39-42, 2005.

[6] Y. Deshayes, *et al.*, "Long-term Reliability Prediction of 935 nm LEDs Using Failure Laws and Low Acceleration Factor Ageing Tests," *QUALITY AND RELIABILITY ENGINEERING INTERNATIONAL,* vol. 21, p. 24, 2005.

[7] S. Ishizaki, *et al.*, "Lifetime Estimation of High Power White LEDs," *Journal of Light and Visual Environment,* vol. 31, pp. 11-18, 2007.

[8] J.-S. Jeong, *et al.*, "Reliability improvement of InGaN LED backlight module by accelerated life test (ALT) and screen policy of potential leakage LED," *Microelectronics Reliability,* vol. 48, p. 5, 2008.

[9] J. J. Fan, *et al.*, "Physics-of-Failure-Based Prognostics and Health Management for High-Power White Light-Emitting Diode Lighting," *Ieee*

Transactions on Device and Materials Reliability, vol. 11, pp. 407-416, Sep 2011.

[10] J. J. Fan, *et al.*, "Lifetime Estimation of High-Power White LED Using Degradation-Data-Driven Method," *Ieee Transactions on Device and Materials Reliability,* vol. 12, pp. 470-477, Jun 2012.

[11] T. Yanagisawa, "Estimation of the degradation of InGaN/AlGaN blue light-emitting diodes," *Microelectronics Reliability,* vol. 37, pp. 1239-1241, 1997.

[12] G. Meneghesso, *et al.*, "Failure Modes and Mechanisms of DC-Aged GaN LEDs," *physica status solidi (a),* vol. 194, pp. 389-392, 2002.

[13] X. A. Cao, *et al.*, "Defect generation in InGaN/GaN light-emitting diodes under forward and reverse electrical stresses," *Microelectronics Reliability,* vol. 43, pp. 1987-1991, 2003.

[14] A. Uddin, *et al.*, "Study of degradation mechanism of blue light emitting diodes," *Thin Solid Films,* vol. 483, pp. 378-381, 2005.

[15] M. Pavesi, *et al.*, "Effects of extreme dc-ageing and electron-beam irradiation in InGaN/AlGaN/GaN light-emitting diodes," *Semiconductor Science and Technology,* vol. 21, pp. 138-143, 2006.

[16] M. Pavesi, *et al.*, "Temperature dependence of the electrical activity of localized defects in InGaN-based light emitting diodes," *Applied Physics Letters,* vol. 89, pp. 041917-3, 2006.

[17] J. Hu, *et al.*, "Electrical, optical and thermal degradation of high power GaN/InGaN light-emitting diodes," *Journal of Physics D: Applied Physics,* vol. 41, p. 035107, 2008.

[18] E. Nogueira, *et al.*, "Evaluation of AlGaInP LEDs reliability based on accelerated tests," *Microelectronics Reliability,* vol. 49, pp. 1240-1243, 2009.

[19] J.-M. Kang, *et al.*, "Life-time estimation of high-power blue light-emitting diode chips," *Microelectronics Reliability,* vol. 49, pp. 1231-1235, 2009.

[20] M. Meneghini, *et al.*, "A Review on the Physical Mechanisms That Limit the Reliability of GaN-Based LEDs," *Ieee Transactions on Electron Devices,* vol. 57, pp. 108-118, Jan 2010.

[21] R. Mueller-Mach, *et al.*, "High-power phosphor-converted light-emitting diodes based on III-nitrides," *Ieee Journal of Selected Topics in Quantum Electronics,* vol. 8, pp. 339-345, 2002.

[22] M. Meneghini, *et al.*, "High temperature electro-optical degradation of InGaN/GaN HBLEDs," *Microelectronics Reliability,* vol. 47, pp. 1625-1629, 2007.

[23] G. Meneghesso, *et al.*, "Recent results on the degradation of white LEDs for lighting," *Journal of Physics D: Applied Physics,* vol. 43, p. 354007, 2010.

[24] E. Jung, *et al.*, "Optical Degradation of Phosphor-Converted White GaN-Based Light-Emitting Diodes under Electro-Thermal Stress," *Journal of The Electrochemical Society,* vol. 158, pp. H132-H136, 2011.

[25] J. L. Down, "The Yellowing of Epoxy Resin Adhesives: Report on Natural Dark Aging," *Studies in Conservation,* vol. 29, pp. 63-76, 1984.

[26] A. L. Andrady, *et al.*, "Effects of increased solar ultraviolet radiation on materials," *Journal of Photochemistry and Photobiology B: Biology,* vol. 46, pp. 96-103, 1998.

[27] A. Torikai and H. Hasegawa, "Accelerated photodegradation of poly(vinyl chloride)," *Polymer Degradation and Stability*, vol. 63, pp. 441-445, 1999.

[28] J. S. Wolffsohn, *et al.*, "Contrast is enhanced by yellow lenses because of selective reduction of short-wavelength light," *Optometry and Vision Science*, vol. 77, pp. 73-81, Feb 2000.

[29] Y. H. Lin, *et al.*, "Development of High-Performance Optical Silicone for the Packaging of High-Power LEDs," *Components and Packaging Technologies, IEEE Transactions on*, vol. 33, pp. 761-766, 2010.

[30] S.-C. Yang, *et al.*, "Failure and degradation mechanisms of high-power white light emitting diodes," *Microelectronics Reliability*, vol. 50, pp. 959-964, 2010.

[31] J.-S. Kim, *et al.*, "Thermal stability of sol–gel derived methacrylate oligosiloxane-based hybrids for LED encapsulants," *Journal of Sol-Gel Science and Technology*, vol. 53, pp. 434-440, 2010.

[32] S. I. Chan, *et al.*, "Accelerated life test of high power white light emitting diodes based on package failure mechanisms," *Microelectronics Reliability*, vol. 51, pp. 1806-1809, 2011.

[33] "ENERGY STAR® Program Requirements for Solid State Lighting Luminaires Eligibility Criteria-Version 1.1," U. S. D. o. Energy, Ed., ed, 2008.

[34] Y. Xi and E. F. Schubert, "Junction temperature measurement in GaN ultraviolet light-emitting diodes using diode forward voltage method," *Applied Physics Letters*, vol. 85, pp. 2163-2165, 2004.

[35] A. K. Gaigalas, *et al.*, "Procedures for Wavelength Calibration and Spectral Response Correction of CCD Array Spectrometers," *Journal of Research of the National Institute of Standards and Technology*, vol. 114, pp. 215-228, Jul-Aug 2009.

[36] B. Han, *et al.*, "Coupled Thermal and Thermo-Mechanical Design Assessment of High Power Light Emitting Diode," *Components and Packaging Technologies, IEEE Transactions on*, vol. 33, pp. 688-697, 2010.

[37] "Cree® XLamp® XR-E LED," vol. CLD DS-05 REV11, ed: CREE. Inc, 2009.

[38] N. Narendran, *et al.*, "Estimating junction temperature of high-flux white LEDs," *Light-emitting diodes: research, manufacturing, and applications VII, Proceeding of SPIE (Society of Photo-Optical Instrumentation Engineers) 5366*, pp. 158-160, 2004.

[39] L. Jayasinghe, *et al.*, "Characterization of thermal resistance coefficient of high-power LEDs," presented at the Sixth International Conference on Solid State Lighting, Proceedings of SPIE 6337, , 2006.

[40] "Luminaire Efficacy," in Energy Efficiency and Renewable Energy, LED Application Series, U.S. Department of Energy2008.

[41] M. Neary and M. Quijano, "Solid state lighting for industrial locations," in *Petroleum and Chemical Industry Conference, 2009. PCIC 2009. 2009 Record of Conference Papers - Industry Applications Society 56th Annual*, 2009, pp. 1-7.

[42] Y. L. Li, *et al.*, "Efficiency droop behaviors of InGaN/GaN multiple-quantum-well light-emitting diodes with varying quantum well thickness," *Applied Physics Letters,* vol. 91, pp. 181113-181113-3, 2007.

[43] M.-H. Kim, *et al.*, "Origin of efficiency droop in GaN-based light-emitting diodes," *Applied Physics Letters,* vol. 91, pp. 183507-183507-3, 2007.

[44] C.-L. Chao, *et al.*, "Reduction of Efficiency Droop in InGaN Light-Emitting Diode Grown on Self-Separated Freestanding GaN Substrates," *IEEE Photonics Technology Letters,* vol. 23, pp. 798-800, Jun 15 2011.

[45] "Lifetime of White LEDs," U. S. D. o. Energy, Ed., ed, 2006.

[46] Subcommittee on Solid State Lighting of the IESNA Testing Procedures Committee, "Approved Method: Measuring Lumen Maintenance of LED Light Sources, LM-80-08," ed: New York: Illuminating Engineering Society of North America, 2008.

[47] "Evaluating the Lifetime Behavior of LED Systems," ed: Philips, Lumileds, 2010.

[48] "Cree® XLamp® Long-Term Lumen Maintenance," vol. CLD-AP28 REV.0, ed: CREE, 2010.

[49] L. Trevisanello, *et al.*, "Thermally activated degradation and package instabilities of low flux LEDs," *IEEE Int. Reliability Physics Symp. IRPS 2009,* 2009.

[50] http://www.usreflector.com/PDF%20files/LED-Lights/LED-wall-wash-light.pdf. [Online].

[51] G. Arnold, "Efficiency Vermont SSL Programs 2009," presented at the ENERGY STAR Lighting Partners Meeting, San Antonio, TX, 2009.

[52] B.-M. Song, *et al.*, "Hierarchical Life Prediction Model for Actively Cooled LED-Based Luminaire," *Components and Packaging Technologies, IEEE Transactions on,* vol. 33, pp. 728-737, 2010.

[53] M. Arik, *et al.*, "Development of a High-Lumen Solid State Down Light Application," *IEEE Transactions on Components and Packaging Technologies,* vol. 33, pp. 668-679, 2010.

[54] M. Arik, "An investigation into feasibility of impingement heat transfer and acoustic abatement of meso scale synthetic jets," *Applied Thermal Engineering,* vol. 27, pp. 1483-1494, 2007.

[55] M. Arik, "Local heat transfer coefficient of a high frequency synthetic jets during impingement cooling over flat surfaces," *Heat transfer Engineering,* vol. 29, pp. 763 - 773, 2008.

[56] Y. Gu, *et al.*, "White LED performance," presented at the 4th International Conference on Solid State Lighting, 2004.

[57] L. Han and N. Narendran, "Developing an Accelerated Life Test Method for LED Drivers," presented at the 9th International Conference on solid State Lighting, San Diego, 2009.

[58] G. Nader, *et al.*, "Effective Damping Value of Piezoelectric Transducer Determined by Experimental Techniques and Numerical Analysis," *ABCM Symposium Series in Mechatronics,* vol. 1, pp. 271-279, 2004.

[59] M. H. Bao and H. Yang, "Squeeze film air damping in MEMS," *Sensors and Actuators a-Physical,* vol. 136, pp. 3-27, 2007.

[60] S. S. Rao, *Mechanical Vibrations*, 3 ed. New York: Addison-Wesley, 1995.

[61] J. Wise, *et al.*, "An Ultrasensitive Technique for Testing the Arrhenius Extrapolation assumption for Thermally Aged Elastomers," *Polymer Degradation and Stability,* vol. 49, pp. 403-418, 1995.

[62] W.-P. Tai and S.-H. Kim, "Relationship between cyclic loading and degradation of piezoelectric properties in Pb(Zr,Ti)O3 ceramics," *Materials Science and Engineering,* vol. B38, pp. 182-185, 1996.

[63] W. P. Chen, *et al.*, "Degradation in lead zirconate titanate piezoelectric ceramics by high power resonant driving," *Materials Science and Engineering B-Solid State Materials for Advanced Technology,* vol. 99, pp. 203-206, 2003.

[64] K. Harada, *et al.*, "Use of ESR for Deterioration Diagnosis of Electrolytic Capacitor," *IEEE Transactions on Power Electronics,* vol. 8, pp. 355-361, Oct. 1993.

[65] V. A. Sankaran, *et al.*, "Electrolytic Capacitor Life Testing and Prediction," presented at the IEEE Industry Applications Society Annual Meeting, New Orleans, Louisiana, 1997.

[66] A. Lahyani, *et al.*, "Failure prediction of electrolytic capacitors during operation of a switchmode power supply," *IEEE Transactions on Power Electronics,* vol. 13, pp. 1199-1207, 1998.

[67] J. L. Stevens, *et al.*, "The Service Life of Large Aluminum Electrolytic Capacitors: Effects of Construction and Application.," *IEEE Transactions on Industry Applications*, vol. 38, pp. 1441-1446, Oct. 2002.

[68] Z. Qin, *et al.*, "Effect of temperature and moisture on the luminescence properties of silicone filled with YAG phosphor," *Journal of Semiconductors*, vol. 32, p. 012002, 2011.

[69] G. Pozina, *et al.*, "Origin of multiple peak photoluminescence in InGaN/GaN multiple quantum wells," *Journal of Applied Physics*, vol. 88, pp. 2677-2681, 2000.

[70] L. T. Tan, *et al.*, "Photoluminescence and phonon satellites of single InGaN/GaN quantum wells with varying GaN cap thickness," *Applied Physics Letters*, vol. 89, p. 101910, 2006.

[71] E. Coetsee, *et al.*, "Luminescent mechanism of Y2SiO5:Ce phosphor powder," *Physica B: Condensed Matter*, vol. 404, pp. 4426-4430, 2009.

[72] Y. Ohno, "Spectral design considerations for white LED color rendering," *Optical Engineering*, vol. 44, p. 111302, 2005.

[73] Y. Uchida and T. Taguchi, "Lighting theory and luminous characteristics of white light-emitting diodes," *Optical Engineering*, vol. 44, p. 124003, 2005.

[74] N.-C. Hu, *et al.*, "Implementing dynamic daylight spectra with light-emitting diodes," *Appl. Opt.*, vol. 47, pp. 3423-3432, 2008.

[75] R. Zheng, "Luminous Efficiency and Color Rendering of Phosphor-Converted White LEDs," *Journal of Light & Visual Environment*, vol. 32, pp. 230-233, 2008.

[76] F. Reifegerste and J. Lienig, "Modelling of the Temperature and Current Dependence of LED Spectra," *Journal of Light & Visual Environment,* vol. 32, pp. 288-294, 2008.

[77] A. Keppens, *et al.*, "Modeling high power light-emitting diode spectra and their variation with junction temperature," *Journal of Applied Physics,* vol. 108, pp. 043104-7, 2010.

[78] I. Moreno and C.-C. Sun, "Modeling the radiation pattern of LEDs," *Optics Express,* vol. 16, pp. 1808-1819, Feb 4 2008.

[79] R. Deepa and S. Arvind, "Modeling and Simulation of Multielement LED Source," *Journal of Light & Visual Environment,* vol. 35, pp. 34-41, 2011.

[80] L. Zongyuan, *et al.*, "Analysis of factors affecting color distribution of white LEDs," in *Electronic Packaging Technology & High Density Packaging, 2008. ICEPT-HDP 2008. International Conference on*, 2008, pp. 1-8.

[81] L. Zongyuan, *et al.*, "Optical Analysis of Phosphor's Location for High-Power Light-Emitting Diodes," *Device and Materials Reliability, IEEE Transactions on*, vol. 9, pp. 65-73, 2009.

[82] "http://www1.eere.energy.gov/buildings/ssl/sslbasics_ledbasics.html," *U.S. Departement of Energy*, 2012.

[83] H. Luo, *et al.*, "Analysis of high-power packages for phosphor-based white-light-emitting diodes," *Applied Physics Letters,* vol. 86, pp. 243505-3, 2005.

[84] J. K. Kim, *et al.*, "Strongly Enhanced Phosphor Efficiency in GaInN White Light-Emitting Diodes Using Remote Phosphor Configuration and Diffuse

Reflector Cup," *Japanese Journal of Applied Physics,* vol. 44, pp. L649-L651, 2005.

[85] H. Luo, *et al.,* "Trapped whispering-gallery optical modes in white light-emitting diode lamps with remote phosphor," *Applied Physics Letters,* vol. 89, pp. 041125-3, 2006.

[86] T. Nguyen The, *et al.*, "Effect of Phosphor Particle Size on Luminous Efficacy of Phosphor-Converted White LED," *Lightwave Technology, Journal of,* vol. 27, pp. 5145-5150, 2009.

[87] J. You, *et al.,* "Phosphor-Concentration-Dependent Characteristics of White LEDs in Different Current Regulation Modes," *Journal of Electronic Materials,* vol. 38, pp. 761-766, 2009.

[88] A. Keppens, *et al.,* "Determining phosphors' effective quantum efficiency for remote phosphor type LED modules," presented at the CIE Tutorial and Expert Symposium on Spectral and Imaging Methods for Photometry and Radiometry location, Bern, 2010.

[89] J. P. You, *et al.,* "Light extraction enhanced white light-emitting diodes with multi-layered phosphor configuration," *Opt. Express,* vol. 18, pp. 5055-5060, 2010.

[90] J. P. You, *et al.,* "Phosphor Concentration Effects on Optothermal Characteristics of Phosphor Converted White Light-Emitting Diodes," *Journal of Electronic Packaging,* vol. 132, pp. 031010-4, 2010.

[91] "LED life for General Lighting: Definition of Life," *Assist,* vol. 1, 2005.

[92] "ENERGY STAR® Manufacturer's Guide for Qualifying Solid State Lighting Luminaires – Version 2.1," *Department of Energy, US,* 2010.

[93] L. Sugiura, "Dislocation motion in GaN light-emitting devices and its effect on device lifetime," *Journal of Applied Physics,* vol. 81, pp. 1633-1638, 1997.

[94] L. Sugiura, "Comparison of degradation caused by dislocation motion in compound semiconductor light-emitting devices," *Applied Physics Letters,* vol. 70, pp. 1317-1319, 1997.

[95] T. Yanagisawa, "The degradation of GaAlAs red light-emitting diodes under continuous and low-speed pulse operations," *Microelectronics Reliability,* vol. 38, pp. 1627-1630, 1998.

[96] K. Kohler, *et al.,* "Control of the Mg doping profile in III-N light-emitting diodes and its effect on the electroluminescence efficiency," *Journal of Applied Physics,* vol. 97, p. 104914, 2005.

[97] P. Altieri-Weimar, *et al.*, "Influence of doping on the reliability of AlGaInP LEDs," *Journal of Materials Science: Materials in Electronics,* vol. 19, pp. 338-341, 2008.

[98] T. Nguyen The, *et al.*, "Effect of Phosphor Particle Size on Luminous Efficacy of Phosphor-Converted White LED," *Journal of Lightwave Technology,* vol. 27, pp. 5145-5150, 2009.

[99] J. Tharian, "Degradation and failure mode analysis of III-V nitride devices," *IPFA 2007. 14th International Symposium,* pp. 284-287, 2007.

[100] K. Min-Ki, *et al.*, "Gradient doping of Mg in p-type GaN for high efficiency InGaN-GaN ultraviolet light-emitting diode," *IEEE Photonics Technology Letters*, vol. 19, pp. 1880-1882, 2007.

[101] S.-H. Yang and C.-Y. Lu, "Influence of doping and coating on the photoluminescence properties of yttrium aluminum garnet phosphors," *Journal of The Electrochemical Society*, vol. 154, pp. J397-J401, 2007.

[102] G. Meneghesso, *et al.*, "Recent results on the degradation of white LEDs for lighting," *Journal of Physics D-Applied Physics*, vol. 43, Sep 8 2010.

[103] L. Hsun-Tien, *et al.*, "The study of thermal properties and thermal resistant behaviors of siloxane-modified LED transparent encapsulant," presented at the Microsystems, Packaging, Assembly and Circuits Technology, 2007.

[104] R. Baillot, *et al.*, "Effects of silicone coating degradation on GaN MQW LEDs performances using physical and chemical analyses," *Microelectronics Reliability*, vol. 50, pp. 1568-1573, 2010.

[105] J.-S. Wang, *et al.*, "Mean-time-to-failure evaluations of encapsulation materials for LED package in accelerated thermal tests," *Microelectronics Reliability*, vol. 52, pp. 813-817, 2012.

[106] B. Song and B. Han, "SPD Deconvolution Scheme for Phosphor Converted White LED Using Multiple Gaussian Functions," *Applied Optics,* (submitted for publication), October 2012

[107] "ENERGY STAR® Program Requirements for Integral LED Lamps Partner Commitments," *Department of Energy, US*, 2010.